NON-NEWTONIAN FLUID INJECTION INTO GRANULAR MEDIA

A Thesis
Presented to
The Academic Faculty

By

T. Patrick Callahan

In Partial Fulfillment
Of the Requirements for the Degree
Master of Science in Civil Engineering

Georgia Institute of Technology

May 2011

NON-NEWTONIAN FLUID INJECTION INTO GRANULAR MEDIA

Approved by:

Dr. Haying Huang
School of Civil and Environmental Engineering
Georgia Institute of Technology

Dr. Carlos Santamarina
School of Civil and Environmental Engineering
Georgia Institute of Technology

Dr. Leonid Germanovich
School of Civil and Environmental Engineering
Georgia Institute of Technology

Date Approved: April 4, 2011

ACKNOWLEDGEMENTS

Lastly, I cannot express enough the motivation and support I have received over the past years from my entire family. To my mom, dad, and sister: thank you for always being there for me no matter what.

I would like to dedicate this Thesis to my grandparents, Walt and Carol Bedard. For as long as I can remember, and in all aspects of my life, the both of you have been one of my biggest sources for inspiration.

TABLE OF CONTENTS

LIST OF TABLES

LIST OF FIGURES

ABSTRACT

The process of fluid injection into granular media is relevant to a wide number of applications such as enhanced oil recovery, grouting, and the construction of permeable reactive barriers. The response of the subsurface is dependent on multiple factors such as in-situ stresses, fluid properties, flow rate, and formation type. Based on these conditions a variety of response mechanisms can be initiated ranging from simple porous infiltration to hydraulic fracturing.

Currently, the mechanics of fluid injection into competent rock are well understood and can be sufficiently modeled using linear elastic fracture mechanics. Because the grains in rock formations are individually cemented together, they exhibit cohesion and are able to support tensile stresses. The linear elastic method assumes tensile failure due to stress concentrations at the fracture tip. A fracture propagates when the stress intensity factor exceeds the material toughness (Detournay, 1988)

However, understanding fluid injection in cohesionless granular media presents a much larger obstacle. Currently, no theoretical models have been developed to deal with granular media displacements due to fluid injection. Difficulty arises from the complexity of fluid rheology and composition used in engineering processes, the strong coupling between fluid flow and mechanical deformation, the non-linear response of subsurface media, and the multi-scale nature of the problem.

The structure of this thesis is intended to first give the reader a basic background of some of the fundamental concepts for non-Newtonian fluid flow in granular media. Fluid properties as well as some interaction mechanisms are described in relation to the injection process. Next, the

results from an experimental series of injection tests are presented with a discussion of the failure/flow processes taking place.

   We developed a novel technique which allows us to visualize the injection process by use of a transparent Hele-Shaw cell. Specifically, we will be using polyacrylamide solutions at a variety of concentrations to study non-Newtonian effects on the response within the Hele-Shaw cell. By performing tests at a range of solution concentrations and injection rates we are to be able to identify a transition from an infiltration dominated flow regime to a fracturing dominated regime.

CHAPTER 1

INTRODUCTION

1.1   Background

The interaction between fluids and subsurface media has long been an area of interest in the field of engineering. Fluid injection serves a variety of functions including but not limited to grouting and soil stabilization, hydraulic fracturing for oil recovery, subsurface disposal of sequestered carbon and waste, and the construction of permeable reactive barriers (Fayers, 1981; Hainey; Hocking, 1999; Kutzner, 1996). For each application it is crucial that the mechanisms and interactions between fluid and subsurface media are well understood in order to design and optimize the engineering applications.

A variety of flow mechanisms may be achieved during the subsurface fluid injection process based on the required engineering function. For instance, in some processes such as oil recovery, fractures are crucial in order to stimulate reservoirs. Hydraulic fracturing for enhanced oil recovery is a fundamental process in petroleum engineering to increase the permeability of formations and therefore increase the production. The process of hydraulic fracturing has been an area of research interest for many years and is constantly evolving with improving technology and resources (Economides, 2000). Another situation in which fracturing is desirable is compensation grouting; a common process for offsetting subsidence by filling in fractured void spaces with cement mixtures in soil formations (Soga, 2004).

However, in a number of applications fracturing is avoided and a simple pore infiltration process is desired. When injecting supercritical carbon dioxide for underground disposal, fluid is intended to infiltrate pore spaces; fracturing is avoided in order to prevent the transport of waste

fluid out of the reservoir and possibly into groundwater sources through preferential fractured paths (Litynski, 2006). Undesirable fracture also occurs in the oil industry in the form of shallow water flows. When drilling in over-pressurized sand formations at the sea floor, local in-situ stresses can reach failure due to small increases in fluid pressure; this can cause fractures which lead to a loss in circulation and can eventually render a drilled well useless (Ostermeier, 2000)

The interaction of fluid with the subsurface does not follow a well-defined pattern. Applications are carried out in a variety of subsurface materials ranging from rock formations to poorly cemented granular media, and take place at a variety of in-situ confining stresses. Currently, the mechanics of fluid injection into competent rock are well understood and can be sufficiently modeled using linear elastic fracture mechanics (Griffith, 1921). Because the grains in rock formations are individually cemented together, they exhibit cohesion and are able to support tensile stresses. The linear elastic method is based on tensile failure and stress concentrations around the fracture tip, and has been widely used to model and predict the process of fracture propagation in brittle material. A fracture propagates when the stress intensity factor exceeds the material toughness (Detournay, 1988)

Understanding fluid interaction in cohesionless granular media presents a much larger obstacle. Currently, theoretical models that describe the grain displacement due to fluid flow are not yet well understood. Difficulty arises from the complexity of fluid rheology and composition used in engineering processes, the strong coupling between fluid flow and mechanical deformation, the non-linear response of subsurface media, and the multi-scale nature of the problem (Huang, 2008).

The importance of understanding the processes of subsurface fluid injection into weak, uncemented granular media has been illustrated when it was seen that in-situ permeability tests

were yielding much higher outflow results than initially expected (Bjerrum, 1972). In this study, fractures were unintentionally being initiated in the tested soil formations creating a preferential flow path and allowing for higher fluid flow. Fractures were also identified as the cause of several dam failures including the Teton Dam in Idaho (Jaworski, 1981). It was concluded that high pressures resulting from the filling of the reservoir behind the dam caused preferential paths between the rock and soil interface which was progressively eroded and lead to the failure (Seed, 1987). A similar failure process has been witnessed in other soil structures such as dams, embankments and dikes as the result of soil erosion and piping. The instability in fluid/grain interaction can lead to a transition from a static jammed state to a dynamic flowing state in which granular particles are washed away through finger-like channels (Johnsen, 2008).

A number of fluids used in subsurface injection applications exhibit non-Newtonian characteristics and have complex flow properties due to shear thinning, viscoelastic, yield stress, and thixotropic effects. The properties of subsurface media can also exhibit a wide range of variability based on in-situ stresses, particle shape and size, and porosity. In order to understand the mechanisms of fluid/granular media interaction, both fluid and granular media properties must be evaluated to successfully characterize the fluid injection process.

1.2   Objectives

In this work we attempt to gain a better understanding of the mechanisms of pattern formation during non-Newtonian fluid injection into cohesionless granular media. We use a novel technique which allows us to visualize the injection process by use of a transparent Hele-Shaw cell. Specifically, we will be using polyacrylamide solutions at a variety of concentrations to study the effects of non-Newtonian shear-thinning and viscoelastic fluid properties on the

failure and flow response within the Hele-Shaw cell. By performing tests at a range of solution concentrations and injection rates, we attempt to identify a transition from an infiltration dominated flow regime to a fracturing dominated regime. The format of this paper is intended to give the reader a general background for understanding the mechanics taking place during fluid/granular media interaction, then described some of the important results and conclusions of our experimental work.

Chapter 2 begins with a review of non-Newtonian fluid characteristics. This is followed by a discussion of the characteristics of granular suspensions and the hydrodynamic interaction between particles and fluid. A background in Saffman-Taylor instability is presented to illustrate the origin of viscous fingering caused by an instability at the fluid/fluid interface. A combination of the preceding concepts is then incorporated for fluid/particle interaction and the concepts of flow in porous media. Chapter 2 is concluded with an overview of some analogous laboratory studies carried out by various researcher groups.

Chapter 3 presents an overview of our experiment setup, methodology, and sample properties.

Chapter 4 gives an extensive analysis of our experiment results. The results are divided into rheology calculations, a dimensionless analysis, image analysis, and pressure data. The experimental results give valuable insight into the fluid injection process.

Chapter 5 provides an in-depth discussion of our results and further analysis. This is followed by a section of proposed future work which could further advance our understanding of fluid/granular media interaction.

CHAPTER 2

LITERATURE REVIEW

2.1   Non-Newtonain Fluid Properties

In simplest terms, a fluid's response to deformation can be described using Newton's law of viscosity:

$$\tau = \mu\dot{\gamma} \qquad\qquad (1)$$

This law states that the shear stress (τ) acting on a body as a fluid moves parallel to it is a function of shear rate ($\dot{\gamma}$) and viscosity (μ).   The viscosity of Newtonian fluids used in engineering applications can vary several orders of magnitude; for instance, from 1 cP for water to over 1000 cP for fluids such as pure glycerin. For ideal Newtonian fluids the viscosity is only dependant on temperature and pressure. A graph of the shear stress vs shear rate will be linear and pass through the origin, with the slope of the line equal to the fluid viscosity. All gases and liquids made up of relatively small molecules (with molecular weights below about 5000 g/mol) can be accurately described using Newton's law of viscosity (Bird, 2002).

Although the above explanation of fluid behavior may be adequate for simple Newtonian fluids, a wide array of liquids exists with complex molecular structures leading to time and rate dependent properties. These liquids, known as non-Newtonian, have non-linear flow curves and (Bird, 2002). Their response to deformation and strain rate, elongation, and shearing can be categorized into classifications of time-independent, viscoelastic, and time-dependent behavior and are often calculated using Hershel-Buckley, Carreau, Bingham, Ellis, and a variety of other complex models (Macosko, 1994). Figure 1 shows typical flow curves for a variety of Newtonian and non-Newtonian fluids. As seen in the figure, some require an increasing amount

of stress as strain rates increase leading to a convex curve (shear thickening), while a majority

fluids act in an opposite manner in which the rate of stress increase will decrease with the strain

rate applied (shear thinning). Also in some instances, as seen in the three fluids in the upper half

of Figure 1, a yield stress must be overcome within the fluid before any strain is induced (visco-

plastic). In this case, the fluid acts as an elastic solid below a critically applied stress but begins

to flow once the yield stress is overcome.
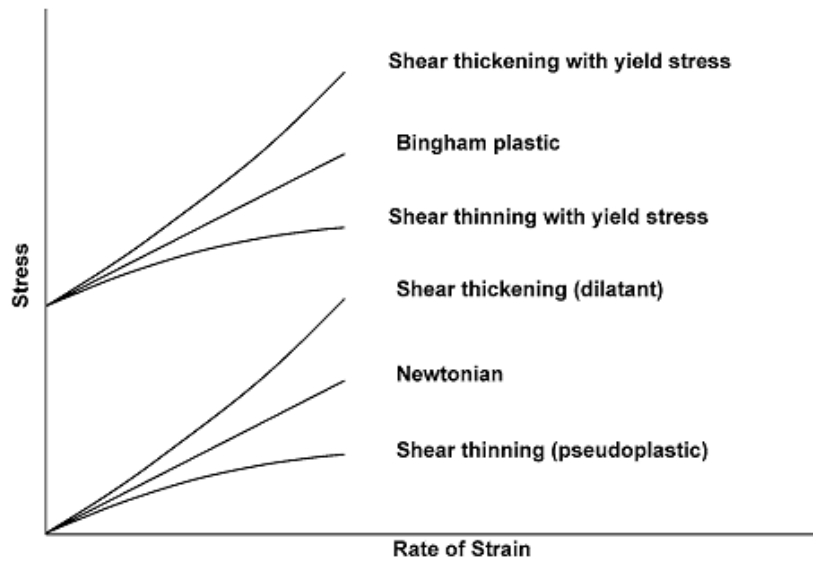
Figure 1: Shear stress / strain rate relationships for a variety of fluid types. The slope of the
Newtonian flow curve is its viscosity (Sochi, 2010)

The viscosity of simple shear-thinning, non-Newtonian liquids is often calculated using

the power law model which relates the response of viscosity as a function of shear rate as:

$$\mu = k\dot{\gamma}^{n-1} \tag{2}$$

where *n* and *k* are the power law index and consistency index, respectively. The power law

index is indicative of the intensity of shear thinning; the lower the value of *n*, the greater the

6

degree of shear-thinning. The consistency index is simply related to the low-shear viscosity of the fluid (Macosko, 1994). The viscosity of time-independent fluids relies only on the applied shear rate for any given time.

Shear-thinning fluids can also exhibit pseudoplastic behavior giving way to characteristic zero shear and infinite shear viscosities (μ_0, μ_∞). For polymeric solutions, the infinite shear rate viscosity approaches a constant due to maximum stretching of individual polymer molecules. A zero-shear value is identified based on the initial internal structure of the fluid while under minimal strain. The effective viscosity of pseudoplastic fluids, given the power-law indices and shear rate, can be calculated using the Carraeu power law model (Macosko, 1994):

$$\frac{\mu - \mu_\infty}{\mu_0 - \mu_\infty} = (1 + (\lambda\dot{\gamma})^2)^{(n-1)/2} \tag{3}$$

where λ is a time constant based on the elastic relaxation time of the fluid at low shear rate.

Along with viscous and pseudoplastic properties, polymer fluids can also exhibit time-dependent elastic characteristics due to polymer chain elongation. The elastic behavior of polymer solutions can be better identified by examining the molecular structure of the liquid. At a microscopic scale the solution is a two-phase liquid consisting of water as the solute and long, intertwined polymer chains dispersed throughout. Fluids such as polyacrylamide solutions have the ability to store a small amount of energy due to entanglement and stretching of individual polymer chains, and thus can exhibit elastic rebounds as shearing is reduced to zero (Ferry, 1948). According to Hooke's law, at small strain the shear stress response of an element is dependent on deformation and elastic modulus; the element will regain its original form if the stress applied is less than a critical yield stress. Some researchers have utilized kinetic theory models to predict these liquids' responses, with the links between polymer chains quantified as

7

elastic springs capable of stretching and storing energy. Figure 2 demonstrates the differences between Newtonian and non-Newtonian velocity profiles and flow characteristics. The retraction of fluid after flow is stopped is due to elastic effects.
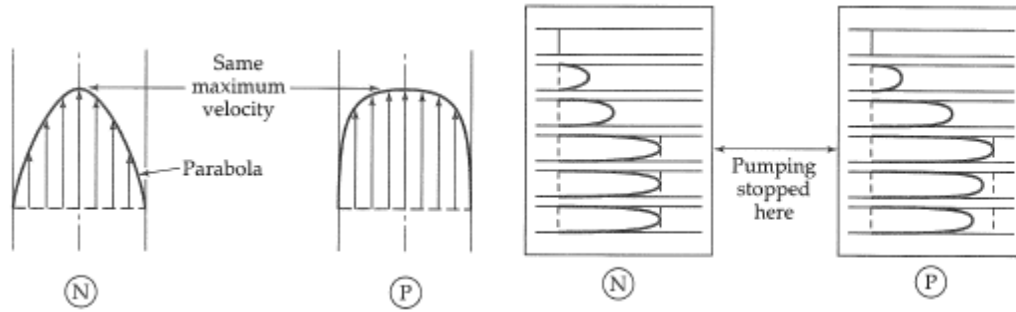
Figure 2: Velocity and flow profiles for Newtonian (N) and power-law (P) fluids. (Ghannam, 1998)

The influence of viscoelasticity on a process can be quantified by the ratio between relaxation time and process time, otherwise known as the Deborah number. The relaxation time is defined based on the relationship between applied strain and resistance, and it is quantified using the storage modulus and loss modulus (G' and G'') of the fluid (Macosko, 1994). When plotting the data of G' and G'' vs. strain rate in graphical form, the crossover of these two curves can be defined as the reciprocal of the fluid relaxation time. The dimensionless Deborah number is a measure of the viscoelastic effect in a given medium.

$$De = \frac{Characteristic\ relaxation\ time\ of\ fluid}{Characteristic\ residence\ time\ of\ process} \tag{4}$$

For instance, a viscoelastic fluid flowing in a medium containing large pores will have a lower Deborah number than the same fluid in smaller pores. This is due to the fact that when

flowing through a larger pore the interstitial velocity and elongational strains are smaller, leading to a higher residence time when compared to flow in a small pore. In regard to solution type, it can be assumed that an increase in polymer concentration will lead to a more pronounced viscoelastic response due to an increased interaction in polymer chains. Any process with a *De* on the order of magnitude of 1.0 is expected to be affected by the elastic response; Marshall et al estimated that in porous media an onset of viscoelastic effects occur for *De* > 0.5-0.6 (Marshall, 1967).

In addition to shear-thinning, pseudoplastic, and viscoelastic responses of non-Newtonian fluids, a number of other complex properties can be identified. Yield stress is a time-independent response in which a fluid exhibits visco-plastic behavior and resists flow below a critical stress value. This is demonstrated by the non-zero stress at small strain for the Hershel-Buckley and Bingham models in Figure 1. Rheopexy is defined as the time-dependent response of shear stresses and is often observed in viscoelastic fluids and is brought about due to structural changes at microscopic levels. When a constant shear rate is applied, the shear stress response overshoots but will decrease with time as the internal structure of the fluid is broken down. Thixotropic responses are the opposite of rheopexy and result in a viscosity increases with the time of shearing (Ghannam, 1998).

An extensive study of polyacrylamide solutions was carried out by Ghannam et al (1998). They measured fluid behavior within a number of experiments and witnessed time and rate dependent changes in viscosity. Figure 3 shows typical viscosity curves for aqueous polyacrylamide solutions at different concentrations. As stated previously for the viscoplastic and Carreau power-law models, a viscosity plateau can be seen at low shear rates while viscosity converges to a limiting value at high shear rates. Often, the range at which the low-shear

viscosity is constant will increase as the molecular weight and concentration of the solution becomes smaller (Chhabra, 2007). The deviation from the zero-shear viscosity is a function of the relaxation time of the fluid. Rheopexy and viscoelastic responses were also seen in transient shear tests, while yield stresses and thixotropy were recorded in controlled stress tests.
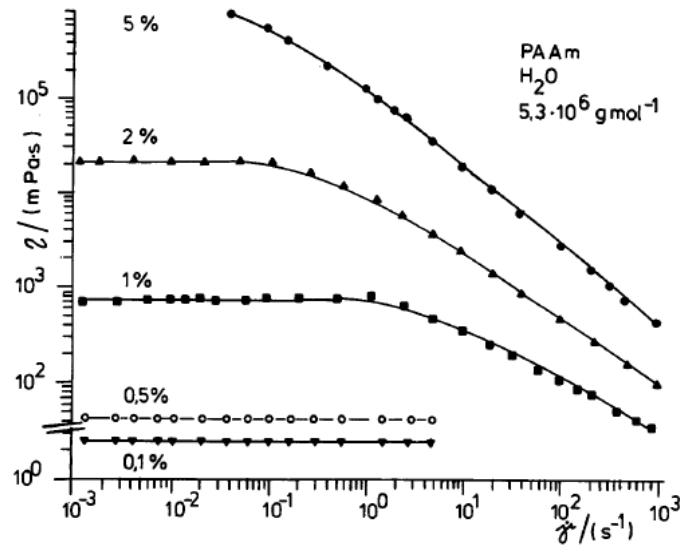
Figure 3*: (a) Flow curve for aqueous polyacrylamide solutions at various concentrations (Kulicke, 1986).

The charasteristics of fluids used in the injection process in the subsurface can be quantified based on a number of fluid properties. Many times, simple rheological models are not sufficient to describe these fluids, and non-Newtonian properties such as shear thinning, viscoelasticity, and thixotropy must be considered. The deviation from Newtonian behavior can be explained by the microscopic structure of solutions and mechanical interactions. An understanding of fluid properties will lead to a more accurate model for predicting the interaction of fluids and porous media.

2.2   Properties of Granular Suspensions

When studying the deformations and flow/failure patterns taking place during the process of fluid injection into granular media, it is important to not only understand the rheology and characteristics of the invading fluid, but also the physical process in granular media. The response of the granular media is dependent on the coupling of fluid flow and particle interaction. The phenomena taking place during injection can range from viscous fingering, to viscoelastic fracture, to simple pore infiltration and can be understood based on energy dissipation mechanisms and fluid/particle interaction.

As is often the case for fluid injection into granular media, fracture is initiated just behind an infiltration front in which the pore space is saturated. One approach to understanding the deformation process in a saturated granular media is to consider the representative volume as a concentrated suspension, with a viscous non-Newtonian fluid invading a more viscous concentrated granular suspension; the fracture can be analogous to a Saffman-Taylor type instability.

The behavior of suspensions has been an area of interest in a variety of practices and can be categorized within three separate fields: fluid rheology, physics of granular matter, and soil mechanics (Coussot, 1998). The hydrodynamic interactions of suspensions have been studied since Einstein (1906) and are quantified based on the flow properties of the interstitial fluid, the grain fraction, and the maximum packing density of the granular suspension. These models take into account hydrodynamic or Brownian effects between the particles. However, they do not account for large changes in shear, viscoelastic, or thixotropic effects. Physical models have also been developed based on kinetic theory and numerical simulation of particle interaction. An

equation for suspension rheology with negligible colloidal interactions was proposed (Chong, 1971);

$$\boldsymbol{\mu}_{gr} = \boldsymbol{\mu}_0 \left(1 + \frac{3}{4}\frac{\phi}{\phi_m - \phi}\right)^2 \tag{5}$$

This equation accounts for the interstitial fluid viscosity (μ_0), grain density within the fluid (ϕ), and maximum packing density (ϕ_m), and accurately predicts that the viscosity of a suspension will approach infinity as $\phi \rightarrow \phi_m$. In soil mechanics flow of concentrated suspensions can be described by plastic theory and associated flow rule.

The work of Coussot and Ancey (1999) categorized the characteristics of flows of granular suspensions or pastes into several regimes and proposed a dimensionless analysis to identify these regimes. The regimes are identified as frictional, lubricational, and collisional for "hard" or dense suspensions with grain fractions above a certain critical value. Other less-concentrated suspension types can be further subdivided into colloidal, Brownian, hydrodynamic, and turbulent dominated interactions at lower grain fractions and flow conditions. A diagram of the described granular suspension regime map is shown in Figure 4. The figure is subdivided based on grain fraction and flow conditions, and the boundaries between different flow regimes can be identified based on several dimensionless groups.
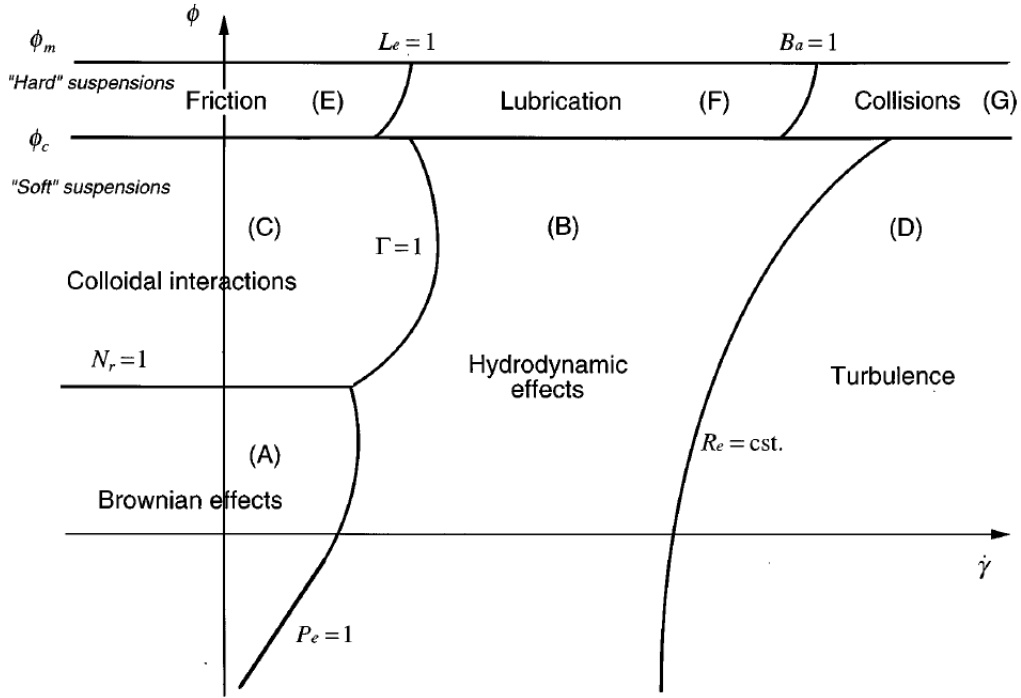
Figure 4: Regime map for the transition of flow conditions for granular suspensions (Coussot, 1999)

As seen at the transition points dividing the various regimes, the boundaries are quantified based on a set of seven dimensionless numbers. This regime map is sufficient for a variety of suspension types and accounts for colloidal interactions, fluid forces, and particle level forces. However, due to the initially dense state of most subsurface conditions, it can be assumed that the in-situ grain fraction is above the proposed "critical" value and inertial effects are negligible. Therefore focus can be given to the transition between frictional and lubricational interactions (Ancey, 1999a).

Before significant strain deformation within a granular medium is encountered due to fluid flow, it can be assumed that a saturated granular medium exhibits a constant grain fraction dependent on the initial packing state. When fluid viscosity and flow rates are below a critical

value to initiate significant granular displacement, stresses are transmitted mainly through the frictional forces of sustained contacts in the granular skeleton, and the role of the fluid phase is related solely to the pore pressure. As deformation and shear rates increase, the fluid viscosity plays a more significant role and a transition from the frictional to lubricational regime occurs between grains. In this instance, the mechanisms of particle interactions are influenced by hydrodynamics, and the response of the interstitial fluid is dependent on the shear-thinning characteristic of the fluid. The lubricated contact forces between particles can be subdivided into components of squeezing, shearing, and rotation. Finally, as shear deformation increases, viscosity and strain rates may be neglected and the response of the granular suspension is dominated by momentum interactions due to the collision of particles. In this phase, inertia effects play a predominant role and may overcome the hydrodynamic effects. The transition from a friction, lubrication, and collision dominated regimes can be quantitatively determined based on the dimensionless Bagnold, Coulomb, and Leighton numbers (Ancey, 1999a). These dimensionless numbers are calculated based on fluid density (ρ_p), shear rate (γ), fluid viscosity (μ_o), strain (ϵ), effective stresses (σ'), length constant (b), and particle size (r).

$$Ba = \frac{\rho_p \gamma r^2}{\mu_0 \ln\left(\frac{\varepsilon^*}{\varepsilon}\right)} \tag{6}$$

$$Le = \left(\frac{\mu_0 \gamma b}{\sigma' \varepsilon}\right) \tag{7}$$

$$Co = \left(\frac{\rho_p \gamma^2 r^2}{\sigma'}\right) \tag{8}$$

(i)   a frictional regime for Co ≪ 1 and Le ≪ 1,
(ii)   a collisional regime for Co ≫ 1 and Ba ≫ 1,
(iii)   a hydrodynamic regime for Ba ≪ 1 and Le ≫ 1.

In the research work of Chevalier (2007, 2009) the effects of grain fraction on the response of failure mechanisms in granular suspensions were studied. They concluded that the rheology was not a function of cell geometry or grain diameter, but rather a function only of grain fraction. The flow profiles for a variety of suspension types are shown in Figure 5, from flow in pure fluid to flow in a rigid porous media. The patterns migrate from a single Saffman-Taylor instability to viscous fingering.
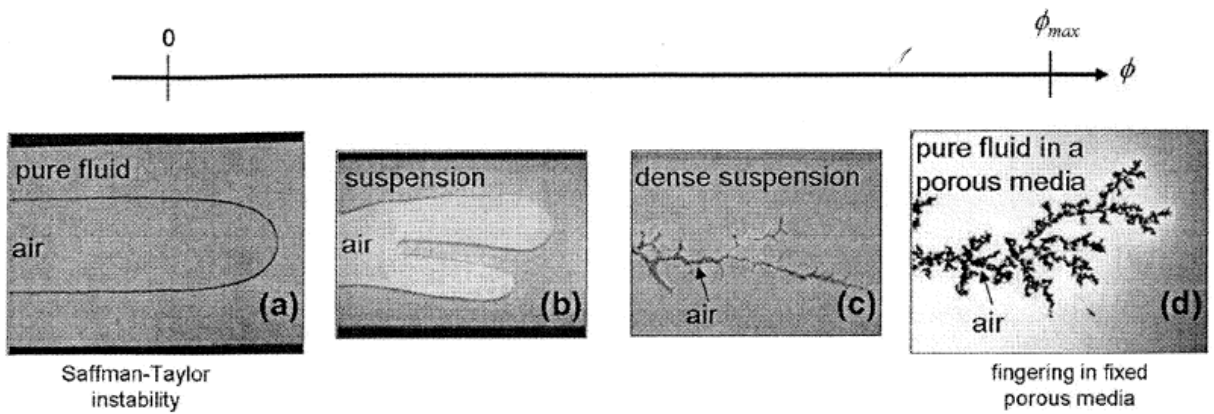
Figure 5: Transition from Saffman-Taylor instability to fingering for an increase in suspension grain fraction (Chevalier, 2009)

Chevalier (2009) also measured the pressure gradient (ΔP^*), which can be predicted using a modified Darcy equation as a function of flow velocity (V) and granular suspension rheology μ_{gr}

$$\Delta \mathbf{P}^* = \frac{12\mu_{gr}(\phi)}{b^2} * \mathbf{V} \tag{9}$$

2.3 Saffman-Taylor Instability

The flow of fluid in porous media has been an area of interest for several decades, and is often the subject of research in the oil and mining industry. Due to the use of fluid injection for

hydraulic fracturing and flooding for enhanced oil recovery, it is necessary to understand the processes taking place at the fluid/fluid interface. Instabilities at the fluid/oil interface lead to a decrease in production efficiency and undesired mixing of oil and injecting fluid within the reserves. This instability has physically been seen in the field as "water tonguing or coning" which occurs when the velocity of oil extraction is too high and fingers of water invade the oil reservoir (Saffman, 1958). Extensive investigation of the interactions between fluids in porous media was performed in the 1950s by researchers such as R.L. Chouke, P.G. Saffman and Geoffrey Taylor. They found that in pressure gradient driven flows the interface between two fluids can be quantified as either stable or unstable based on pressure, viscosity, density, and permeability relationships.

Saffman and Taylor used flow between two parallel plates within a gap of thickness *b* as an analogue for modeling flow in porous media with a permeability of $b^2/12$. They used a linear Hele-Shaw cell with two fluids (air and various oils) forming an interface and calculated the mean velocity inside the cell as:

$$V = -\left(\frac{b^2}{12\mu}\right) grad(p + \rho g x) \tag{10}$$

They varied the fluid and flow properties within the cell to study the response and concluded that for negligible interfacial tension fluids the interface between two fluids was stable (i.e. a uniform, linear propagation of the invading fluid) if

$$\left(\frac{\mu_2}{k_2} - \frac{\mu_1}{k_1}\right) V + (\rho_2 - \rho_1) g > 0 \tag{11}$$

and unstable (i.e. growth of viscous fingers) if

$$\left(\frac{\mu_2}{k_2} - \frac{\mu_1}{k_1}\right) V + (\rho_2 - \rho_1) g < 0 \tag{12}$$

Expounding on the work carried out by Saffman and Taylor, other investigations were completed to study instabilities taking place during fluid/fluid interface flows (Chouke et al 1959, Gupta et al 1973). Paterson (1981) carried out a series of injections in radial a Hele-Shaw cell because of its applicability to radial flow from a well during fluid intrusion into porous media for oil recovery and gas storage. A fluid mobility term $M = \left(\frac{b^2}{12\mu}\right)$ was calculated for both the host and invading fluid. Using the mobility of the host fluid (M), the propagation front radius of the invading fluid in the Hele-Shaw cell (R), interfacial tension (γ_s), and injection rate (Q) the number of fingers created (n_m) and critical wavelength (λ) for displacement can be calculated as:

$$n_m = \frac{1}{3}\sqrt{\frac{QR}{2\pi M \gamma_s} + 1} \qquad (13)$$

$$\lambda = \frac{2\sqrt{3}\pi R}{\sqrt{\frac{QR}{2\pi M \sigma} + 1}} \qquad (14)$$

In other words, the invading fluid will have a circular leakoff front until the circumference reaches the critical wavelength, at which time an instability will occur and a finger will begin to propagate from the radial pattern.

Peters and Flock (1981) used a cylindrical packed column to verify a dimensionless term for the onset of instability taking place during the intrusion of water into an oil-saturated granular media. They verified that the dimensionless term proposed by Chouke (1959) correctly predicted the onset of an interfacial instability during their water flooding experiments when its value was greater than 13.56

$$I_c = \left(\frac{\mu_o}{\mu_w} - 1\right)\frac{V\mu_w D^2}{C^*\sigma k} \qquad \textbf{(15)}$$

This term is dependent on the ratio of oil viscosity to water viscosity (μ_o/μ_w), diameter of the cylindrical column (D), permeability (k), superficial flow velocity (V), wettability (C^*), and interfacial tension (σ) between the fluids. With all things being equal, an increase in the oil viscosity, an increase in flow rate, or decrease in permeability will lead to a high degree of instability during the water flooding.

In addition to studying Newtonian fluid instability, experiments have also been carried out using non-Newtonian fluids in Hele-Shaw cells (Daccord, 1986; Ben Amar, 1999; Kondic, 1996; 1998; 2001; Tordjeman, 2007). The shear thinning viscosity of non-Newtonian fluids leads to a shift in the instability regime and a change in the pattern formation in radial Hele-Shaw injections. Thinner, fracture like patterns were commonly observed in shear-thinning fluid experiments.

Kondic et al (1998) proposed a regime map based on a simple non-Newtonian power law model with viscosity given as a function of flow velocity (V) and shear dependence (α)

$$\mu = V^\alpha \qquad \textbf{(16)}$$

The regime map is scaled based on the dimensionless Weisenberg (We) and capillary (Ca) numbers. The We number measures the magnitude of the shear thinning effect and is a function of relaxation time, and Ca is a dimensionless number that quantifies the relative importance of viscous forces and surface tension. For a given fluid, an increase in We corresponds to an increased shear-thinning effect while an increase in Ca could be due to a higher flow velocity or

lower surface tension. The proposed instability regime patterns calculated through computer simulation are shown in Figure 6 based on input *Ca* and *We* values.
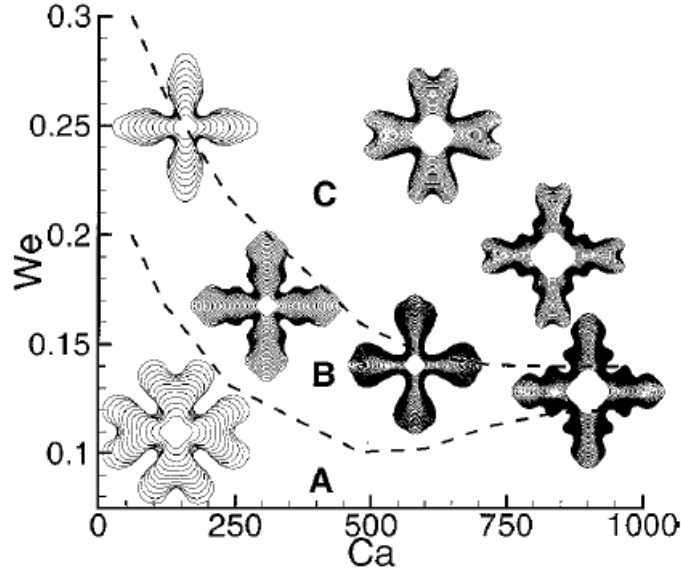
Figure 6: Tip behavior as a function of Capillary and Weisenberg number (Kondic, 1998)

Kondic et al (2001) hypothesized that in order to suppress tip splitting a fluid has to be strongly shear-thinning ($\alpha > 0.25$), and the viscosity must vary significantly across the interface front of the fluid. The relaxation time also plays an important role. As the fluid relaxation time decreases, the ability of the fluid to resist tip splitting increases. In Figure 6 above, region B is the bound for non-tip splitting behavior. With an increasing capillary number above ~500, the range for *We* at which fingers do not split will decrease.

The effect of shear thinning rheology on tip splitting can be seen by comparing two model injection simulations as seen below. In Figure 7 (a), a Newtonian fluid is injected and the instability manifests itself through finger growth and tip-splitting; however, in Figure 7 (b) a non-Newtonian fluid is modeled with the same capillary number, and tip-splitting is suppressed (Fast, 2001). An explanation of this was proposed based on the local viscosity at the tip

compared to the viscosity at the "fjord"/base region. In the non-Newtonian fluid, a high finger velocity at the tip induces shearing which in-turn decreases the fluid viscosity, allowing for preferential flow at the tip. This is in contrast with a purely viscous Newtonian fluid, in which case the viscosity is constant at any given location. The model for relative viscosity at various locations along the interface are shown in Figure 8 below; at each given time step the viscosity is lowest at the tip and approaches a high viscosity, low-shear limit at the base of the finger, or the "fjords". As seen in the graphical representation, the viscosity at the tip region is approximately 40% less than the effective viscosity at the base of the finger.
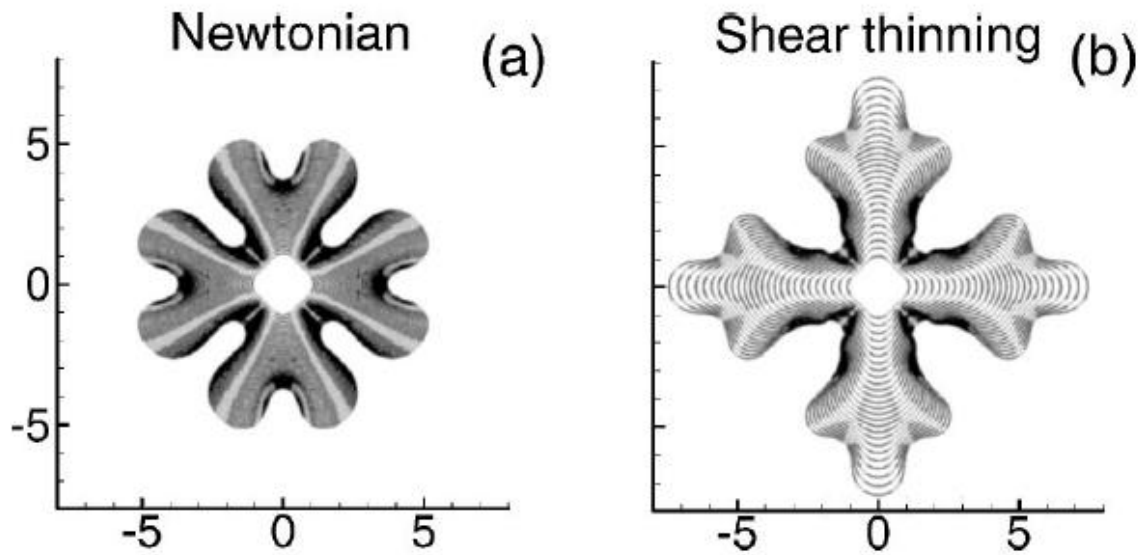
Figure 7: Difference in tip behavior for Newtonian (a) and shear-thinning (b) fluid injections
(Fast, 2001)
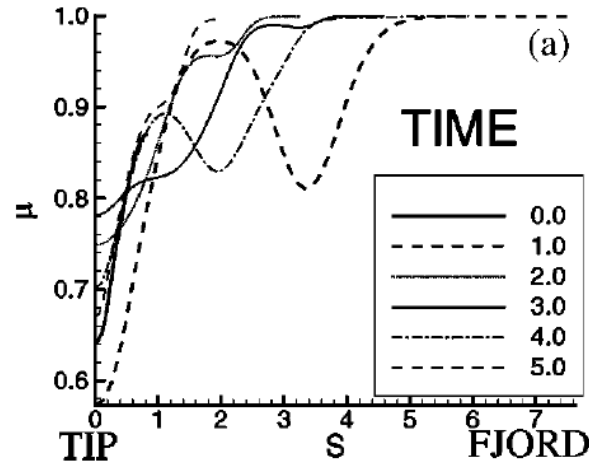
Figure 8: Viscostiy change at various locations and times for a non-Newtonian fluid (Fast, 2001)

2.4   Transition from Viscous Fingering to Fracture

In accordance with early work regarding the invasion of a less viscous fluid into another fluid, the transition from a viscous fingering type instability to a fracturing-type process has become an area of research interest.   The viscous fingering process is a result of surface instabilities at the interface between an invading and host fluid.   While at the other end of the spectrum hydraulic fracturing occurs due to structural instability due to stress concentrations and fluid pressure in an elastic medium.   In the fixed bed case when the process is governed by the capillary effect, flow regimes can be defined by the capillary number, a ratio of viscous to capillary forces.   The capillary number can be expressed in a variety of forms based on flow parameters according to (Lovoll, 2004)

$$Ca = \frac{\mu_0 V d^2}{\gamma_s \kappa}$$

(17)

21

where μ_0 is the fluid viscosity, V the flow velocity, d particle size, γ_s interfacial surface tension, and κ is the permeability.

Chevalier (2007) defined a relationship between capillary number and relative finger width for stable propagations for flow in Hele-Shaw cells. By using fluid suspensions with a variety of grain fractions and flow rates they were able to adjust the suspension rheology and capillary number, and a relationship between relative finger width $\lambda = w/W$ and a dimensionless control parameter $1/B = 12(W/b)^2 Ca$ was proposed. They concluded that the presence of grains in a suspension will cause a drop in the threshold value of capillary number at which a flow will destabilize.

Experimental work using non-Newtonain fluids in Hele-Shaw cells has shown thinner fractures with more branching patterns when compared to Newtonian fluid. For viscoelastic, non-Newtonian fluids a transition from viscous to elastic effects can be defined based on the Deborah number. The work of Lemaire et al (1991) varied the viscoelastic properties of a clay/water medium in a Hele-Shaw cell by changing the water content of the mixture, and injected Newtonian fluids into the medium. They were able to determine that at low concentrations of clay, the failure pattern was essentially similar to viscous fingering; rounded profiles and branching at smaller than 90⁰ angles at the finger tips. At higher flow rates in the rigid pastes the fingers turned into cracks with sharp tips and branching behind the tips. The observed experimental failure patterns can be seen in Figure 9. The fracturing regime was identified based on the perpendicularly branching growth. The researchers were able to create a phase diagram to predict the failure type based on clay/water ratios and injection rate, plotted in Figure 10. With fractal image analysis techniques it was found that the mass fractal dimensions of the viscous fingering injections were systematically higher than those of viscoelastic fractures,

due to the smoother fracture profiles. Several research studies on the growth of instabilities within Hele-Shaw cells (Daccord, 1986; Nittmann 1985) found that the fractal dimension of viscous fingering approaches the diffusion limited aggregation value of about 1.65.
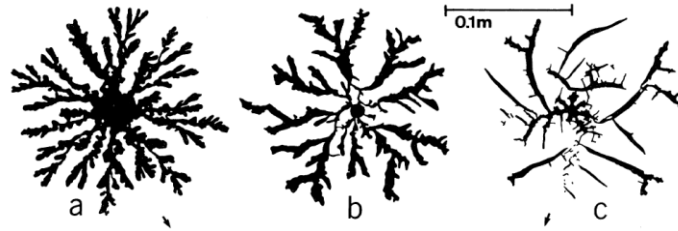
Figure 9: Change in fracture pattern as clay concentration is increased. (Lemaire, 1991)
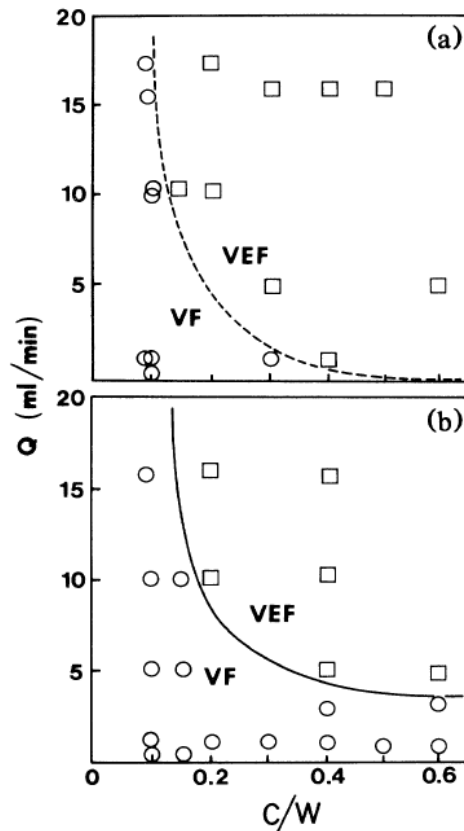
Figure 10: Regime map to predict the boundary between viscoelatic fracture and viscous fingering with change in flow rate and clay concentration (Lemaire, 1991)

McLean and Saffman (1981) studied the effects of fluid surface tension on the width of fingers inside a Hele-Shaw cell and found an increase in width with an increasing surface tension. Their results are more than likely due to a competition of capillary and fluid drag forces on the walls of the Hele-Shaw cell. An increase in surface tension would correspond to a subsequent decrease in capillary number.

The dependence of displacement shape on capillary number was studied by Lovoll et al (2004) using a linear Hele-Shaw cell. They found that by increasing the fluid flow rate, and thereby increasing the capillary number, the fracture patterns became thinner, the tip velocity increased, and the mechanisms of displacement were dominated by viscous forces. For their experiments, the transition from capillary fingering to viscous fingering with an increase in capillary number (a: Ca=0.027, b: Ca=0.059, d: Ca=0.22) can be seen in Figure 11.
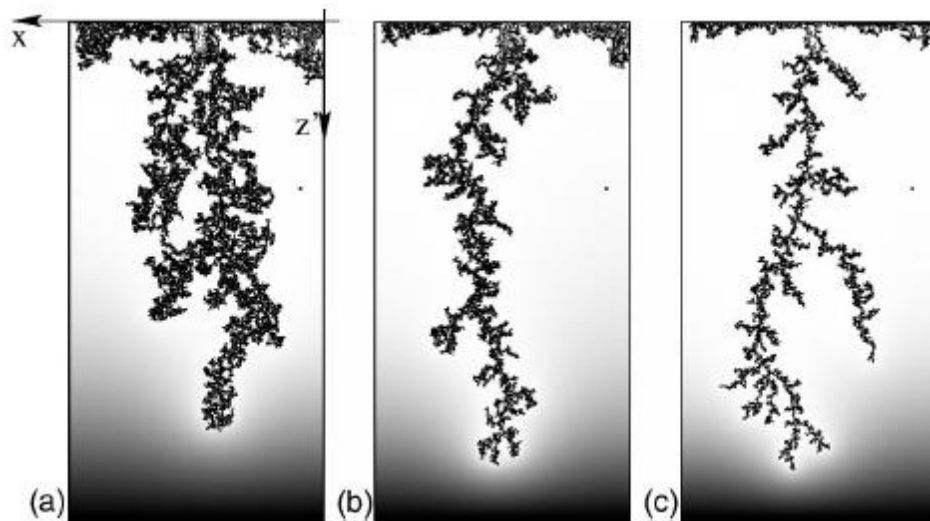
Figure 11: Transition from capillary fingering to viscous fingering as capillary number is increased from a: Ca=0.027, b: Ca=0.059, d: Ca=0.22 (Lovoll, 2004)

The work of Holtzman and Juanes (2010) hypothesizes that a transition from capillary fingering to viscous fingering occurs when the viscous pressure drop perpendicular to a particle exceeds the capillary entry pressure along the front. They used a particle scale model with interacting particle contact and pore pressure forces to determine the invasion pattern during fluid injection. Their numerical models defined a regime of capillary fingering, viscous fingering, and fracture based on a capillary number, pore scale disorder, and a dimensionless "fracture number". This fracturing number, N_f, is a ratio of the pore-scale pressure force and the force increment due to interparticle deformation. Using their numerical models a failure regime map was created and can be seen in Figure 12 below. Holtzman and Juanes's research also came to the similar conclusion that the fractal dimension of failure patterns will decrease as the failure regime migrates from a capillary fingering and viscous fingering regime in porous media, to a fracture regime.
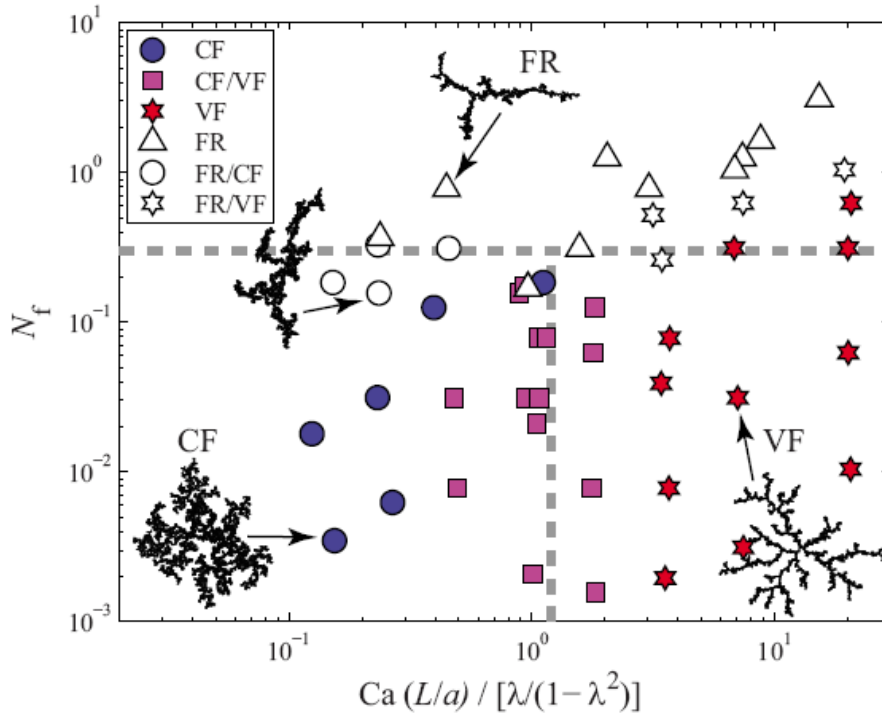
Figure 12: Regime map defining regions of capillary fingering, viscous fingering, and fracture (Holtzman, 2010)

2.5 Fluid / Particle Interaction

As seen in the preceding sections, the interaction of non-Newtonian fluids in granular porous media can take on many forms depending on a variety of factors such as fluid type, pore size, grain mobility, confining stresses, and flow rates. A description of the response for many of these studies is dependent on a particle level force balance. A starting point in understanding fluid / granular media interaction is to first consider fluid flowing around a single particle. The drag force on a spherical particle can be calculated based on the integration and combination of pressure drag and friction drag over the surface of a sphere. For a Newtonian fluid, the Stokes drag can be calculated based on velocity (V), viscosity (μ) and particle size (d_p) by

$$F_d = 6\pi\mu \frac{d_p}{2} V \qquad (18)$$

The contributions from the pressure drag and friction drag around a spherical particle are $2\pi\mu Rv$ and $4\pi\mu Rv$, respectively.

The ratio of inertial forces to viscous forces is expressed as the Reynold's number; at low flow rates (ie laminar flow, low Reynolds number) viscous forces are dominate, while at higher flow rates (turbulent flow, high Reynolds number) inertial effects inside the fluid element are more prevalent.

$$Re = \frac{\rho V d}{\mu_{ref}} \qquad (19)$$

A dimensionless drag coefficient which does not take into account inertial effects can be defined in terms of F_d and Reynolds number as:

$$C_d = \frac{F_d}{\left(\frac{1}{2}\rho V^2\right)\left(\frac{\pi d^2}{4}\right)} = \frac{24}{Re} \qquad (20)$$

This drag coefficient is sufficient for a laminar flow Reynold's numbers, however and a modified equation which accounts for fluid inertia can be defined:

$$C_d = \frac{24}{Re}\left(1 + \frac{3}{16}Re\right) \qquad (21)$$

By modifying the Newtonian Stokes equation, eqn 20 can be applied to other time-independent, shear thinning fluid types. For non-Newtonian fluids with viscosities defined by the Carreau power law equation, Chhabra and Uhlherr (17) found the drag coefficient can be calculated by

$$C_d = \frac{24}{Re}(1 + 0.15Re^{0.687})(1 + 0.65(n - 1))\Lambda^{0.20} \qquad (22)$$

$$\Lambda = \frac{2\lambda V}{d} \qquad (23)$$

In which Λ is a drag correction factor, λ a time constant dependent on relaxation time, d sphere diameter, n power law index, and Re_0 the zero shear Reynolds number based on the zero shear viscosity. Eq. 21 is a useful approximation, however it does not take into account viscoelastic and other time dependent effects seen in polymer solutions.

The drag coefficient for a single particle can be integrated for an assemblage of particles to calculate a modified Reynolds number and drag coefficient for Newtonian fluids in porous media. Similarly, the particle drag force can be calculated as a function of viscosity and porosity in the granular media. An increase in particle drag force is expected when particle diameter increases; this is due to a viscosity increase and a large surface projection for the fluid to act upon. As seen in Figure 13 the drag force increases with the particle size, and the response is more pronounced at higher flow velocities.
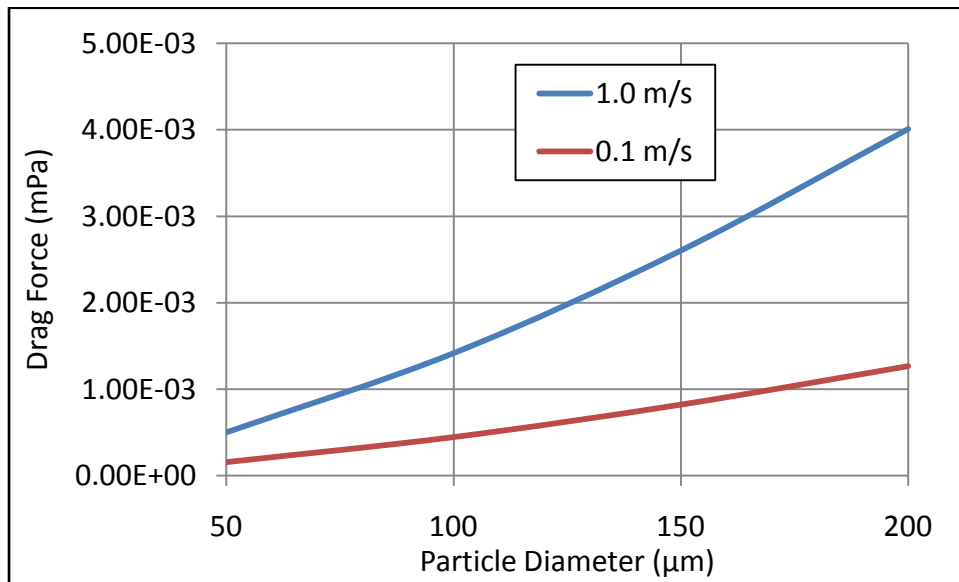
Figure 13: Particle drag force (Eq. 18) based on particle size for 0.1 and 1.0 m/s flow rate and polymer concentration of 0.75%. The polymer characteristics are based on power law and consistency indices identified by Ghannam (1998)

2.6   Flow in Porous Media

In the case where grain displacements are negligible, the soil skeleton can be considered rigid and Darcy's law governs the laminar flow behavior. The rate of energy loss is expressed as change in pressure over a given length, or as a dimensionless friction factor, f.

$$-\Delta p = \frac{\mu}{k} V \tag{24}$$

$$f = \left(\frac{\Delta p}{L}\right)\left(\frac{d_p}{\rho V^2}\right) \tag{25}$$

Similar to the dimensionless friction factor equation, a pressure loss can be calculated based on the Hagen-Poiseuille model using the Kozeny-Carman equation with porosity (ϵ) as an input parameter

$$\Delta p = \frac{72\mu VL}{d^2}\left\{\frac{(1-\epsilon)^2}{\epsilon^3}\right\}\left(\frac{Le}{L}\right)^2 \tag{26}$$

Le/L is a ratio of the effective length traveled by a fluid element. If it is assumed that capillaries deviate at an angle of 45 degrees from the mean direction of flow then the above equation can be rewritten as the Ergun equation:

$$\Delta p = \frac{180\mu V}{d^2}\left\{\frac{(1-\epsilon)^2}{\epsilon^3}\right\} + \frac{1.75\rho V^2}{d}\left(\frac{(1-\epsilon)}{\epsilon^3}\right) \tag{27}$$

 The left hand side of the equation accounts for laminar viscous pressure loss and the right hand side is a second order approximation for inertial effects, known as the Forchhiemer equation (Huang, 2008). The pressure loss can be explained as the frictional loss due to drag across a number of particles as the fluid is forced through the porous media. Figure 14 below demonstrates the effect of changing several model properties on pressure loss. It can be seen that

at low flow rates (red line) the particle size has less of an effect on pressure loss, however at higher flow (blue line) the pressure loss decreases significantly with increase in particle size.
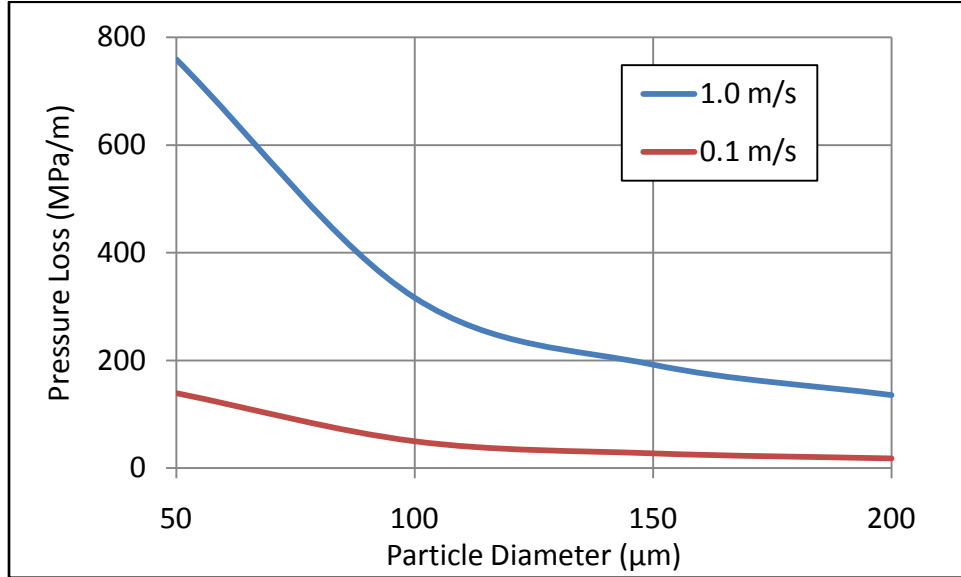
Figure 14: pressure loss (Eq 28) as a function of particle diameter at flow rates of 1.0 m/s and 0.1 m/s for polymer concentration of 0.75%

When dealing with flow of non-Newtonian fluids a wide array of difficulties arise due to time and rate dependent fluid characteristics. Due to the complexity of flow of non-Newtonian fluids, there is no definite description of the transition of flow regimes (Chhabra, 2007). There have however been some modifications to existing equations to account for non-Newtonian effects. The Kozeny-Carman equation has been adapted to include a modified Reynolds number (Re*) which is calculated for inelastic, power law fluids and incorporates both the power law (n) and consistency (k) indices. The friction factor for non-Newtonian fluids can be calculated:

$$\mathbf{f}\left\{\frac{\epsilon^3}{1-\epsilon}\right\} = \frac{\mathbf{180}}{\mathbf{Re}^*} \tag{28}$$

$$\mathbf{Re^*} = \frac{\rho V_0^{2-n} d^n}{k(1-\epsilon)^n} \left(\frac{4n}{3n+1}\right)^n \left(\frac{15\sqrt{2}}{\epsilon^2}\right)^{1-n} \qquad \text{(29)}$$

Although the aforementioned equations can account for some non-Newtonian fluid and porous media properties, a number of effects such as viscoelasticity have not been accurately quantified. Because of viscoelastic and shear thinning effects and extensional strains with porous media, a sufficient model for pressure loss for viscoelastic fluids has not been obtained. Elastic effects of polymer solutions arise because of flow contraction and expansion. As fluid is constricted in pore throats, elongational strains cause polymer chains to stretch and a normal stress is transferred to the particle walls. The energy associated with this process results in higher than expected pressure loss.

Along with rheological effects, other complications may arise during the flow of non-Newtonian polymer solutions in porous media. As the fluid flows though pore spaces it is possible for polymer chains to be adsorbed or entrapped against individual grains. This not only "clogs" pore spaces leading to a drop in permeability, but also decreases the overall concentration and viscosity of the flowing pore fluid. Mechanical degradation of polymer chains has also been identified during porous flow, caused by shearing and extensional strains in pore throats (Bestul, 1956; Haas, 1984).

2.7   Coupled Fluid / Granular Media Displacement Process

As stated in previous sections, the response of a granular system can take on many forms depending on flow and in-situ conditions; from porous infiltration to viscous fingering to viscoelastic fracture. If the granular media is loosely packed the fluid invasion process can act analogously to a Saffman-Taylor instability, modeled as one viscous fluid invading a more

viscous fluid. In this case the mechanics of the granular suspension are be governed by lubrication and collisional forces, and an effective viscosity of the system can be estimated based on grain fraction. If the host granular media is densely packed it may act more like a fixed bed condition dominated by frictional forces transmitted throughout the soil skeleton induced by the invading fluid.

As fluid is injected into a porous granular media an unbalance of forces may occur which results in a deviation from a fixed bed model due to the rearrangement of the soil skeleton. And unlike brittle solids which fail in tension at the crack tip due to cementation between grains, unconsolidated / uncemented granular media fail due to compressive loading mechanisms (Chang, 2004; Wu, 2006).

Chang (2004) and Wu (2006) both proposed a failure mechanism based on a modified Dugdale-Barenblatt model; in which the entire material is considered to be in compression with an elastic region adjacent to the fracture walls and no grain cohesion. A schematic of this model is presented in Figure 15. It is assumed the fluid pressure reduces the stress (σ_{yy} at the tip region 2, 3) to below the far field stress. Therefore the stress components come in contact with the Coulomb failure surface. As the particles in the tip region become unloaded, fluid is forced into the region and localized flow occurs. The Mohr-Coulomb model can be used to describe material yielding.
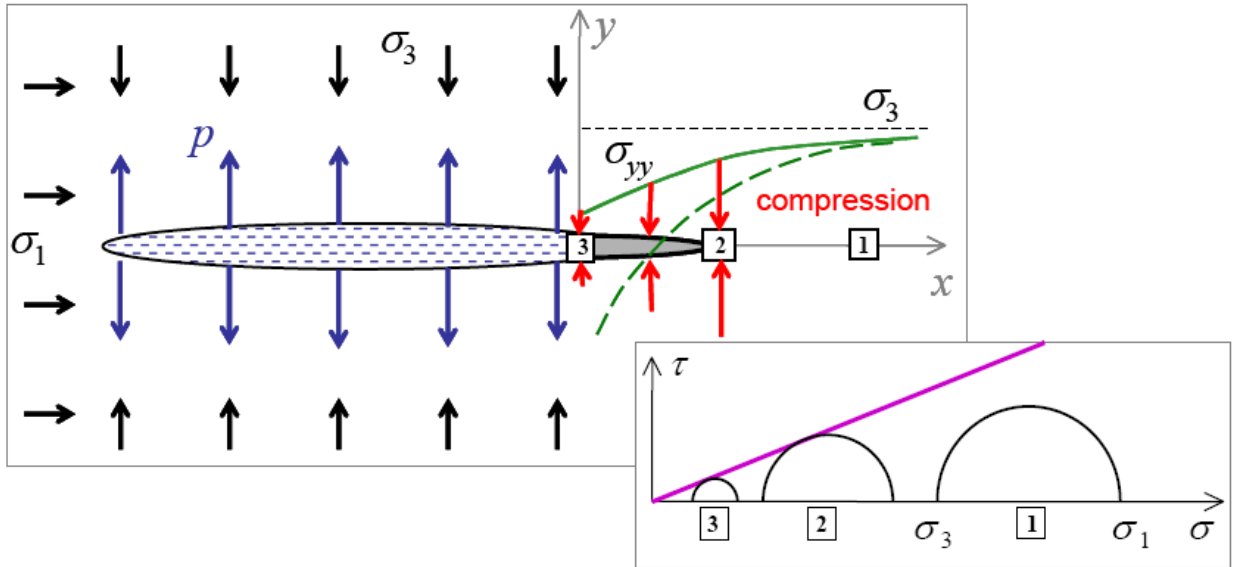
Figure 15: Proposed stress profile for a pressurized crack in cohesionless granular media
(Chang, 2004)

In addition to the process zone model described above, Wu (2006) proposed a second model of fracture in cohesionless material based on crack tip plasticity and a "super-dislocation" theory. This model uses slip planes as an analog for the plastic zone surrounding the fracture tip. The position, angle, and strength of the dislocation are determined from a zero stress intensity factor at the tip with stresses following the Mohr-coulomb criterion. Figure 17 presents a schematic model of the "super-dislocation" theory.
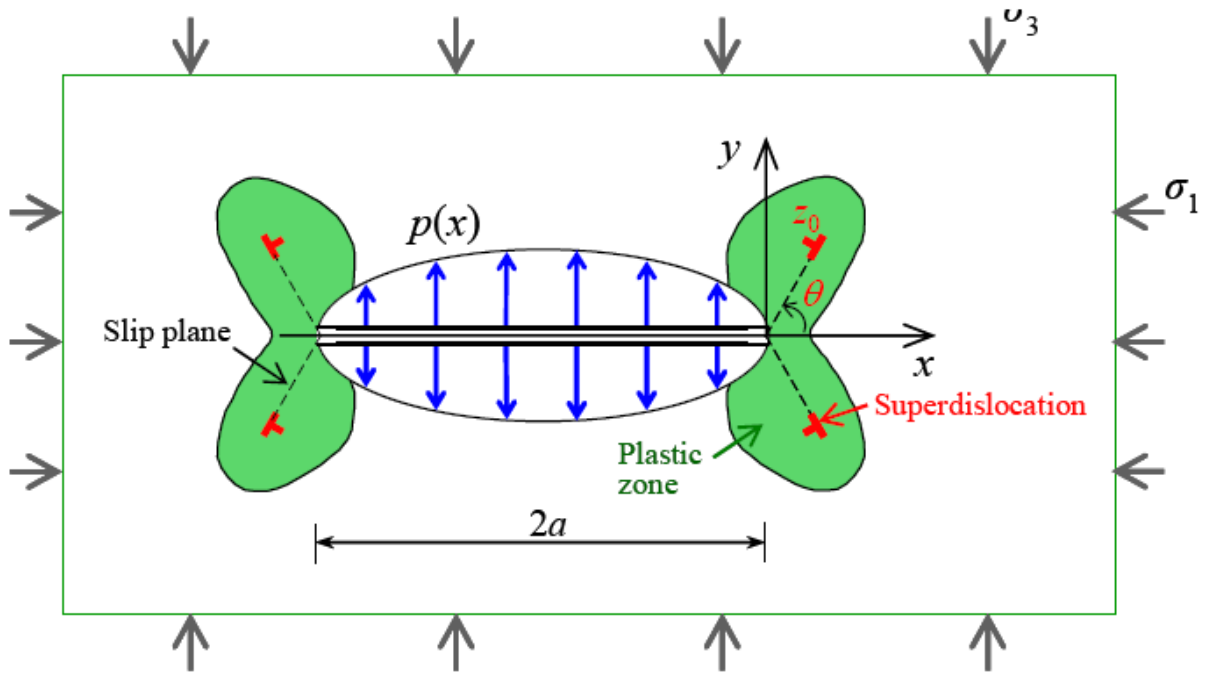
Figure 16: Schematic of superdislocation model (Wu, 2006).

Along with theories considering general failure criterion, the mechanisms taking place during fluid invasion in granular media can be accounted for by particle-level forces such as weight of the grains, skeletal forces due to effective stresses, capillary forces, and particle drag forces. For injection into a dry granular media the fluid initially imposes immiscible capillary forces at the fluid front due to surface tension, then transitions to miscible drag forces as the fluid infiltrates further into the porous media and the injection point becomes saturated. This can be qualitatively described as a combination of capillary and drag forces as seen in Figure 17.
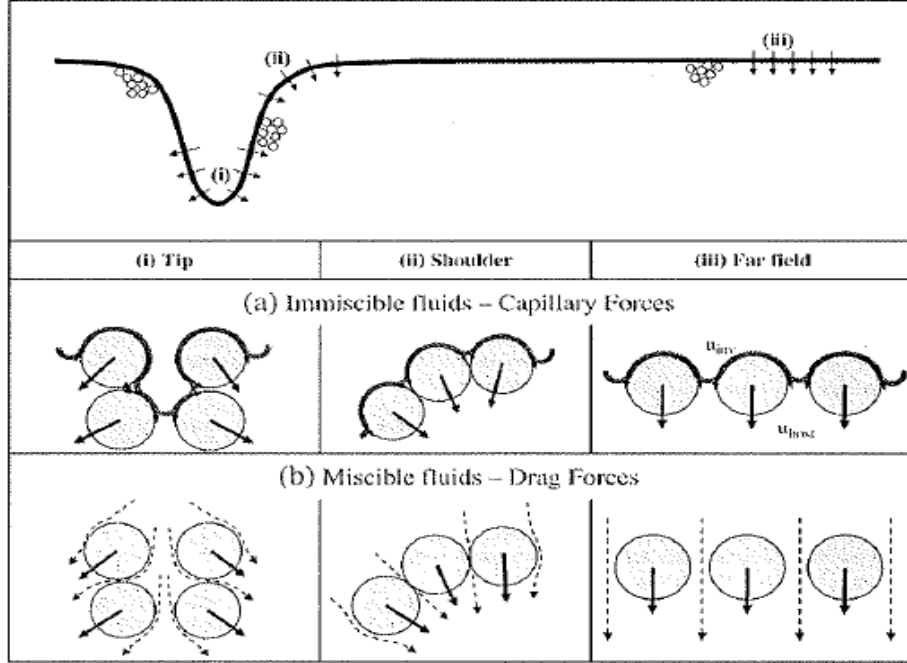
Figure 17: Capillary and drag forces acting on soil skeleton with fluid invasion (Shin, 2010)

The work of Shin and Santamarina (2010) hypothesized a hydraulic fracturing regime based on capillary, skeletal, and seepage forces. The graphical results of Figure 18 show that four opening mode regimes are possible based on a balance of the given forces. Specifically, from a micro-scale point of view, the ratio between capillary and seepage forces to skeletal forces is critical for determining the granular media response. Other particle-level forces such as electrical attraction, cementation, and buoyancy could be included based on particle size and system considerations (Santamarina, 2001). Each of the particle level forces is based on surface tension (T_s), particle size (d_s), viscosity (μ), flow velocity (v), and given as follows:

$$\text{Capillary: } F_C = \pi d_s T_s \cos\theta \tag{30}$$

$$\text{Skeletal: } F_{sk} = \sigma' d_s^{\,2} \tag{31}$$

$$\text{Seepage: } F_s = 3\pi\mu d_s v \tag{32}$$
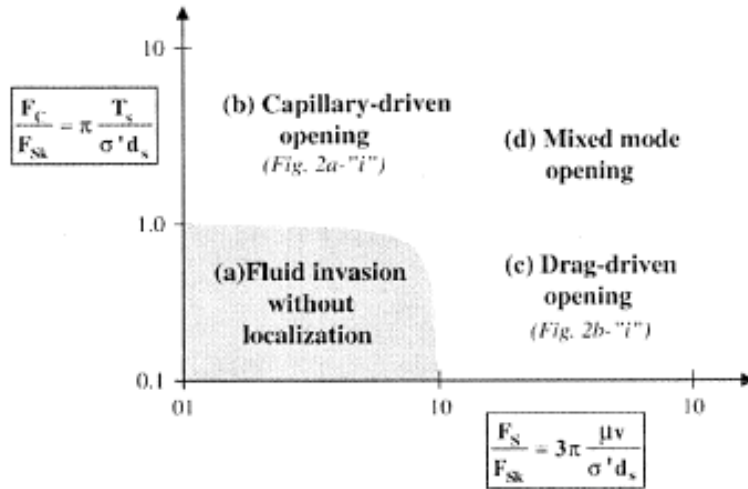
Figure 18*: Flow regime based on ration of particle-level forces (Shin, 2010)*

The four regimes are defined based on ratios of forces. If neither the seepage nor capillary forces are larger than skeletal forces, fluid invasion occurs without significant rearrangement of particles. If a large seepage force is present with still relatively low skeletal forces, drag-driven fracture opening will occur. On the other hand, if capillary forces are high due to surface tension and drag forces low, a capillary-driven opening is expected. As seen in the equations above, many of the characteristic functions are non-linearly related to parameters such as particle size, porosity, and flow properties. This model and failure regime presents a conceptual understanding of the balance between particle-level forces.

A 2-D particle-level study involving discrete element simulation of water flooding into particulate media was carried out by Wu (2006). Three distinct growth stages were observed: cavity expansion, stable cavity development, and unsteady cavity propagation. During the initial stages of injection the particles become detached from one another and a "fluidized" system is created leading to the creation of an initial cavity. A subsequent simulation of particle

36

deformation is shown in Figure 19(b); as the injection velocity is increased, an increased drag on the particle assembly creates an unbalance in the stress field and unstable cavity propagation occurs. The two simulations do not account for surface tension or capillary forces but do factor in particle-level deformations due to a hydrodynamic response.
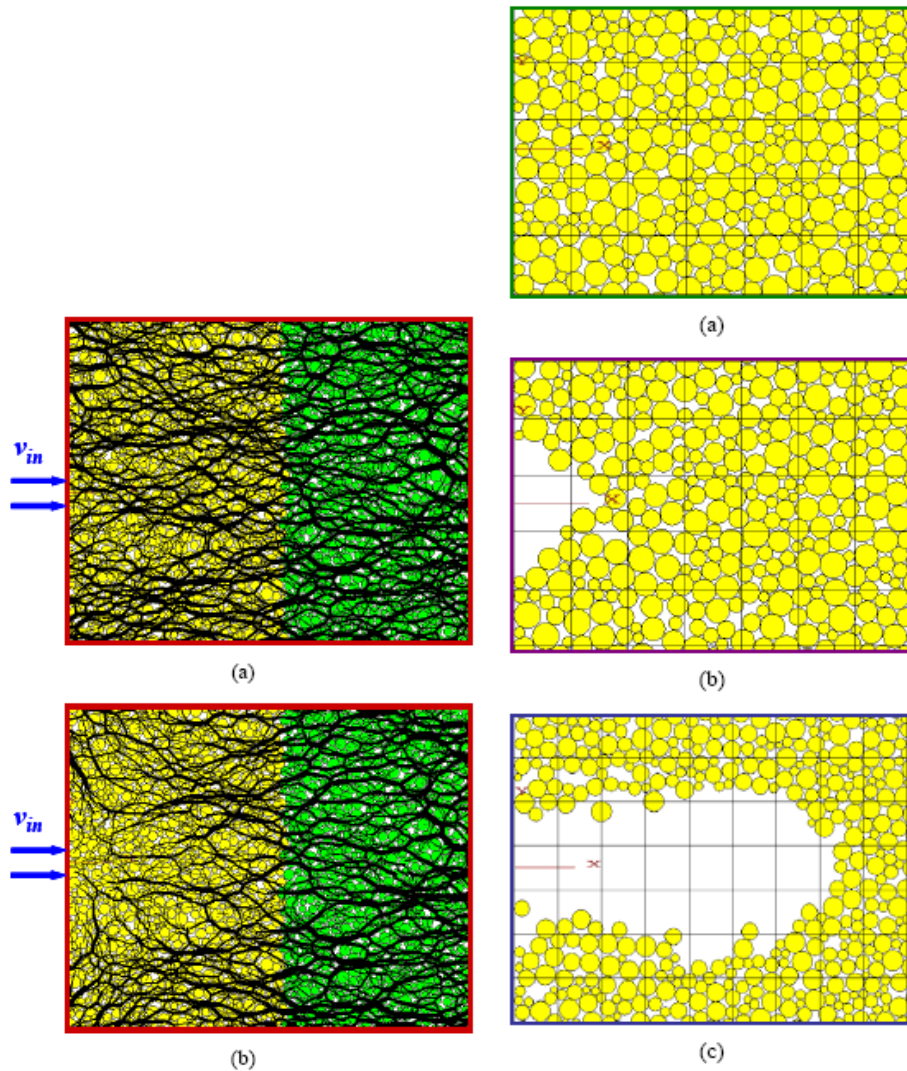
Figure 19: (a) Change in force chains present near an injection inlet; (b) particle deformation during the cavity expansion, stable cavity development, and unsteady cavity propagation stages (Wu, 2006)

Wu (2006) also found that the critical value for cavity "fluidization" is determinant on both injection velocity and fluid viscosity, corresponding to the inertial and viscosity dominated regimes. A critical injection velocity was determined based on the minimum injection rate at which cavity formation is possibly for any given fluid viscosity. The relationship between the critical velocity and fluid viscosity can be found in Figure 20 below. As expected, the minimum velocity needed to initiate cavity expansion decreases with an increasing fluid viscosity due to an increase in drag force subjected on the particle assembly.
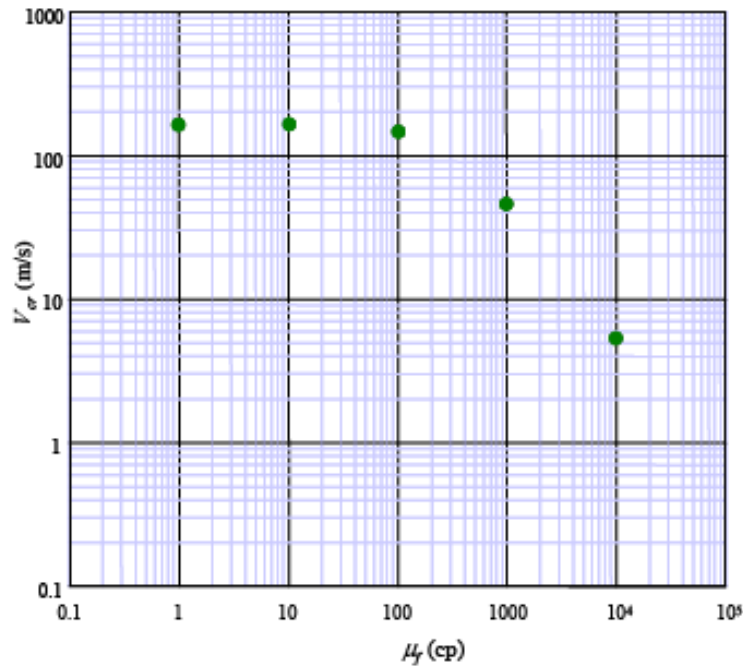
Figure 20: Calculated critical velocity needed to induce fracture propagation (Wu, 2006)

2.8   Previous Laboratory Experiments

A number of laboratory scale experiments have been conducted to study the effects of parameters on the failure/flow mechanisms taking place during fluid injection into granular

media. Due to a variation in testing conditions several leakoff and fracture patterns and have been observed. The patterns in these experiments are the result of the coupling between fluid flow and mechanical deformation of the particulate material.

Khodaverdian and McElfresh (2000) conducted research to understand and predict the injection pressure for fracture stimulation in unconsolidated sand formation. It was found that for the injection tests with lower fluid efficiency (allowing for higher leakoff), the net propagation pressure is higher and the resulting fractures are branched. It was also seen that fluidization at the fracture tip and shear failure results in tortuous, multiple branching fractures. When filter cake building fluids are used the net pressure is reduced and fewer branches are observed. The pressure and fracture response was hypothesized to be due to shear induced dilation and effective stress reduction which lead to local permeability increase. They came up with an idea of "pseudo-fractures" which are created due to a combination of fluid mobility and formation damage. Fluid mobility causes local shear failure and high permeability flow conduits while formation damage is caused by clogging of pores and filter cakes (Khodaverdian, 2010). A schematic of the two psedo-fracture mechanisms is shown below in Figure 21.
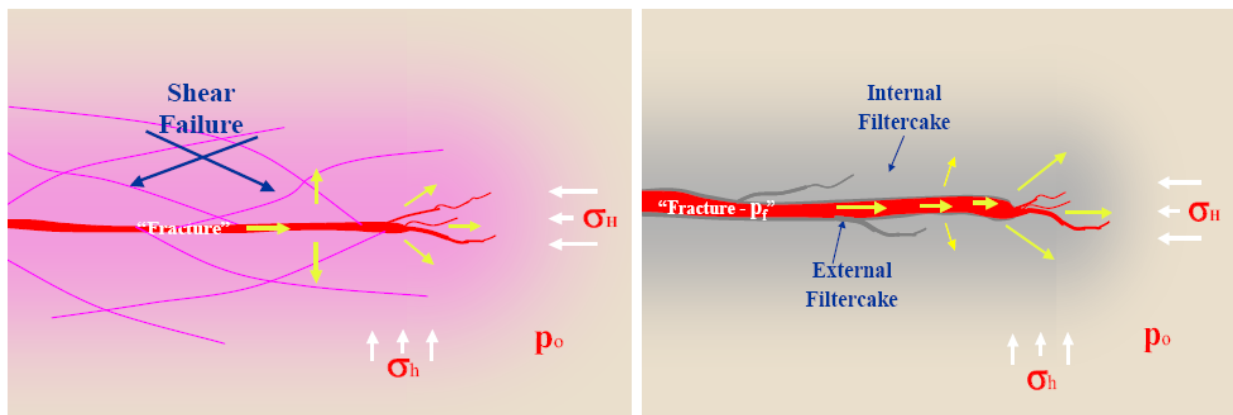
Figure 21*:* "Pseudo fractures", mobility driven (a) and formation driven (b) (Khodaverdian, 2010)

A series of small-scale and large-scale laboratory injection tests were carried out by Chang (2004). In her work the effects of both granular media and fluid properties were studied. Four types of particulate media at various relative densities were used: fine sand, sand and silica flour mixture, Georgia red clay, and silica flour. Fractures observed in each of the different particulate media exemplify a wide range of shapes and sizes; from a rounded leakoff bulb in fine sand, to sharp fingered fractures in Georgia red clay. The effects of the samples' relative density were also compared. Tests yielded thinner and smoother fractures at higher density. Injection tests showed that high viscosity resulted in thicker, beveled fractures. A series of large-scale tests were also performed to study the effect of confining stress anisotropy on fracture patterns. It was found that as vertical load is increased, fractures migrated from fingered fronts to thicker, more rounded edges. The research of Robert Hurt using injections into saturated sand in a large-scale triaxial apparatus has also studied the flow/failure response.

Huang et al (2011) defined four failure/flow regimes in their experiments injecting Newtonian glycerin solutions into a sand-filled, radial Hele-Shaw cell. The experiments varied fluid viscosity and injection rate in order to identify a wide range of flow/failure conditions. Four failure/flow regimes were observed: i) simple radial flow, ii) infiltration-dominated, iii) grain displacement-dominated, and iv) viscous fingering-dominated dissipation. It was argued that the failure/flow regimes emerge as a result of competition among several energy dissipation mechanisms: viscous dissipation through flow in porous media, dissipation through mechanical deformation, and viscous dissipation through flow in thin channels.

Injection tests have also been performed by a group of researchers at the TU Delft in which injections were carried out in triaxial test conditions with varying parameters of confining

stress, fluid rheology, permeability, and strength (de Pater, 2007; 2009; Dong, 2008; 2009). In these experiments the fracturing and leakoff characteristics were identified using x-ray CT scanning to obtain real-time measurement of fracture geometry, as well as excavation of the sample after injection to observe patterns directly. In their first set of experiments (2007), tests were carried out in a radial, triaxial test cylinder in which the confining stresses were varied from 0.7 – 7 MPa. The group used three fluid types: a viscous Newtonian fluid, bentonite slurry, and cross-linked gel with some of the fluids having added silica flour particles. In tests with the Newtonian fluid it was found that fractures were only initiated for the case of low confining stress and high flow rate; at high confining stress and low flow rate only cylindrical leakoff was observed. During tests with bentonite slurries, fractures were unable to form; rather, large borehole expansion was observed with shear bands emitted radially. For the stable cross-linked gel under high confining stresses borehole expansion was again seen, however fractures were initiated at low confining stress. Lastly, a mixture of silica flour was added to the cross-linked gel in order to improve on its wall-building capability, and fractures were created in all tests even up to confining stresses of 40 MPa.

A subsequent study by de Pater and Dong (2008) concluded that fluids which allow for high leakoff often only result in borehole expansion and shear banding, however, fluids which induce filter-cakes at the fluid/granular interface tend to propagate fractures and allow for smooth closure at the fracture tip. It was found that fractures in low-permeable layers of uncemented granular media are more likely to initiate and propagate than high-permeable formations. This is more than likely due to low infiltration which leads to a higher contrast in effective stress near the fracture tip (Dong 2009).

Numerous other research has studied the effects of experimental parameters on fracture formation. Golovin et al (2010) found that based on initial stress, fluid type, and injection rate the response can be classified as either flooding, cavity formation, single fracture formation, or multiple branching fractures. Similar to the results of the Delft group, the percent of solids in the injection fluid is directly related to the type of fracture formed; with planar fractures forming at high solids concentration and a diffuse fracture network with low solids concentration. They also found that fracture pattern is related to injection rate, resulting in linear cracks and little branching at low flow rates, and multi-branch stochastic fractures forming at high flow rate.

A schematic of the variety of fracture and leakoff patterns observed by the various research groups in presented in

Figure 22.
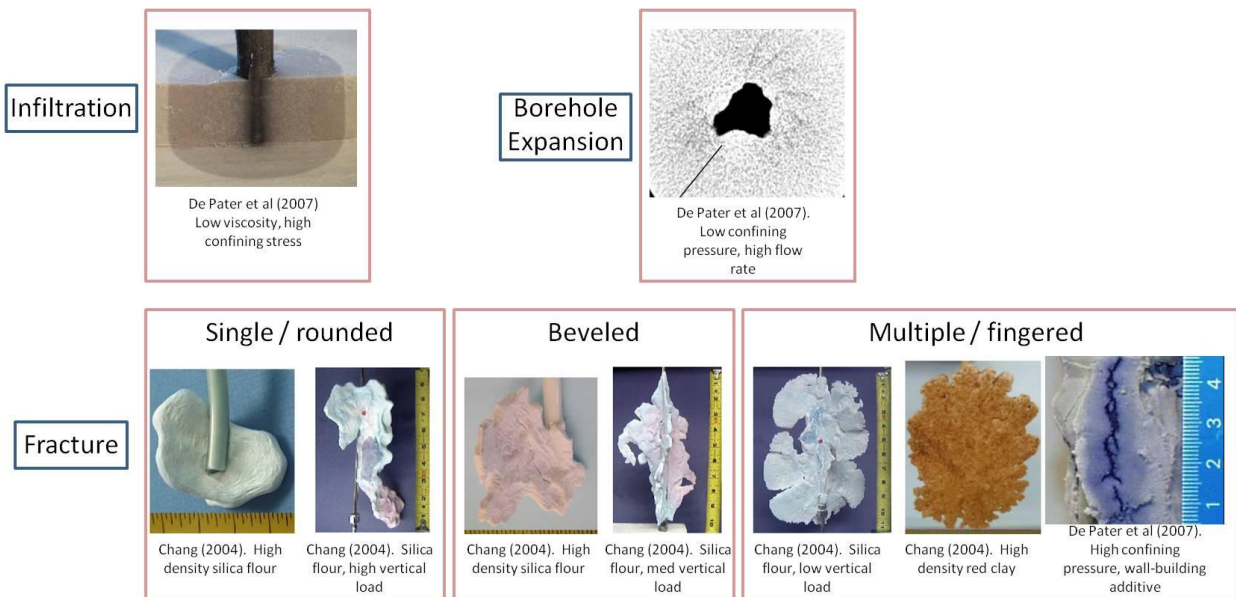
Figure 22: Schematic of the variety of fracture types created as a function of testing parameters

CHAPTER 3

HELE-SHAW EXPERIMENTS

3.1   Experiment Setup

In order to visualize the injection process and fluid/grain interaction we chose to conduct our series of experiments in a transparent radial Hele-Shaw cell. The cell was constructed from two, one-inch thick polymethyl methacrylate (PMMA) plates measuring twelve inches on each side. The narrow opening and wide surface area is representative of a plane-strain condition. The plates were fastened together using four stainless steel bolts in each corner. The gap separation between the plates could be varied using different sized metal shims which allowed for a gap thickness of 0.031" to 0.125".   An injection port was drilled into the bottom of one of the plates and the diameter of the injection hole measured 1.02 mm.

The set up of our Hele-Shaw cell is very similar to other experiments carried out to study viscous fingering instability. However, rather than using a fluid to fill the gap within the cell, in our experiments the Hele-Shaw cell was filled with Ottawa F-110 sand from U.S. Silica, with a particle size distribution of ~100-200 microns. A consistent method was implemented to obtain uniform sand packing within the Hele-Shaw cell. It was sealed on three sides and filled in a series of successive lifts. After each lift the cell was placed on a vibratory compactor to achieve dense packing. After the cell was filled, the fourth side was sealed and it was rotated on each side on the vibration table in order to achieve a uniform compaction in all directions. Any excess voids after compaction were filled. The cell was calibrated to determine the exact volume available for filling, and an initial and final weight was recorded to calculate the exact grain fraction for each test.

The Hele-Shaw cell filled with dry sand was positioned horizontally atop the laboratory table and connected to the injection pump via an inlet on the underside of the cell. In order to collect image data for each injection series a Canon Vixia HFS100 high-definition camera was positioned over the Hele-Shaw to take a series of photos throughout the injection. A schematic of the experimental setup can be seen below.
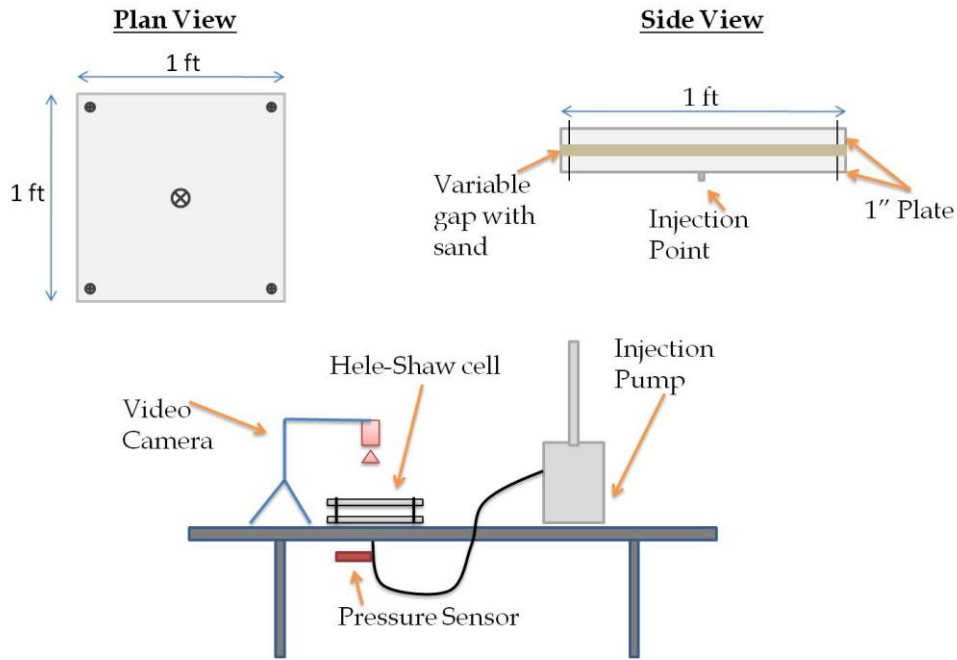
Figure 23: Schematic of experimental setup and material properties

3.2   Sample Properties

The permeability of the sand was determined using a flexible wall permeameter according to ASTM Standard D5084. At a confining stress of 20 psi the permeability was calculated to be $k = 739$ mD. It is expected that the compaction in the permeability test was slightly lower than compaction within the Hele-Shaw cell because tamping was used rather than the vibration table. A drained triaxial test was also performed following ASTM Standard, and

the F-110 sand was found to have a small strain elastic modulus of $E = 66.2$ MPa and an internal friction angle of $\phi = 43°$. The table below and corresponding figures show some typical material properties of Ottawa F-110 sand.

Table 1: Characteristic values of Ottawa F-110 sand including particle shape, packing, and density (Chang 2004, MSDS)

Particulates		Ottawa Sand F110
Type		Fine sand
Mineral		Quartz
Color		White
Grain shape		Round
Specific gravity		2.65
Void ratio	Maximum	0.85
	Minimum	0.54
Porosity	Maximum	0.46
	Minimum	0.35
Dry density	Minimum	1.43
(g/cm^3)	Maximum	1.73
Angle of repose		27
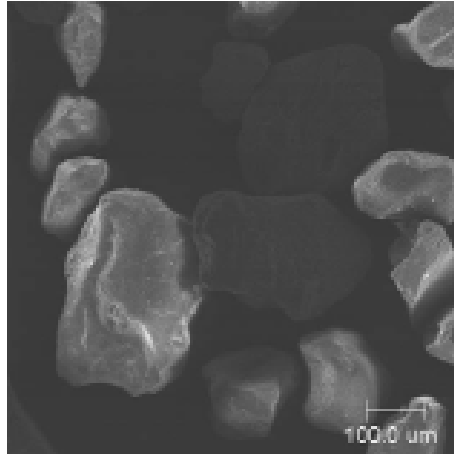
Figure 24: Microscopic view of Ottowa F-110 sand (Chang 2004)
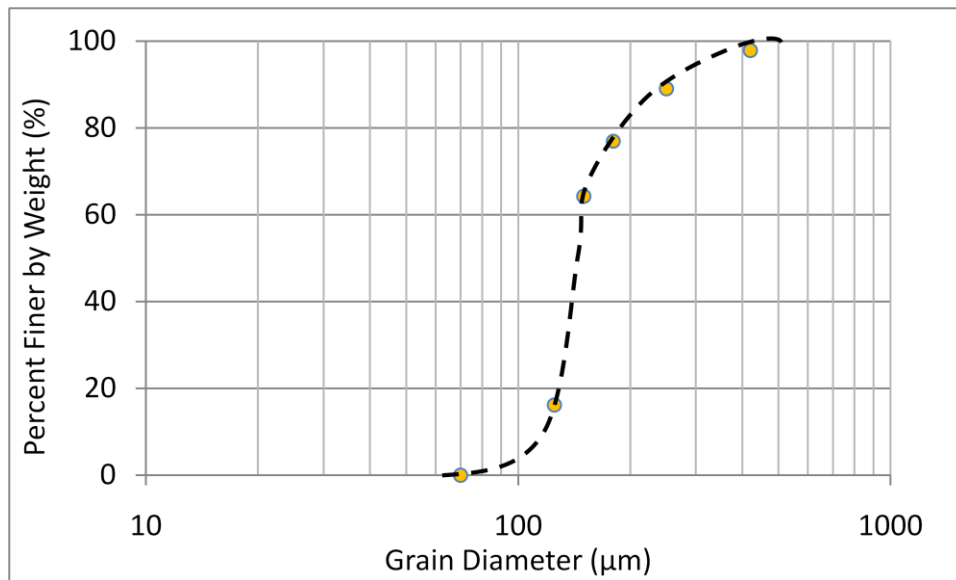
Figure 25: Particle size distribution of Ottawa F110 sand (fine sand) compared to other natural materials (Georgia Red Clay and Silica Flour) (Chang, 2004)

A series of tests were carried out at a range of solution concentrations and injection rates. For polyacrylamide solutions, the polymer chains are derived from acrylic acid groups with the size of the molecules ranging from about 0.1-0.3 μm. When the solid form of polyacrylamide is

hydrolyzed in water the acrylamide groups react to form dissociated carboxyl groups (COOH), and the negatively charged carboxyls cause the polymer chains to stretch and intertwine. Changes in ionic concentration in the solvent have a large effect on solution viscosity and polymer chain length. Mechanical degradation due to high shear rates is also a potential problem; polymer chains can be broken due to high shearing when injecting through perforated injection inlets (Bestul, 1956). The molecular weight of the pure polyacrylamide was listed as 5,000,000 – 6,000,000 mol/L.

The polyacrylamide (PAAM) solutions were made from a mixture of powder PAAM and deionized water. The solutions were mixed for several hours using a low-speed magnetic bar stirrer in order to prevent mechanical and shear-induced degradation of the polymer chains. No visible polymer globules, or "fisheyes", were seen in any of the solutions.

3.3   Procedure

To carry out the injection tests, the Hele-Shaw cell was connected to a Teledyne Isco Series 500D pump. The pump has the capacity to run at either constant flow-rate (0-170 mL/min) or constant pressure settings. This set of experiments only utilized the constant flow-rate operation. The pump is equipped with a pressure sensor at the injection outlet, however this overestimates the actual pressure inside the Hele-Shaw cell due to the pressure losses in the 1.5 meters of injection tubing connecting the pump to the cell. In order to overcome this error an extra pressure sensor was placed at the cell inlet for a more accurate prediction of pressures inside the cell. The new pressure sensor is capable of readings at 400 Hz and transfers pressure data wirelessly to the computer.

Post processing of the data collected during each test included gathering pressure data files and compiling photos. The raw data is stored as a .txt file and post processed using a

Matlab script. With a continuous shooting mode for the camera, each test resulted in 20-300 still images depending on the duration of the test. To extract image analysis data from the series, 10 pictures at even time intervals throughout each test were selected. A sample series of these pictures can be seen below in Figure 26. The lightest gray area is dry sand, the dark gray is the infiltrated region, and the black is the fractured area.
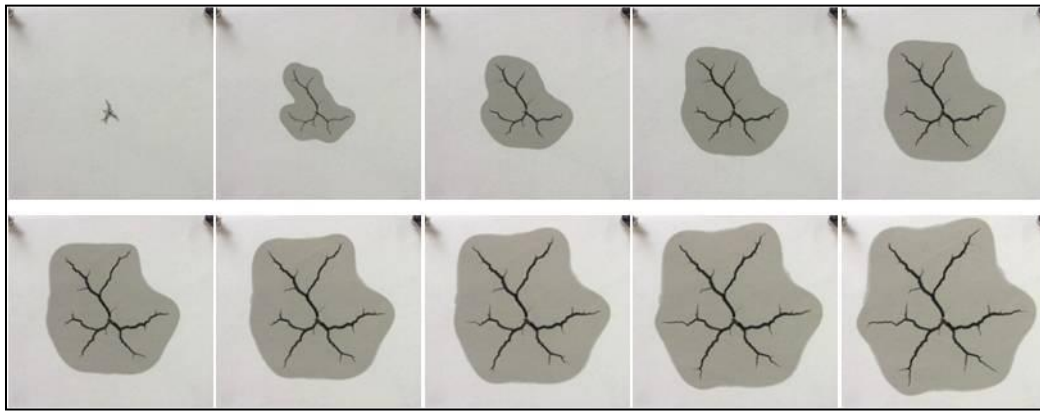
Figure 26: Image sequence for 0.5% solution concentration at 10 ml/min

Table 2 presents a complete list of every polyacrylamide test completed. The table is color-coordinated based on the solution concentration. In all, data was collected for 34 tests. For each concentration (0.10%, 0.50%, 1.00%, 1.50%, and 2.00% polyacrylamide by weight) the injection tests were conducted at a rate of 5.0 mL/min, 10.0 mL/min, 25.0 mL/min, 50.0 mL/min, and 100 mL/min.

Table 2: List of completed tests

Date	Concentration	Injection Rate (ml/min)
15-Nov	0.10%	10
31-Jan	0.10%	25
31-Jan	0.10%	5
31-Jan	0.10%	100
2-Feb	0.10%	5
2-Feb	0.10%	100
2-Feb	0.10%	5
15-Nov	0.10%	50
19-Nov	0.50%	1
19-Nov	0.50%	10
19-Nov	0.50%	25
19-Nov	0.50%	100
23-Nov	0.50%	50
11-Nov	0.50%	5
15-Nov	0.50%	50
23-Nov	0.50%	5
16-Nov	1.00%	10
16-Nov	1.00%	50
26-Jan	1.00%	25
30-Jan	1.00%	5
26-Jan	1.00%	100
26_Jan	1.00%	5
18-Nov	1.00%	2
21-Feb	1.50%	5
21-Feb	1.50%	10
21-Feb	1.50%	25
21-Feb	1.50%	50
21-Feb	1.50%	100
8-Dec	2.00%	10
8-Dec	2.00%	50
8-Dec	2.00%	25
10-Dec	2.00%	100
10-Dec	2.00%	5
10-Dec	2.00%	1

CHAPTER 4

EXPERIMENT RESULTS

4.1   Rheology Calculations

As described in the preceding sections, the flow behavior response of non-Newtonian polymer fluids can vary greatly based on a flow conditions.   Time and rate-dependent characteristics such as viscosity and viscoelasticity play a very important role in the fluid/particle interaction mechanisms within the Hele-Shaw cell.   In order to quantify the rheological properties of the polymer solution, a Carreau power-law model has been employed to fit rheology data obtained directly through laboratory testing using the cone-plate and Couette viscometers.   The Rheology curves for each solution concentration (0.10%, 0.50%, 1.00%, 1.50%, and 2.00%) used during our injection experiments can be seen in Figure 27.
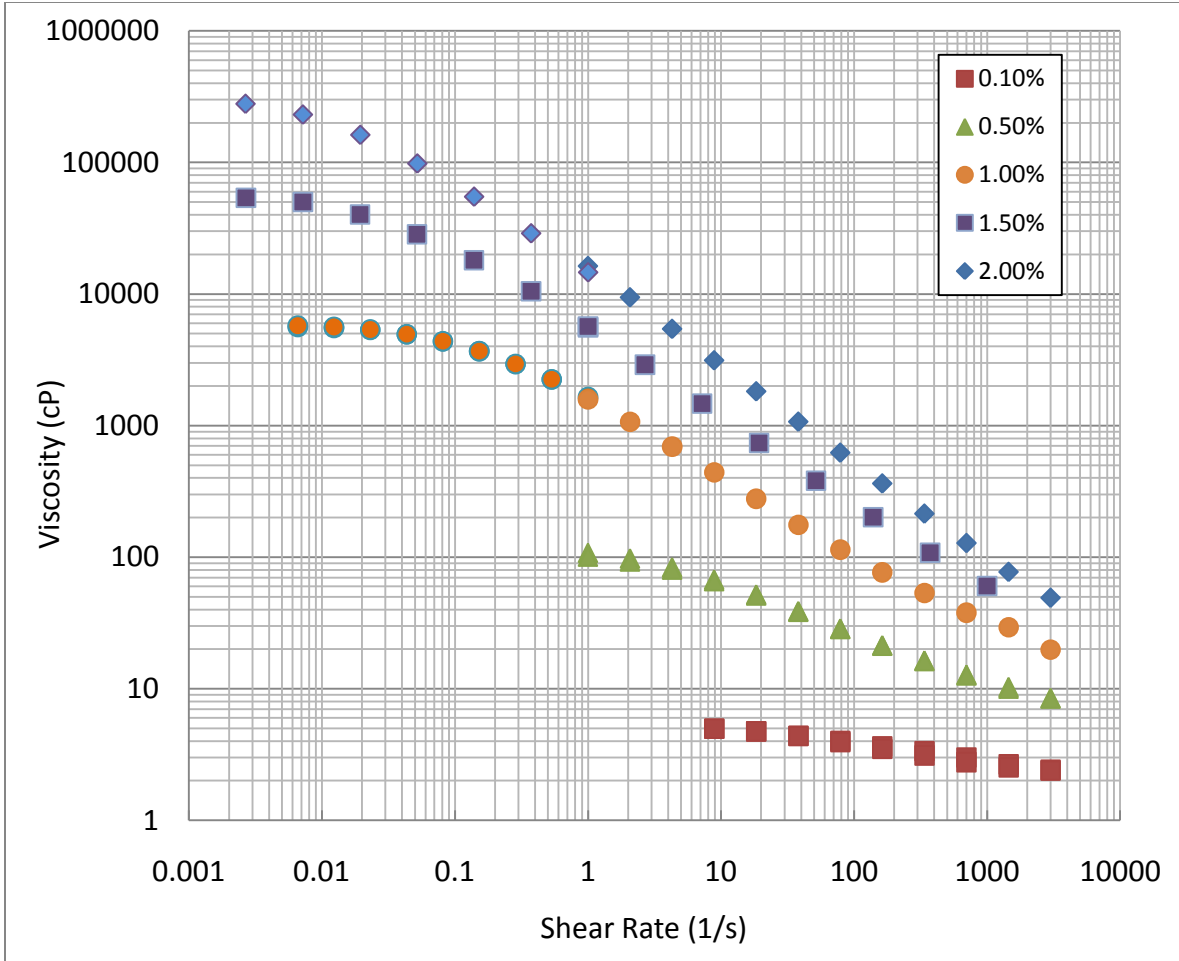
Figure 27: Rheology data for all five solution concentrations (courtesy of Kyung Oh and Dr. Victor Breedveld's complex fluid laboratory)

The shear thinning and pseudoplastic effects can clearly be seen in the rheology data. At the low-shear rate there exists a constant viscosity plateau, while shear-thinning occurs after a critical shear rate is reached. The laboratory rheology data was fitted to the Carreau power-law equation (Figure 28) where μ_o is the low shear viscosity, μ_∞ the high shear viscosity, n power law index, $\dot{\gamma}$ shear rate, and λ relaxation time:

$$\frac{\mu-\mu_\infty}{\mu_0-\mu_\infty} = [1 + (\lambda\dot{\gamma})^2]^{(n-1)/2} \tag{33}$$
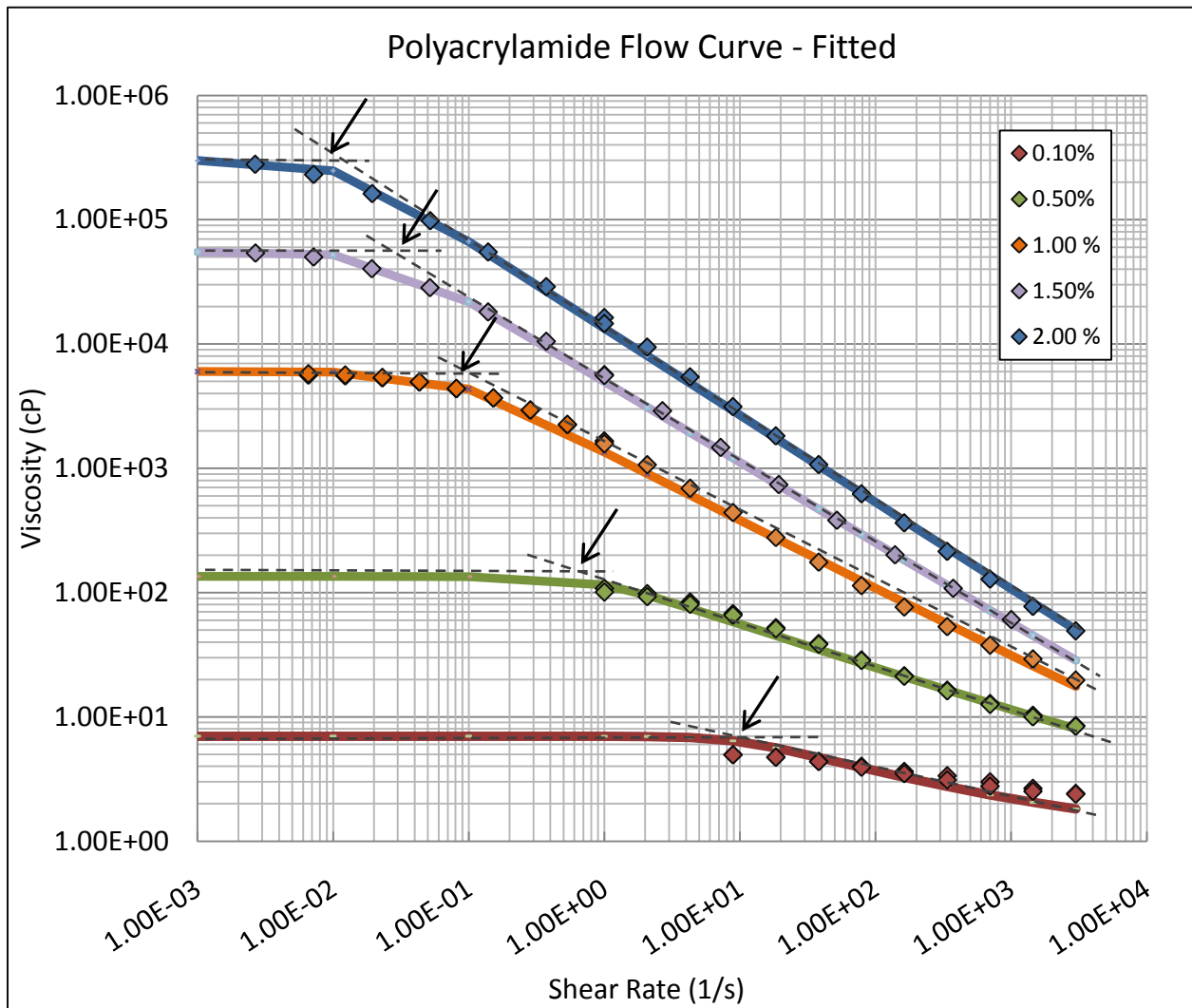
Figure 28: Fitted Carreau power law model for five solutions used in injection experiments

Table 3: Fitted rheological parameters for polyacrylamide using the Carreau power-law model

Fitted Data				
Concentration	μ0 (cP)	μ∞(cP)	n	λ (s)
0.1%	7	1	0.65	0.1
0.5%	135	1	0.64	1.2
1%	6000	1	0.45	15
1.5%	55000	1	0.35	40
2%	300000	1	0.3	85

An effective viscosity within the Hele-Shaw cell can now be estimated based on the fitted Carreau viscosity model and the representative cell shear rate. In order to determine an effective shear rate at the vicinity of the injection point, the parameters of injection rate (Q), inlet radius (r_w), average grain diameter (d_p), and gap thickness (b) were used as inputs.

$$\dot{\gamma} = \frac{Q}{2\pi r_w d_p b} \qquad \text{(eqn 34)}$$
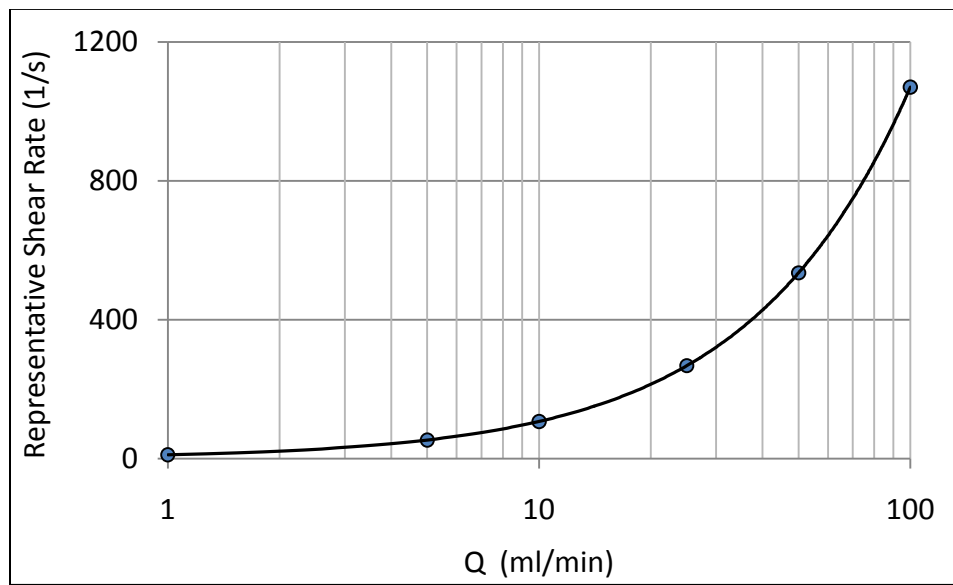
Figure 29: Calculated cell shear rate as a function on injection rate

Based on the calculated injection shear rate within the Hele-Shaw cell, an effective viscosity (η_{eff}) can be defined for each polymer solution for a given injection rate. Although it is not possible to calculate the exact viscosity at any point within the cell due to local changes, an apparent shear rate is calcualted for each test. A graph of calculated effective viscosity vs the effective velocity based on the flow rate can be seen in Figure 30. The effective viscosities corresponding to the apparent shear rate vary several orders of magnitude and can range from

about 4300 cP for 2.00% polyacrylamide at a flow rate of 1.0 ml/min, to 2.0 cP for the low-concentration 0.10% solution at 100.0 ml/min.
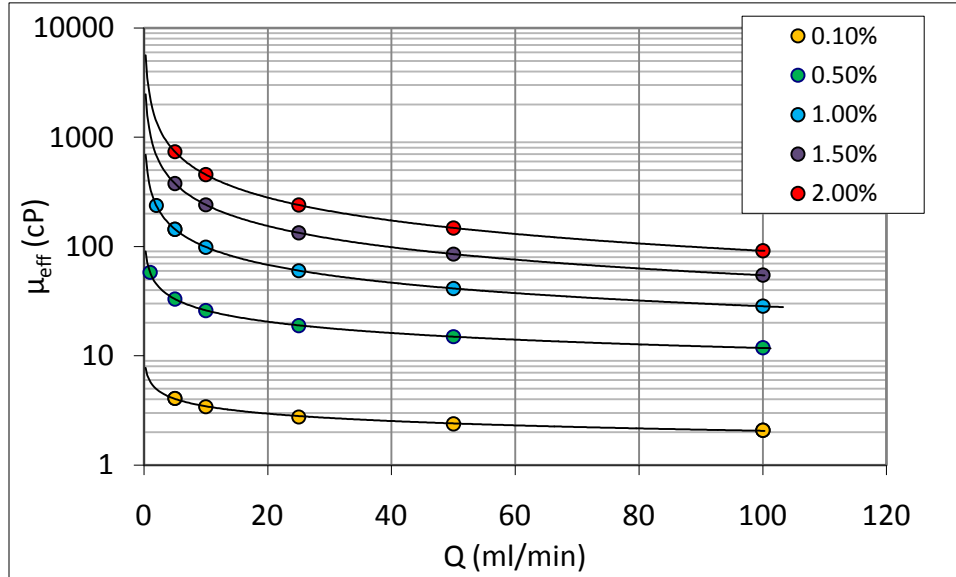
Figure 30: Calculated solution viscosity within the Hele-Shaw cell as a function of solution concentration and injection rate

The fitted polyacrylamide flow curves in Figure 28 also reveal critical shear rates for each solution; i.e. the shear rate above which the fluid behavior becomes shear-thinning. These values are marked by the arrows in the figure above and are located at the intersection of lines fitting the low shear and shear-thinning portions of the curves. An inverse of the critical shear rate for each fluid can be used as an approximate relaxation time (λ). As expected, due to viscoelastic effects, the relaxation time will increase greatly as polymer concentration increases. The figure below shows the relationship between fluid relaxation time and zero-shear viscosity for each of the five solutions used in our injection series.
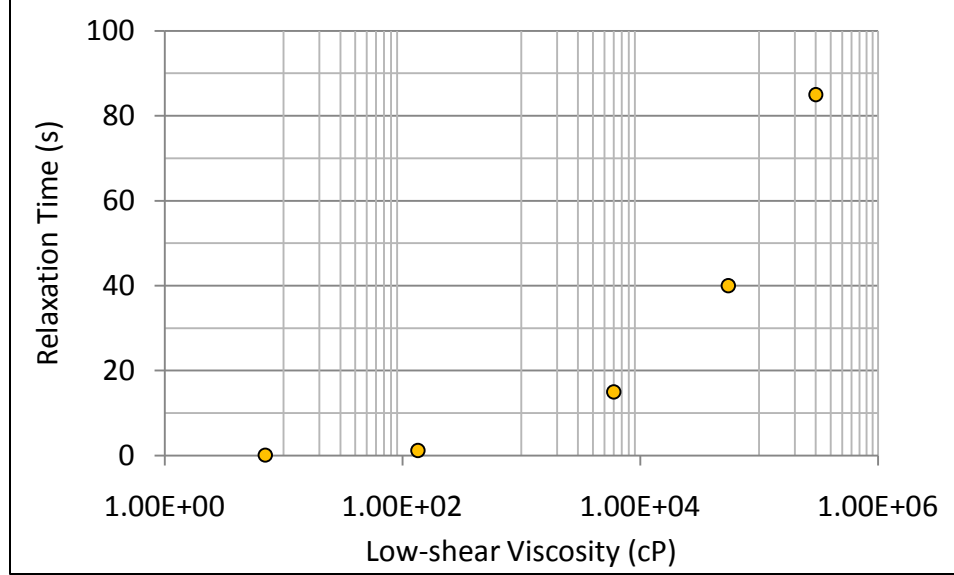
Figure 31: Approximate relaxation time for each polymer concentration based on the critical shear for viscosity drop

4.2 Dimensionless Analysis

In order to quantify the varying experimental parameters, a dimensionless number (χ) has been calculated based on the fluid and granular media properties, as well as test conditions. The number takes into account flow rate (Q), effective fluid viscosity (μ), particle size (d_p), inlet size (r_w), gap thickness (b), small strain elastic modulus of the sand (E), and permeability (k).

$$\chi = \frac{Q\mu d_p}{2\pi r_w b E k} \tag{35}$$

This dimensionless number contains components of several characteristic time scales for this experiment. It is a combination of the injection time $\frac{\left(\frac{Q}{2\pi rb}\right)}{d_p}$ and the diffusion time $\frac{\mu d_p^2}{Ek}$. The latter can also be interpreted as a measurement of the fluid/granular mixture relaxation time $\frac{\mu_{gr}}{E}$.

For our series of injection experiments, the cell and sand properties remain constant and are listed in Table 4. However the flow rate and fluid viscosity are varied for each test.

Table 4: Constant experiment parameters

| Gap Thickness (mm)	Young's Modulus (MPa)	Sand Permeability (millidarcies)	Particle Size (mm)	Inlet Radius (cm)
1.57	66.2	739	0.11	.051

The range in the dimensionless numbers calculated for each test can be seen below in Figure 32. The values are plotted on a log scale and vary by about three orders of magnitude. For our injection series, the dimensionless number ranges from a maximum of $1.91*10^{-3}$ for a flow rate and concentration of 100 mL/min and 2.00%, to a minimum of $4.24*10^{-6}$ for a flow rate and concentration of 5 mL/min and 0.10%. As stated previously, the only parameters varied from test to test are the flow rate and solution viscosity (as a function of shear rate and polymer concentration). Therefore, only the value in the numerator in equation 35 will be variable.
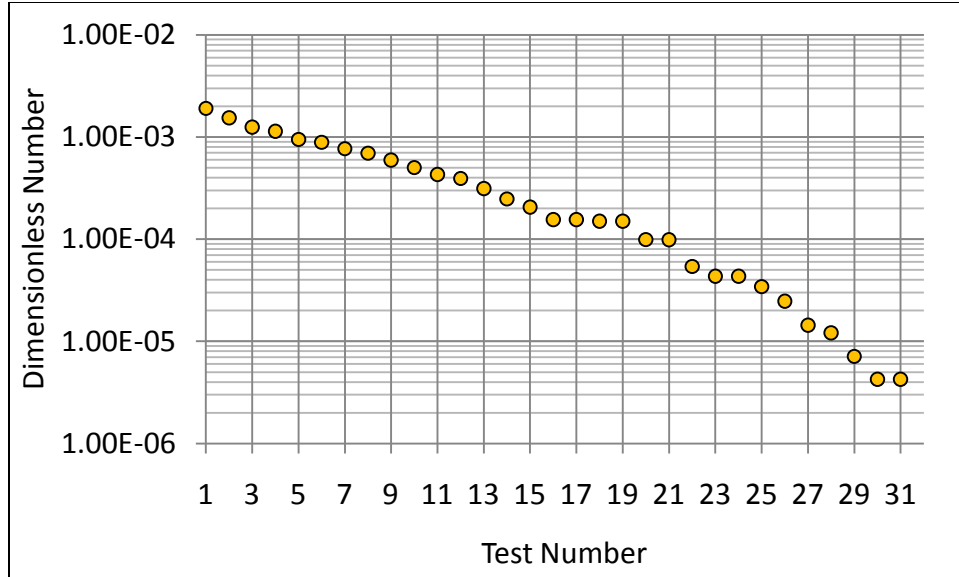
**Figure 32:** Dimensionless number calculated for each polymer injection

In order to determine the types of forces prevalent within the Hele-Shaw cell two dimensionless numbers can be calculated; i.e. the capillary number and the Reynolds number. *Ca* is a ratio between viscous to capillary forces, while *Re* is a ratio between inertial and viscous forces.

A capillary number can be calculated for our injection experiments using $Ca = \frac{\mu_0 V d^2}{\gamma_s \kappa}$, and as expected there is a systematic increase in *Ca* as the polymer concentration increases from 0.10% to 2.00% and flow rate increases from 5 ml/min to 100 ml/min; see Figure 33. For each injection, the effective viscosity of the solution and velocity are calculated at the inlet. The particle diameter, surface tension, and permeability all remain constant at 0.11 mm, 0.06915 N/m, and 748.7 mD, respectively.
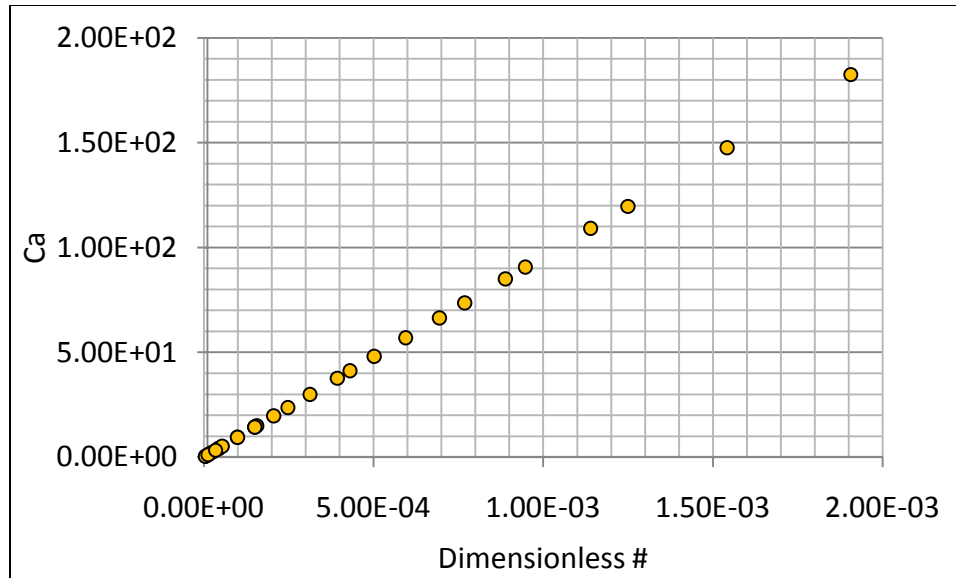
Figure 33: Capillary number calculated for each injection test

A majority of the tests show a capillary number much greater than the limiting value of 1.00. Only the tests at a concentration of 0.10% and flow rates of 5.0 mL/min and 10.0 mL/min will experience a noticeable amount of capillary forces with $Ca < 1.0$. As can be seen from the infiltration patterns for these two low-Ca tests (Figure 34), the profiles of saturation show evidence of capillary flow.
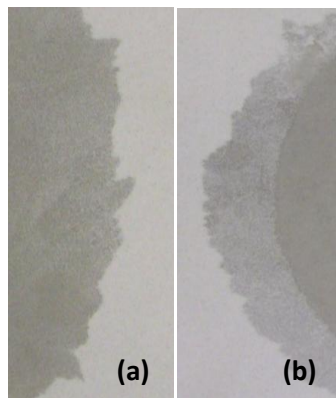
Figure 34: Infiltration boundary dominated by capillary flow for (a) C=0.10%, Q=5.0 mL/min; (b) C=0.10%, Q=10.0 mL/min

Similarly, a Reynolds number is calculated for each injection test using $Re = \frac{\rho V d}{\mu_{ref}}$.

Once again, the only varying parameters are the velocity (as a function of flow rate) and the

effective viscosity. The *Re* values are plotted in Figure 35. Each calculated number is below the

critical values of 2500 for the transition from viscous to inertial dominated forces. As expected

at the highest possible flow rate and lowest viscosity, the maximum Reynolds number of 53.9

occurs at a solution concentration of 0.10% and flow rate of 100 mL/min. Therefore, it can be

concluded that each of our injection tests is governed by the viscous effect and not significantly

affected by inertial forces or capillary forces.
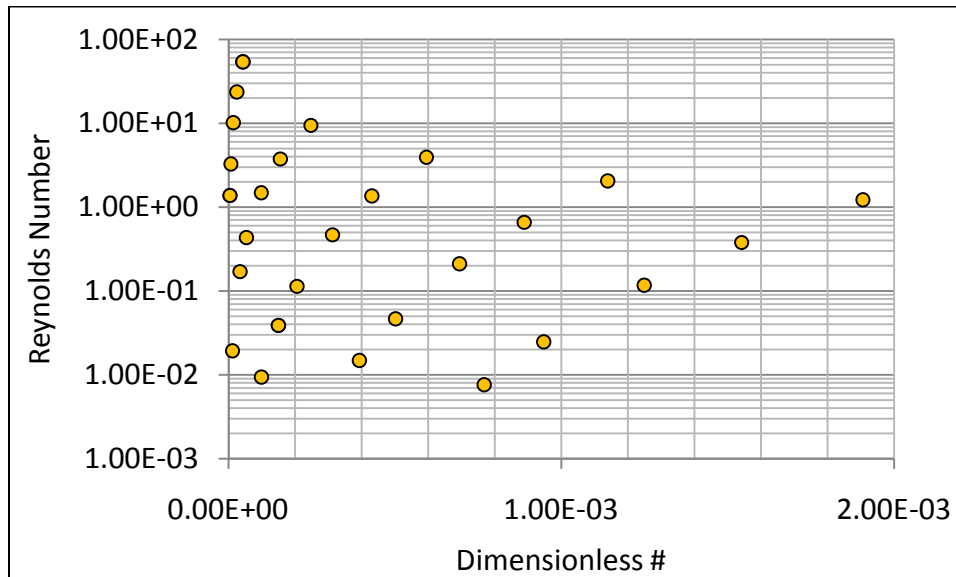
Figure 35: Reynolds number calculated for each injection test

4.3 Image Analysis Results

One advantage of the use of a Hele-Shaw cell is the ability to visualize the flow/failure

process. Figure 36 below shows the final images from our injection series. *B* is equal to the gap

thickness (0.062" for each test) and Q is the volumetric flow rate. The solution concentration remains constant for each row, while the injection rate (or velocity) is constant for each column.
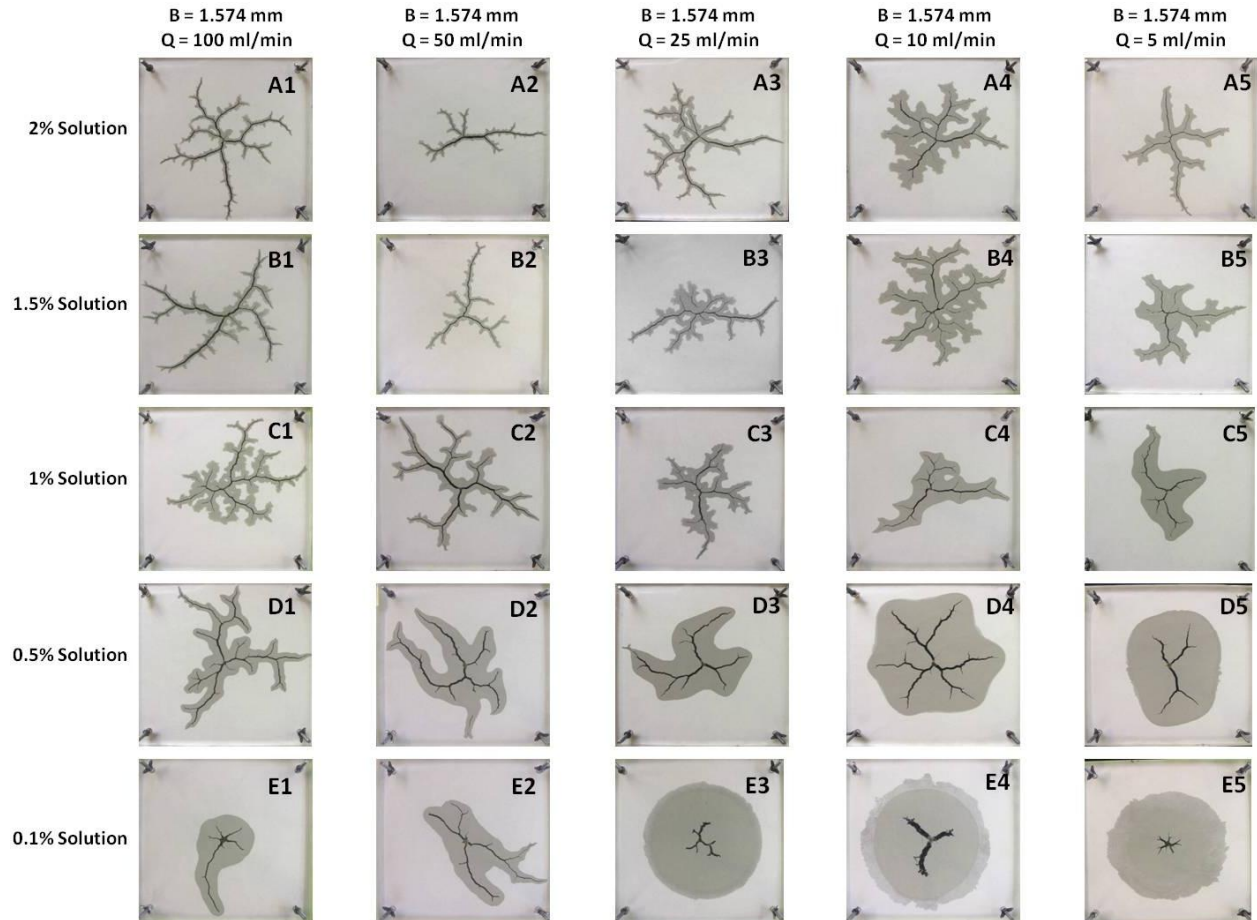
Figure 36: Fracture and leakoff patterns for our series of Hele-Shaw injections

The patterns created during the injection process can be quantified using several image analysis techniques. Because we take a continuous progression of photographs throughout each injection we are able to process a series of these pictures and extract numerical data from them. For each test, a sequence of photos was chosen and processed through a Matlab script created to identify the boundaries of the fractured zone and leakoff zone.

4.3.1 Fracture and Leakoff Growth

The Matlab image processing technique also allows for analysis of the growth patterns of the leakoff and fracture areas. By overlaying the series of images taken at successive times during the injection process, a time-lapse figure is created in which the patterns of the fracture and leakoff growth can clearly be identified. As stated in the observations of previous research studies, the fractures created by non-Newtonian fluid injection are often much thinner and localized due to shear thinning and viscoelastic effects. A preferential flow direction is followed because of a drop in viscosity at the tip of fractures due to high shear rate (Fast, 2001). Similar fracture patterns were witnessed in our injection tests. We observed that throughout the injection process a majority of the growth taking place occurred at the fracture tip, with a narrower, sharper finger than those observed with Newtonian injections (Huang et al 2011). There was also very little splitting at the fracture tip when compared to Newtonian fluid injection; most of the branching took place behind the advancing tip. A set of four injection image sequences at various flow rates and polymer concentrations is presented below in Figure 37 - Figure 40; the narrow fracture growth and transition from radial to localized leakoff patterns can be clearly identified. In order to explore the leakoff and fracture propagation process for a wide range of tests, the dimensionless number χ increases from 3.00×10^{-6}, 4.15×10^{-5}, 3.94×10^{-4}, to 2.01×10^{-3}, respectively.

61

(a)   **(b)**
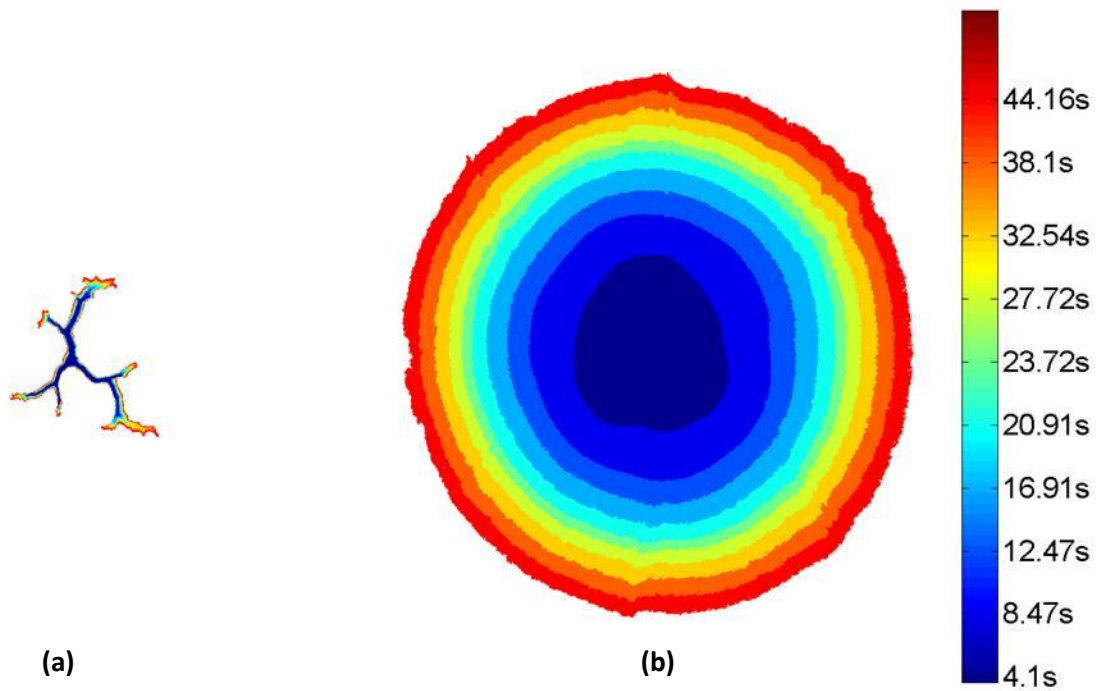
Figure 37: Image sequence (C = 0.10%, Q = 25 ml/min), Test E3 (a: fracture, b: leakoff)

(a)   **(b)**
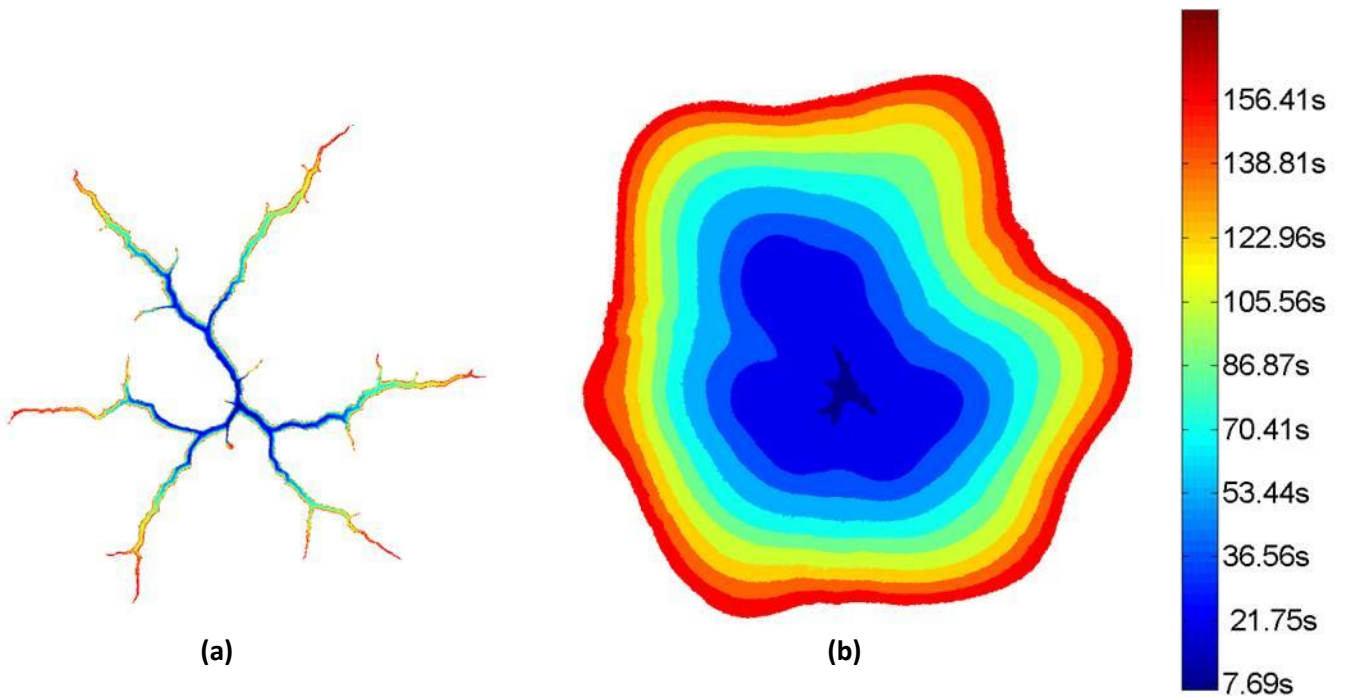
Figure 38: Image sequence (C = 0.50%, Q = 10 ml/min), Test D4 (a: fracture, b: leakoff)
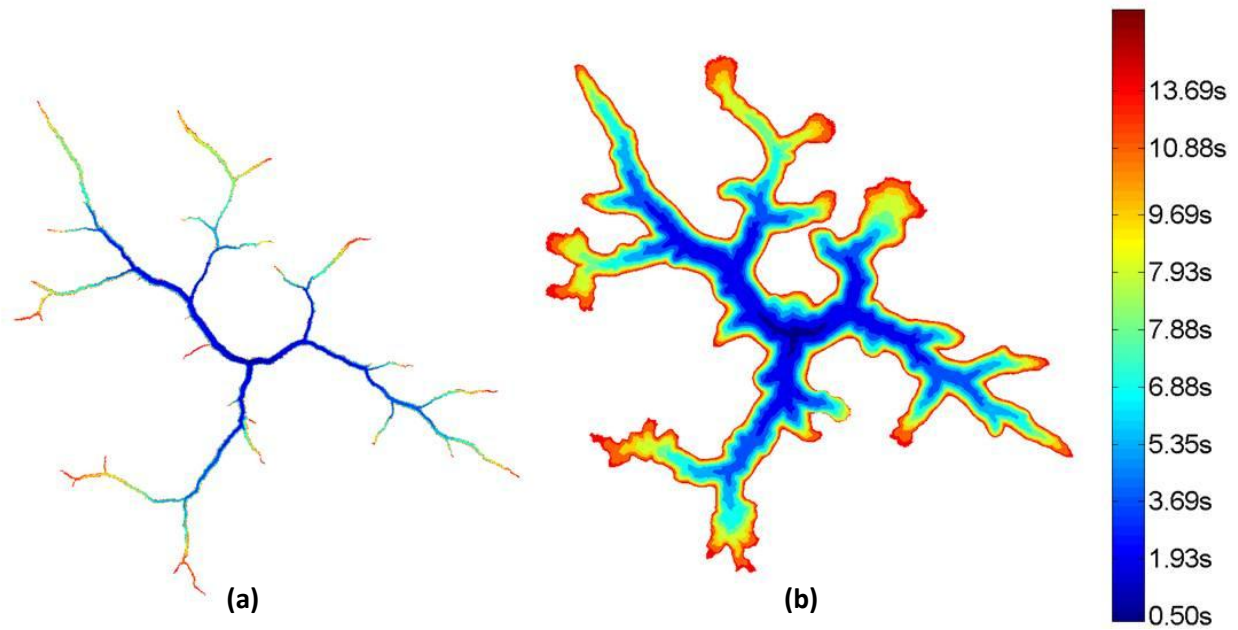
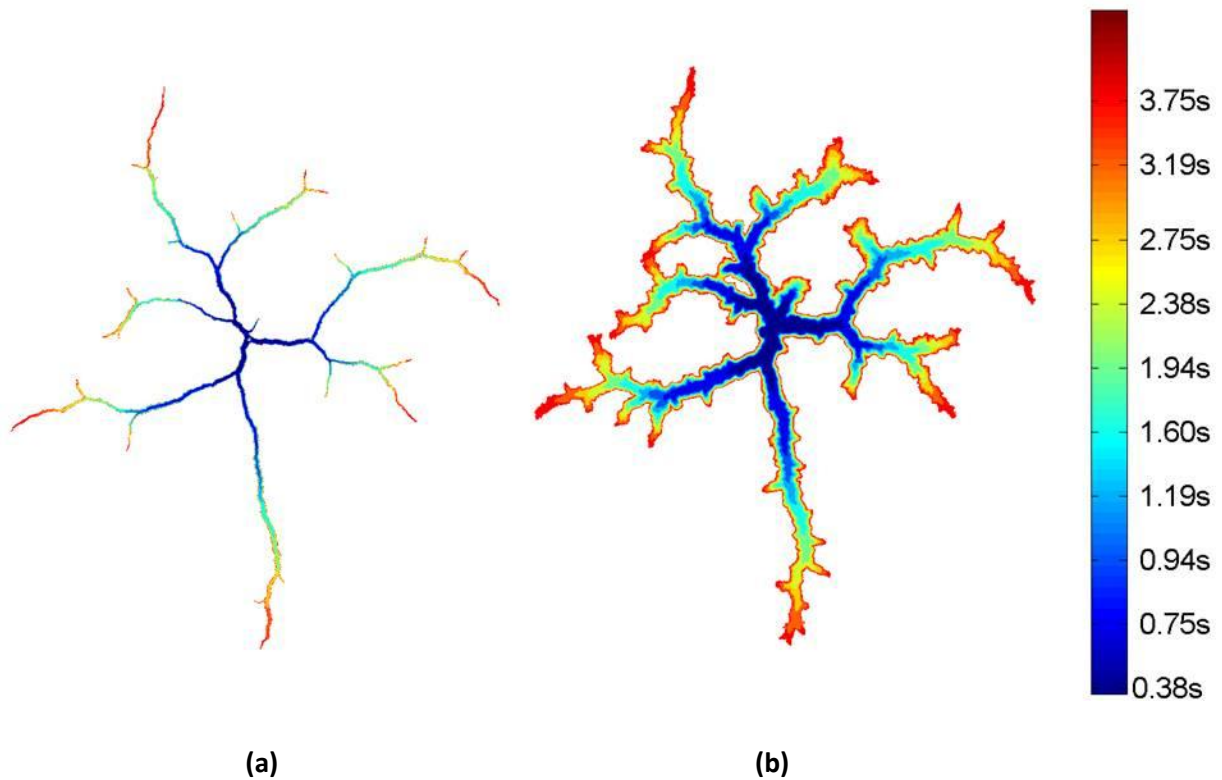**Figure 39:** Image sequence (C = 1.00%, Q = 50 ml/min), Test C2 (a: fracture, b: leakoff)

Figure 40: Image sequence (C = 2.00%, Q = 100 ml/min), Test A1 (a: fracture, b: leakoff)

4.3.2 Ratio of Fracture Area / Leakoff Area

The first quantifiable value we look at is the ratio between the area of fracture (S_F) to the area of leakoff (S_L); i.e. the black area and dark gray area in each image. These values are calculated by counting the number of pixels in the fracture and leakoff regions for a series of 10 successive photographs. For example, for the given series of images taken during Test E3 (C = 0.10%, Q = 25.0 mL/min) the calculated S_F/S_L value at each time step is plotted in
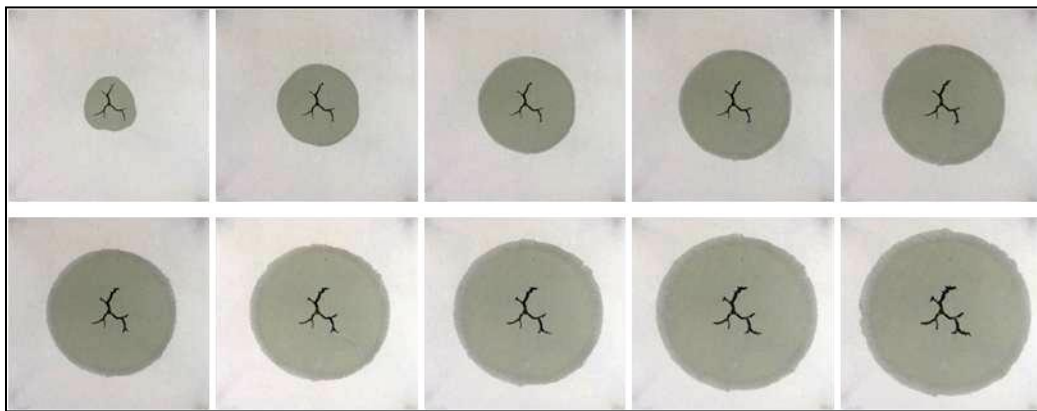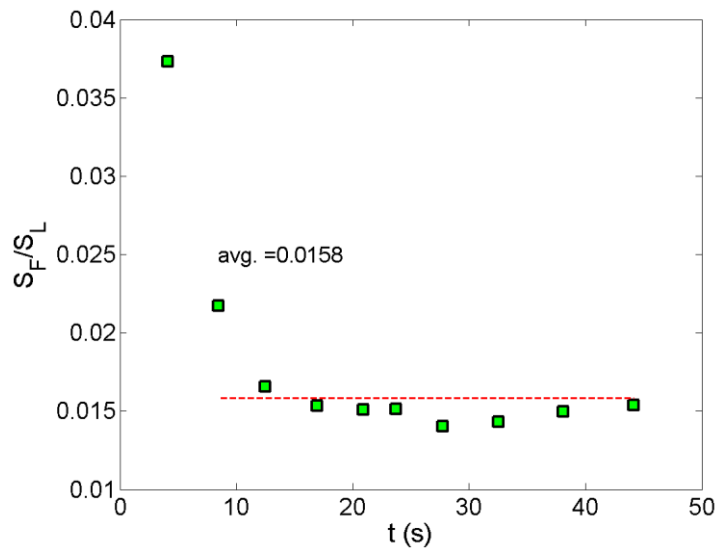
Figure 41: (a) image series and (b) plotted values of S_F/S_L for each image. The average value is reported. Test E3 (C = 0.10%, Q = 25.0 mL/min)

The average ratio from these 10 pictures is found and reported in Figure 42 below as a single S_F/S_L value for each test. As expected from a visual inspection of the injection patterns in Figure 36, the tests at low dimensionless number which, resulted in large circular l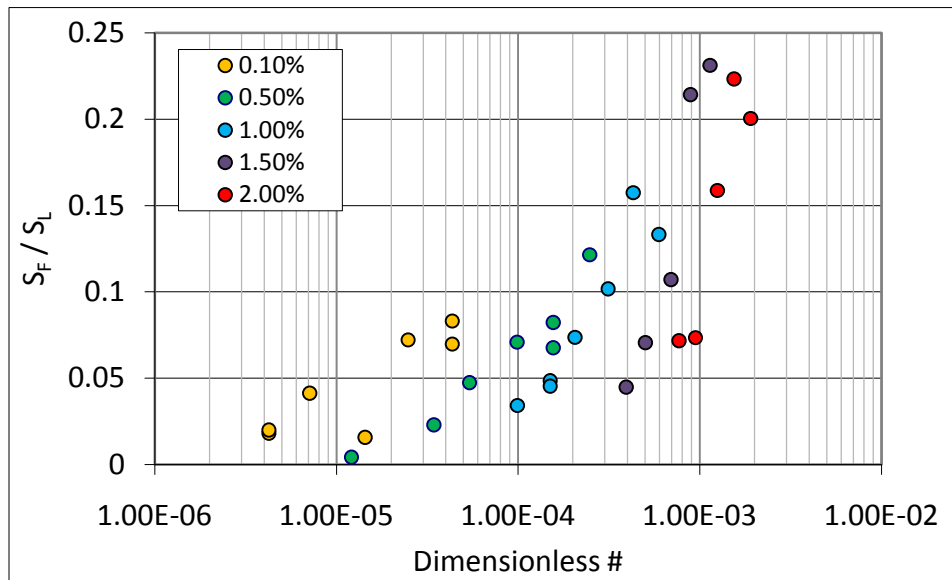eakoff patterns and less extensive fractures, have considerably lower S_F/S_L values. As flowrate and polymer concentration are increased, the branching, localized leakoff patterns result in higher values of S_F/S_L. Figure 42 is color coordinated based on solution concentration.

Figure 42: S_F/S_L data for each injection test performed as a function of calculated dimensionless number. The data is broken down based on solution concentration.

4.3.3 Fractal Analysis

A useful technique to quantify the injection patterns is the use of fractal dimension. A fractal is defined as an object that retains a characteristic shape at a variety of magnifications or scales. For each injection series we used the shape of the final leakoff and fracture pattern to calculate the fractal dimension of the image in Matlab. Essentially, it is expected that if the pattern is circular the fractal dimension will approach the limit of 2. However, if the leakoff is

branching and localized, the fractal dimension will decrease. Graphs of the calculated fractal dimension for the leakoff and fracture patterns are presented below in Figure 43 and Figure 44.
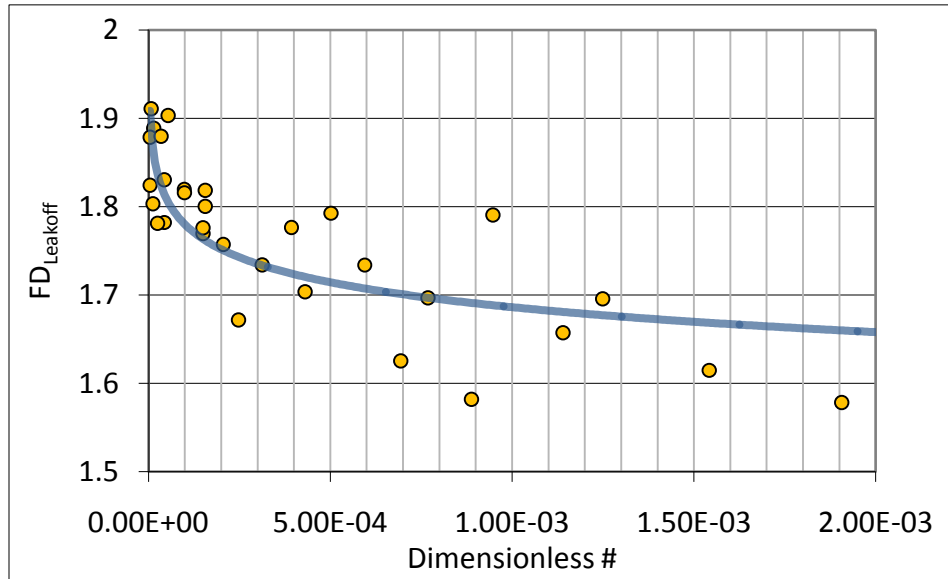
Figure 43: Fractal dimension of the leakoff pattern for each injection
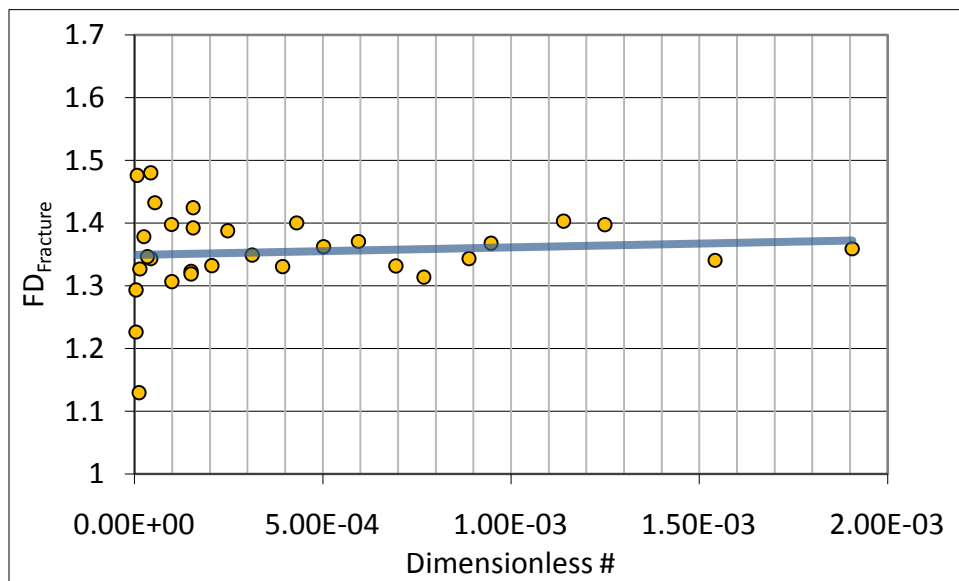
Figure 44: Fractal dimension of the fracture pattern for each injection

The calculated values for the leakoff (Figure 43) follow very nicely the predicted trend; as leakoff patterns transition from circular (low χ) to branching (high χ) the fractal dimension decreases logarithmically from a limiting value of about 1.9 to a constant of around 1.65, the proposed diffusion limited aggregation value (Daccord 1986). From visual inspection there is obviously a transition from a circular, rounded pattern to a more localized, branching formation. The fractal dimension calculation allows for a quantitative description of the shape. At first glance the geometric difference between the series of leakoff boundaries may not be apparent; especially at high dimensionless numbers where the leakoff is small. However, the fractal dimension analysis is able to pick up on the small variations in pattern shape. A zoomed in comparison between two leakoff fronts is shown in Figure 45 for two injection tests highlights the differences in pattern. As expected, the fractal dimension drops from 1.704 to 1.578 due to the more rounded, uniform boundary in (a).
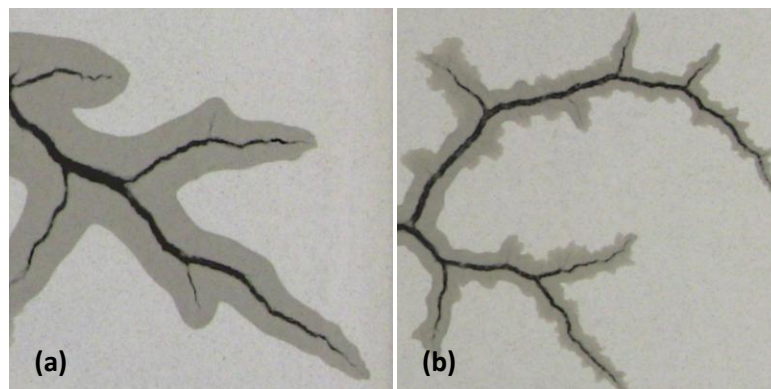
Figure 45: Magnified view of leakoff boundary to illustrate transition from rounded, uniform pattern. (a) Test C2, C=1.00%, Q=50 mL/min and (b) Test A1, C=2.00%, Q=100 mL/min fractal dimension drops from 1.704 to 1.578

The values of the fractal dimensions from the fracture patterns (Figure 44) follow a more peculiar trend and seem to remain constant at a more predictable value of about 1.35 as the

dimensionless number increases. There is some data scatter at lower χ values due to variation in fracture shape, however at high and intermediate χ the fractal dimension remains fairly constant. This can be explained by the fact that, unlike the leakoff boundaries, the fracture patterns do not vary significantly as viscosity and flow rate are modified. Although the Matlab image analysis code is designed to differentiate and identify the fracture and leakoff boundaries, some errors in image analysis can arise due to the inability to pick up "micro-fracture". These features appear in many of the high concentration injections and are formed as small channels between the sand formation and Hele-Shaw plate. Technically some of these could be considered fractures and would affect the S_F/S_L and fractal dimension calculation. A zoomed in view of some typically observed micro-fractures is shown in Figure 46

Figure 46: Micro-fractures forming between the sand layer and Hele-Shaw cell. Test A4

A combination of both the fracture and leakoff shape can be quantified based on the ratio of their two fractal dimensions. As leakoff is minimized and localized to the fracture pattern, the

two fractal dimensions will approach a similar value. The ratio of fracture fractal dimension to leakoff fractal dimension will initially be low for the radial leakoff regime and tend to a value close to 1.0 as the leakoff becomes smaller and more localized to the fracture pattern. This relationship is shown graphically in Figure 47.
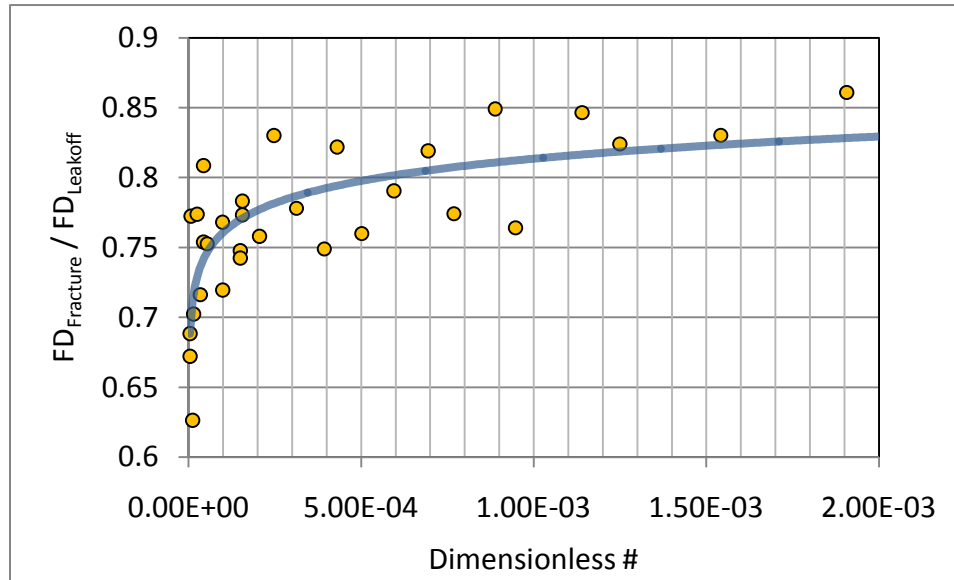
Figure 47: Ratio of fractal dimension terms

4.3.4 Defining Flow/Failure Regime Boundaries

The ratio between the area ratio (S_F/S_L) and the fractal dimension of the leakoff area (FD) can be calculated. The calculated ((S_F/S_L) / FD) values are plotted as a function of dimensionless number in Figure 48. The shape of the data plot is similar to Figure 42 for simply the (S_F/S_L) data, however the new data set incorporates leakoff fractal dimension values.
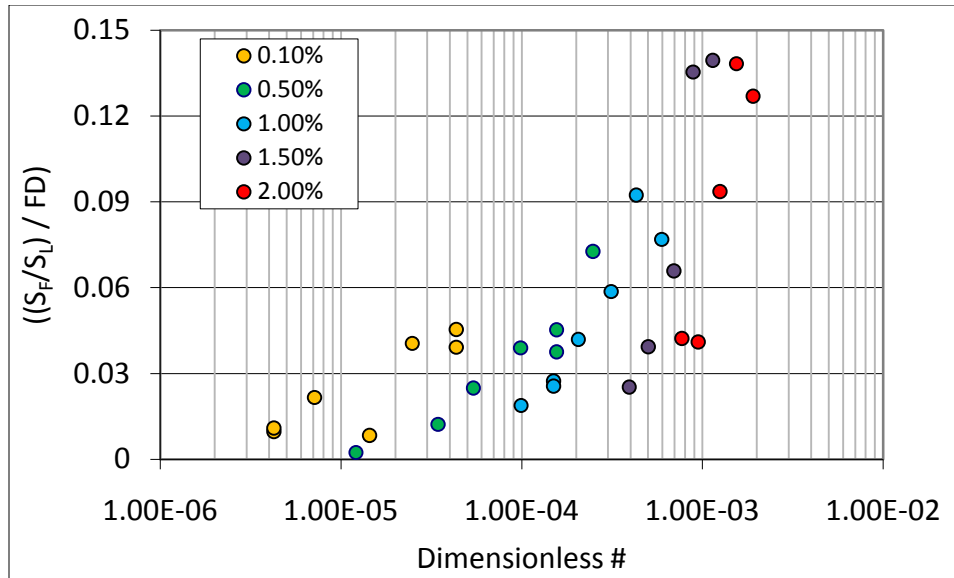
Figure 48: $((S_F/S_L) / FD)$ as a function of dimensionless number.

In accordance with similar work (Huang 2011), a failure/flow regime map for polyacrylamide solutions is proposed. A visual inspection of the failure/infiltration regime map shown in Figure 49 identifies a distinct transition from simple radial infiltration to tortuous, branched viscoelastic fracture. The low viscosity, low flowrate injections results in small fractures and a radial leakoff area. As injection rate and solution concentration is increased the leakoff patterns become more localized and longer fractures are propagated. At the highest flow and concentrations the fractures and leakoff follow localized, branching paths. Three regions are identified and color-coordinated in Figure 49. The injections highlighted in red show the largest leakoff and their infiltration is the most circular (as calculated by the fractal dimension); this is defined as the infiltration dominated regime. The green injections are identified as transitional. The tests highlighted in blue show localized, low leakoff and are in the viscous flow regime more comparable to a fracturing process.
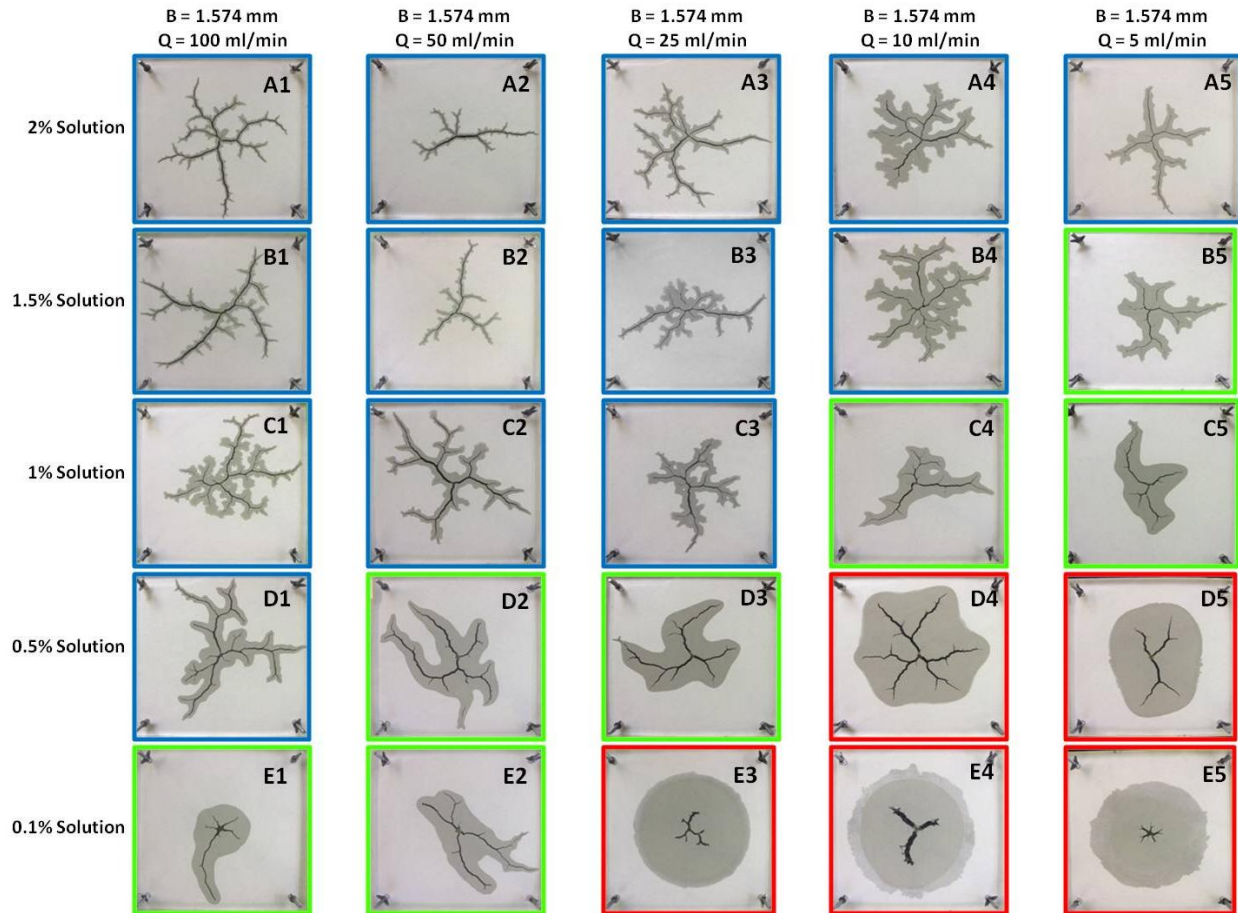
Figure 49: Regime map with separate regions defined based on the values of $((S_F/S_L) / FD)$

4.4   Pressure Data Results

The pressure required to inject each given fluid was recorded using a 400 Hz wireless pressure sensor. The pressure response of each test followed similar patterns; usually exhibiting an initial period of significant pressure increase, followed by a sharp decline and a period of stabilization. This pressure response is more than likely due to a three-stage process of radial flow, fracture initiation, and fracture propagation. In other words it can be assumed that the fluid invasion process begins with in initial saturation period in the vicinity of the injection point; then

as fluid pressure builds and is resisted by the skeletal forces of the granular matrix a cavity is developed, and is finally propagated due to stress localizations. With a non-uniform particle distribution the fluid will invade the largest pores first leading to hydraulic wedging. The well-defined pressure spike was seen in every experiment, and the drop occurs right at the instance of fracture propagation. The stable, low propagation pressure can be attributed to the preferential flow tendency of the fluid due to fracturing. A sample of the pressure history for an injection can be seen below in Figure 50 with the images of infiltration, early-time fracture development, and late-time fracture propagation identified.
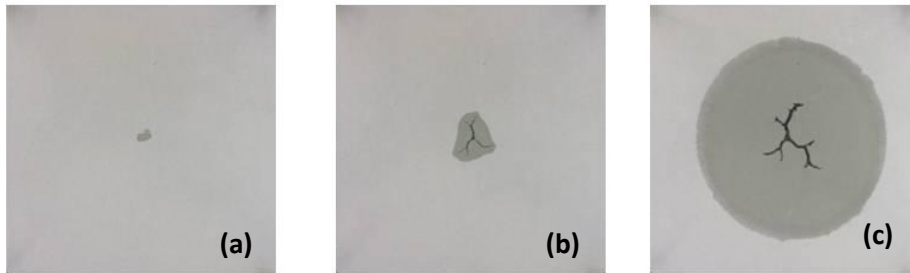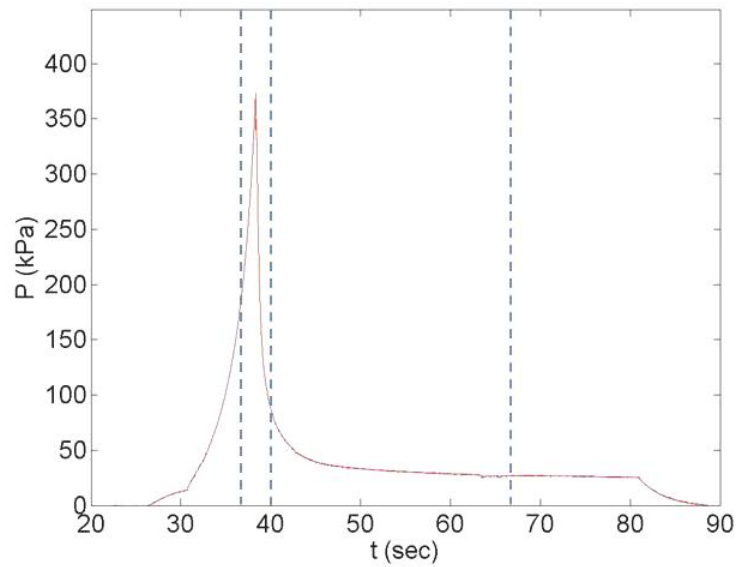
Figure 50: Pressure response history and injection image sequence at various times in during the injection process (a: infiltration, b: fracture development, c: propagation), Test E3

4.5   Discussion

The failure/flow regimes proposed by Huang (2011) can be directly compared to our non-Newtonian results. In Hele-Shaw experiments using glycerin solutions several regimes are defined based on simple radial flow with no fracture initiation, a leakoff dominated, grain displacement dominated, and viscous fingering dominated process. The behavior of the granular media within the Hele-Shaw is comparable to a solid response for an infiltration process and a fluid-like response for the viscous fingering regime (Huang 2011). A failure / flow map for an injection series using Newtonian glycerin solution is presented in Figure 51 below. Through visual inspection the regimes and energy dissipation mechanisms can be identified.
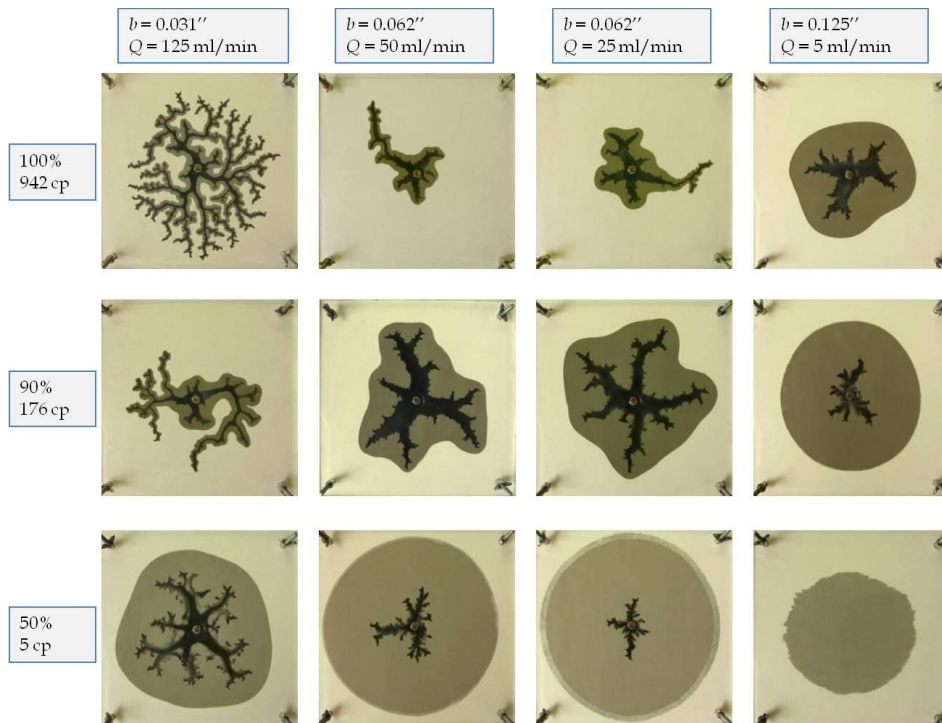
Figure 51: Injection series for Newtonian glycerin solutions with varying viscosity (y-axis) and flow rate (x-axis) (Huang 2011)

The modes of energy dissipation for our non-Newtonian polyacrylamide injection tests include viscous losses for flow in porous media, dissipation via grain displacement, and finally viscous loss due to flow in channels created by multiple, branching fingers. Once again, the flow/failure patterns vary from a radial infiltration process to a viscous fingering / fracture process.

One identifiable difference from a comparison between polyacrylamide and glycerin injections is noticeably thinner fractures for the non-Newtonian test series. This can possibly be explained by shear-thinning viscosity and polymer adsorption. The response of the polymer solution in granular media is predominately governed by the shear thinning response of the fluid. After the initial infiltration phase, the fluid invades the largest pore spaces and fractures begin to propagate. The high velocity and shear rate in the channel causes a viscosity drop in the fluid. As fluid flows within the fracture channel, a preferential flow direction is established. Due to elasticity of the polymer chains, a higher extensional viscosity causes the fluid to prefer parallel flow within the fracture rather than perpendicularly into the pore space. This results in narrow fractures and insignificant leakoff growth.

It has also been noted that it is possible for individual polymer molecules to become adsorbed and entangled within pore spaces, and act to clog potential flow paths (Flew, 1993). This results in not only a decrease in the local permeability but also a reduction in polymer concentration of the invading fluid. Both could lead to divergence of flow from the intact granular skeleton to the preferential fracture path.

A comparison can also be made between the mode of fracture growth for Newtonian glycerin solutions and non-Newtonian polyacrylamide. For the glycerin injections the tip propagation occurred in a series of successive steps. First, an initially sharp fracture tip slows its

movement and becomes blunted and as fluid pressure presumably increases within the fracture, the tip splits and further propagation is initiated. The process sometimes manifested itself as a stick-slip signature in the pressure data. This mechanism can be seen in Figure 52. The growth process for non-Newtonian fractures seems to occur with a sharp fracture tip penetrating the granular media and blunting at the tip reduced.
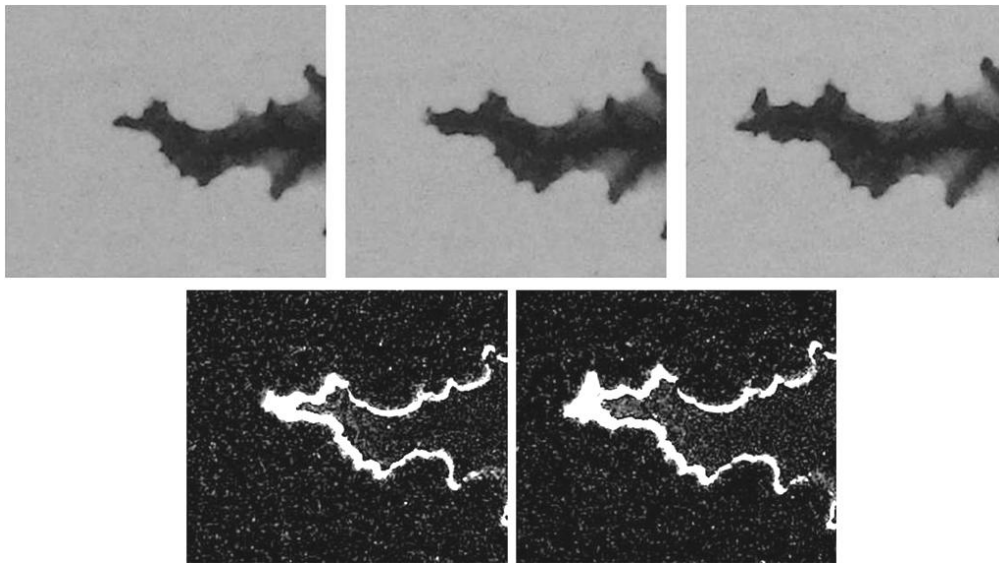
Figure 52: Tip blunting and splitting process witnessed during the injection of Newtonian glycerin solutions. BW image shows the pixel difference between successive pictures, with the white area being areas of growth. (Huang 2010)
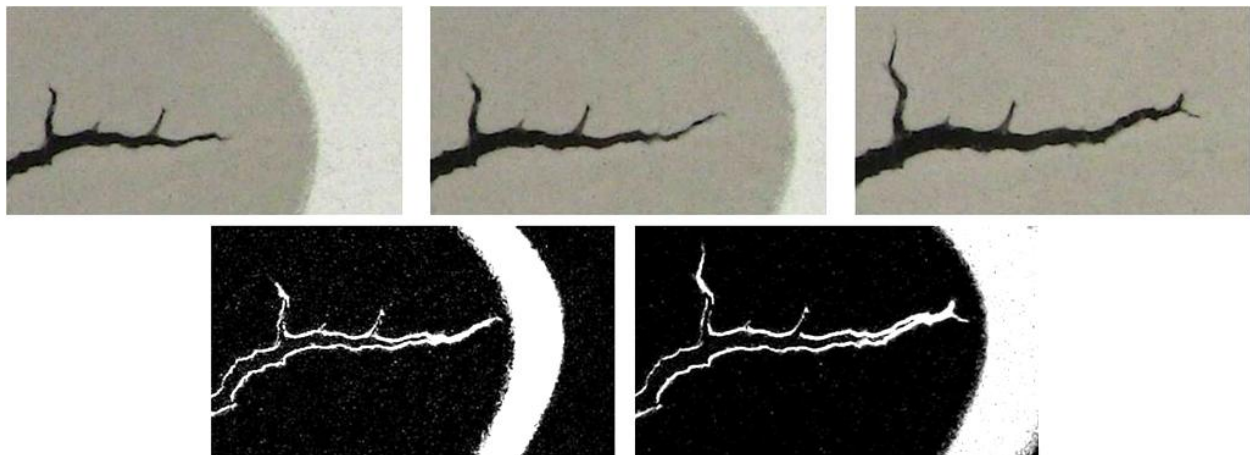
Figure 53: Tip growth process witnessed during the injection of non-Newtonian polyacrylamide solutions. Fractures have much sharper tip and significantly less splitting. BW image shows the pixel difference between successive pictures, with the white area being areas of growth. Test D4

An analysis of the growth patterns for our injection tests reveals some interesting characteristics about the evolution of pattern formation. In many of the tests at low dimensionless number where circular and very rounded leakoff profiles are witnessed, the growth of leakoff and fracture occurs in several distinct stages. A significant fracture is often initiated just prior to the peak in the pressure response, followed by a period of leakoff growth with insignificant fracture propagation. Generally, the fracture will remain a constant size until the leakoff front reaches a critical length, at which point further growth occurs predominantly at the fracture tip. This can be quantified in Matlab using a pixel differential technique to track the areas in which changes have occurred between successive photos. As seen in Figure 54, at the early injection stage a fracture is initially created, however growth occurs only in the leakoff region; it is only later in the time series that further fracture growth is initiated.
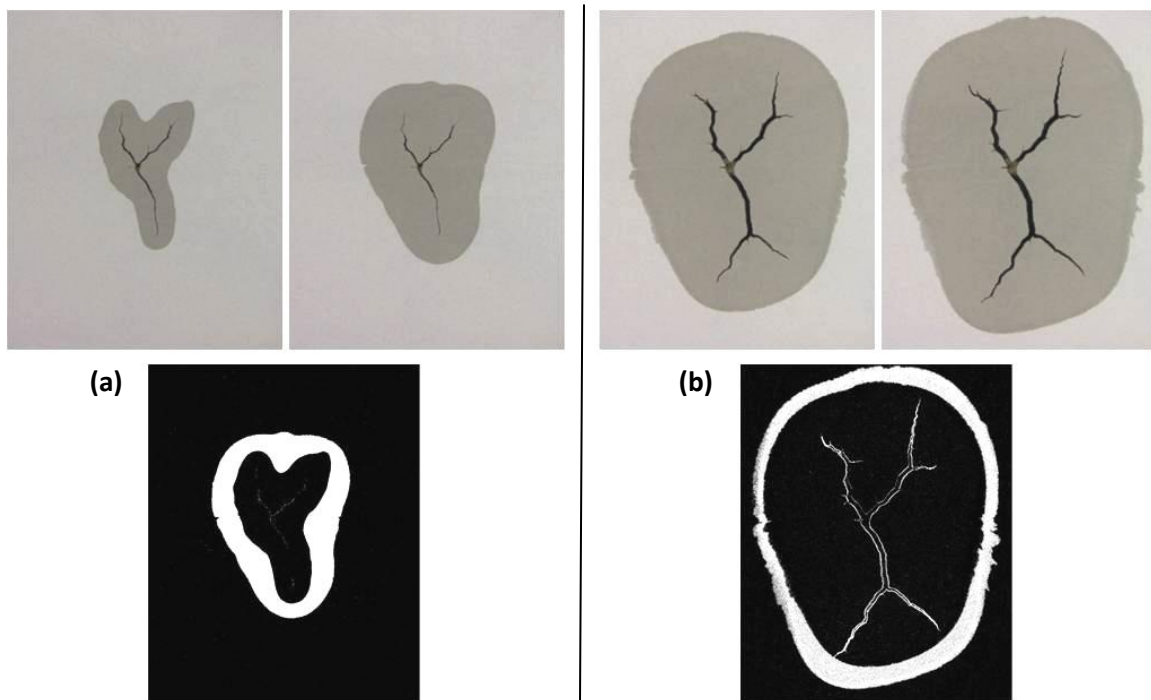
Figure 54: Comparison of growth at two stages in the injection cycle. Initially (a), fracture is formed but growth is limited to the leakoff area. In later stages (b), growth occurs at both leakoff and fracture boundaries. Test D5

The elasticity effects in our injection series can be identified based on polymer concentration; it can be expected that as the concentration on of polymer in solution increases, the elastic effects within the fluid will also increase. This can be quantified based on the relaxation time of each solution; a parameter defined as the inverse of onset shear rate at which shear-thinning effects become prevalent. The relaxation times for each of the five polymer solutions used in our injection tests can be seen in Figure 31 in the preceding chapter. Based on the work of Lemaire (1991) and as seen in our experiment series, the transition from viscous fingering to viscoelastic fracture can be in part attributed to viscoelastic effects of the polyacrylamide solutions. Figure 55 – Figure 58 offer a detailed overview of the fracturing process for several tests at various χ values. Tests E3, D4, C2 and A1 are presented, and an overview of some of their individual flow properties is listed in Table 5.

Table 5: Calculated properties for representative testss

	E3	D4	C2	A1
Concentration (% Wt)	0.10	0.50	1.00	2.00
Flow Rate (mL/min)	25.0	10.0	50.0	100.0
Dimensionless Number	1.44E-05	5.40E-05	4.30E-04	1.91E-03
Reynolds Number	10.20	0.43	1.36	1.23
Capillary Number	1.37	5.17	41.21	182.50
Fractal Dimension (leakoff)	1.89	1.90	1.70	1.58
S_F/S_L	0.016	0.047	0.157	0.200

For each test, a series of ten images taken at even time intervals during the injection are displayed in order to visualize the sequence of fracture and leakoff formation. Tests E3 and D4 take place at low concentration and low injection rates; their leakoff boundaries are large and rounded leading to subsequently high fractal dimensions and low S_F/S_L values. The tests' capillary numbers are relatively low. The capillary effect may not be negligible at late times of the test. The pressure response of these two tests are similar as well; with an initial sharp increase and spike at the moment of fracture initiation, flowed by a low gradual pressure decline during the remaining propagation and infiltration process. As the last portion of the analysis, a series of photos from each test is process using the aforementioned pixel-difference technique to track where changes in the fracture and leakoff propagation are taking place. As mentioned previously in Figure 54, the growth of the fracture and leakoff boundaries seems to occur in two distinct stages for low χ value tests. For Tests E3 and D4 this is visualized through the fractal difference technique; it can be highlighted that there is significant leakoff growth in early time stages but very little fracture growth immediately following initiation.

The higher viscosity and high flow rate injections, Tests C2 and A1, experience much more significant viscous effects as shown in their higher Ca values. The low, tortuous leakoff patterns result in low fractal dimensions and high S_F/S_L values. Because the fluid flow is mainly contained in the fracture, it can be assumed that the prevalent energy dissipation mechanism is due to viscous loss for flow in thin channels. The pressure response for these two tests are similar to E3 and D4 in that there still exists an initial peak and subsequent drop after fracture initiation; however, disturbances are present due to fluxuations during propagation. The image difference analysis for these test show a majority of growth taking place at the fracture and leakoff tip and insignificant expansion perpendicular to the fracture wall.
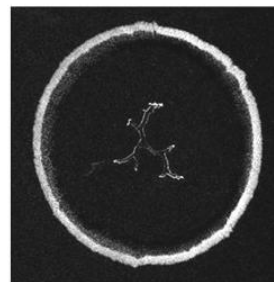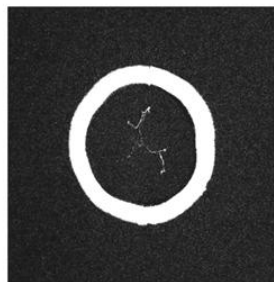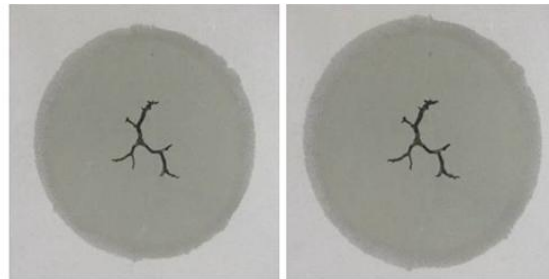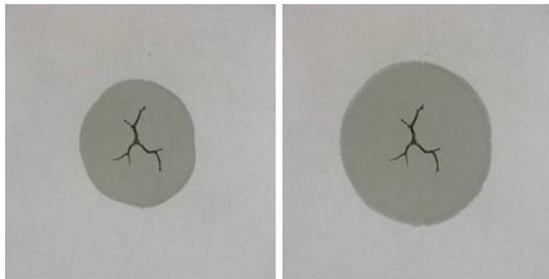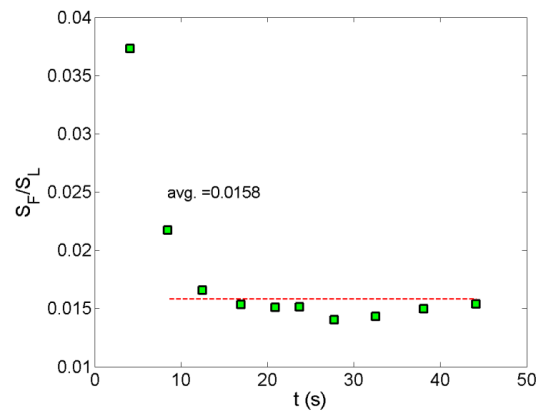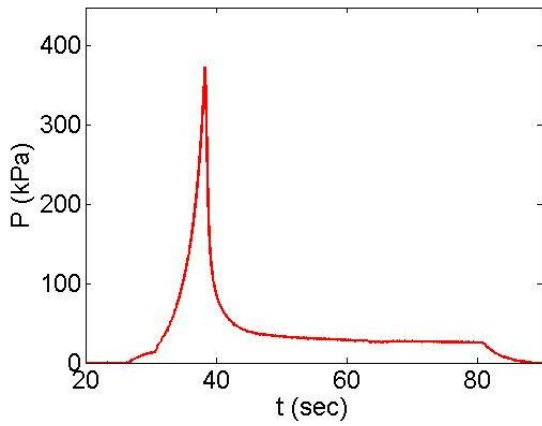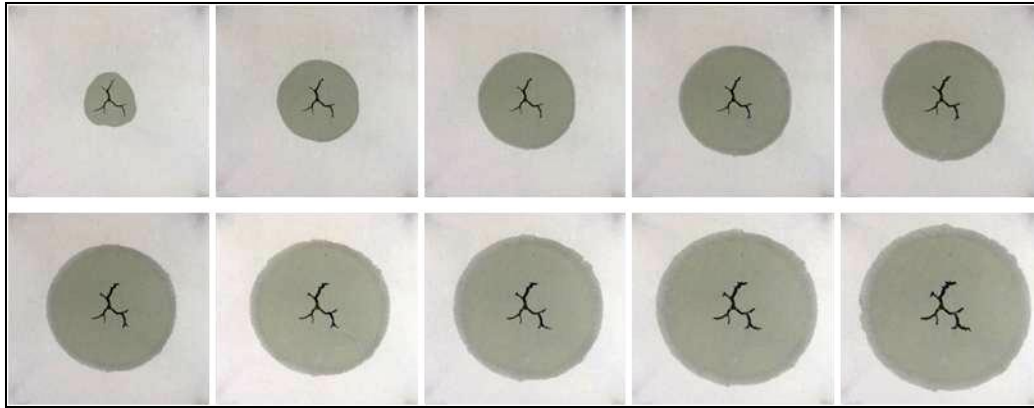
Figure 55: Test E3, (C=0.10%, Q=25mL/min)
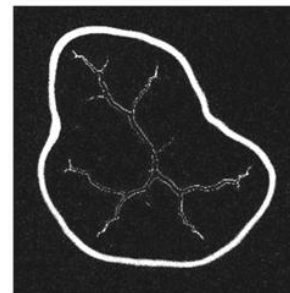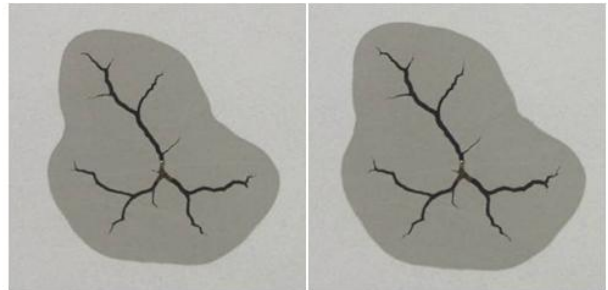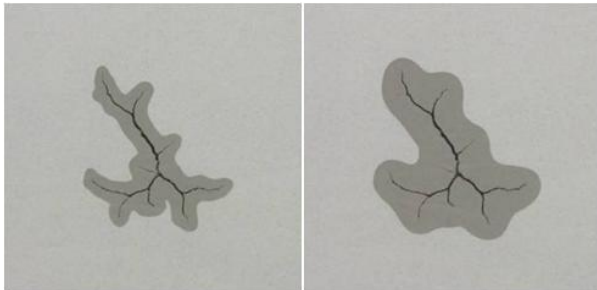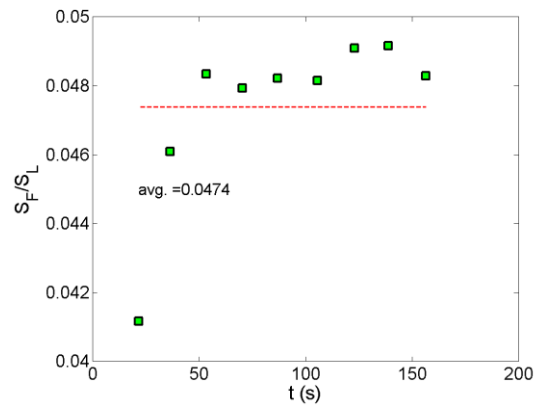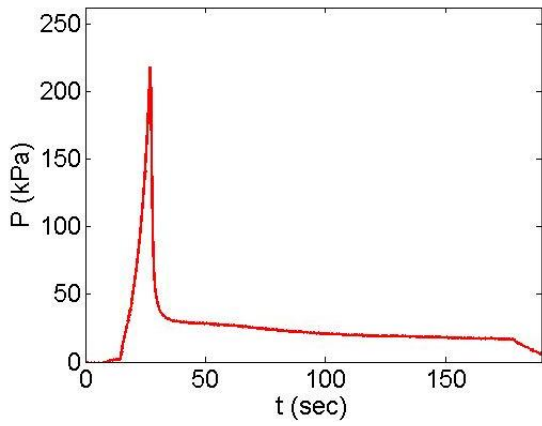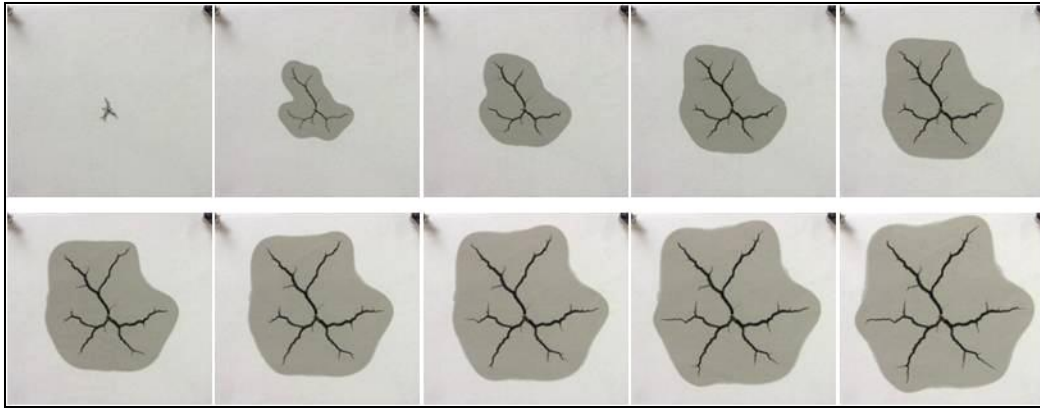
Figure 56: Test D4, (C=0.50%, Q=10mL/min)
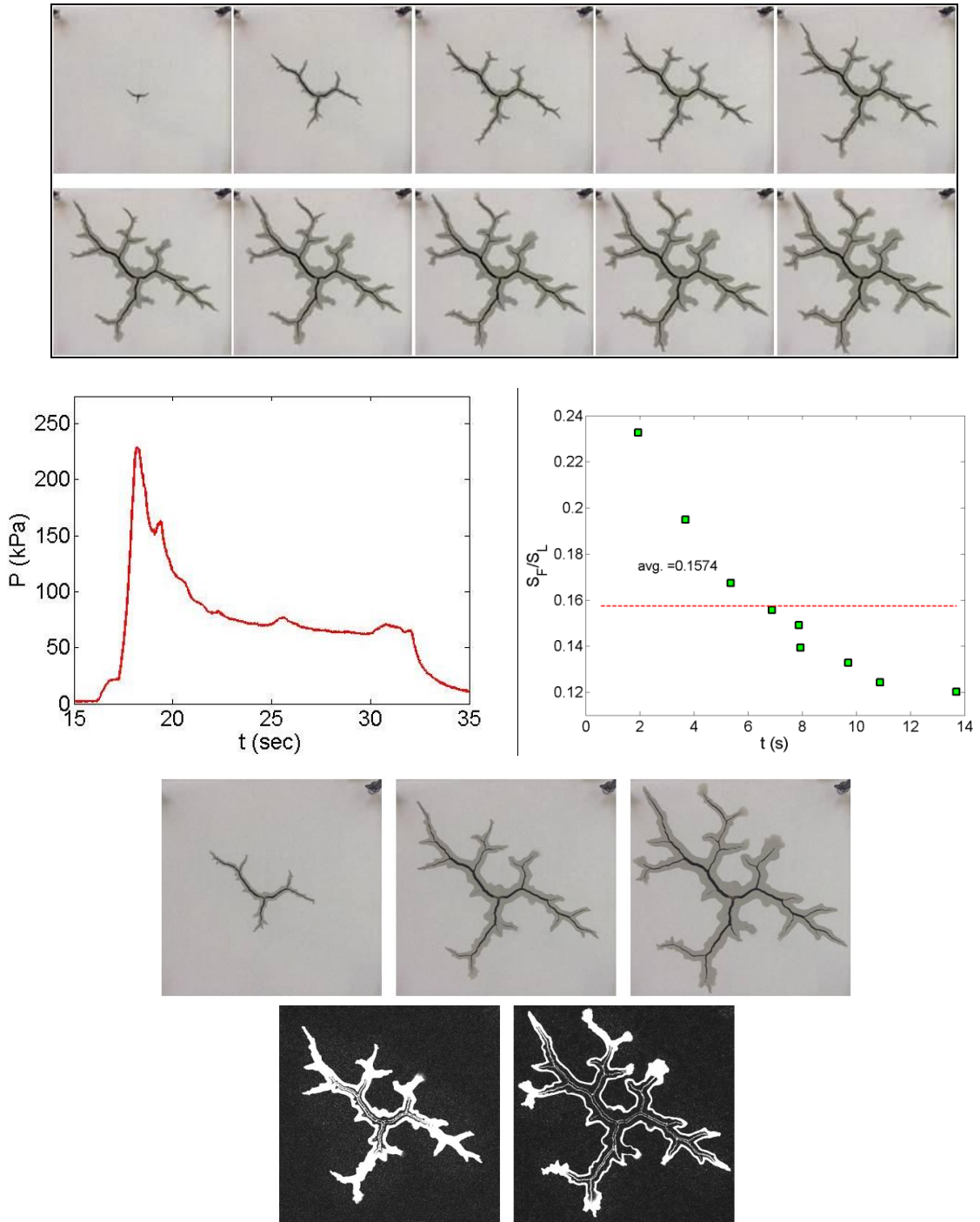
Figure 57: Test C2, (C=1.00% Q=50mL/min)
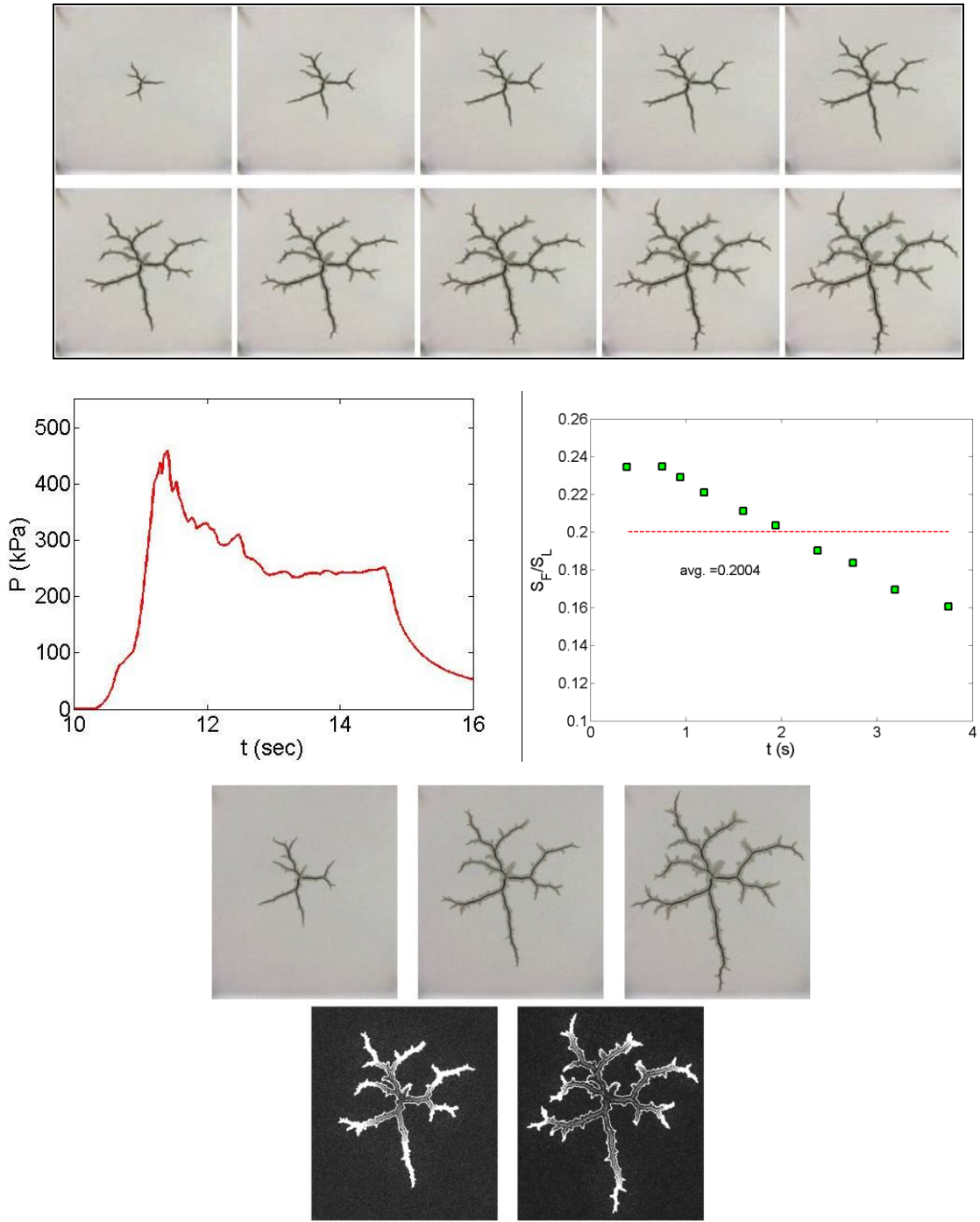
Figure 58: Test A1, (C=2.00%, Q=100mL/min)

CHAPTER 5

CONCLUSIONS AND RECOMMENDATIONS FOR FUTURE WORK

5.1 Conclusions

In this study the coupled fluid / granular media displacement process is investigated experimentally. With a Hele-Shaw cell we focus on the behavior of non-Newtonain polyacrylamide as the invading fluid. This experimental process allows us to visualize and study the failure and flow patterns at various polymer concentrations and flow velocities.

We carried out a series on injections into dry sand with non-Newtonian polymer solutions at a range of concentrations. Our experimental investigation differs from other works of this type because it allow for grain displacement and real-time data collection of the infiltration and fracturing process. Through the use of a pressure sensor we recorded the pressure response at the injection inlet. We found that the pressure history is directly related to the infiltration, fracture development, and fracture propagation process. The image data of the fractures revealed thin, localized fractures with sharp propagation at the tip.

The non-Newtonian rheology of the polyacrylmaide can be described by a Carreau power law model. We are able to calculate an effective viscosity for our fluid as a function of an effective shear rate within the cell. We defined a quantitative dimensionless number for each injection based on our experimental parameters of flow rate (Q), effective fluid viscosity (μ), particle size (d_p), inlet size (r_w), gap thickness (b), small strain elastic modulus of the sand (E), and permeability (k), $\chi = \frac{Q\mu d_p}{2\pi r_w bEk}$ The dimensionless numbers ranges from $4.24*10^{-6}$ to $1.91*10^{-3}$ for tests at low concentration and low flow rate to high concentration and high flow rate.

A capillary number can be calculated for our injection experiments using $Ca = \frac{\mu_0 V d^2}{\gamma_s \kappa}$,.

For each injection, the effective viscosity of the solution and velocity are calculated at the inlet. The particle diameter, surface tension, and permeability all remain constant at 0.11 mm, 0.06915 N/m, and 748.7 mD, respectively. The calculated capillary numbers range from 0.41 to 182.5; the series of injection tests are governed by viscous effects. Similarly, a Reynolds number is calculated for each injection test using $Re = \frac{\rho V d}{\mu_{ref}}$. Once again, the only varying parameters are the velocity (as a function of flow rate) and the effective viscosity. *Re* value range from 0.0076 to 53.8. Once again it can be concluded that each of our injection tests is governed by the viscous effect and not significantly affected by inertial forces or capillary forces.

A number of image analysis techniques were also incorporated to identify the fail/flow mechanisms taking place. We calculate values for the ratio of fracture area to leakoff area (S_F/S_L) and fractal dimension (FD). These values quantitatively allow us to define the fracture and leakoff patterns. At low dimensionless numbers, the large rounded leakoff patterns result in a low S_F/S_L value and a fractal dimension close to 2.0. As leakoff decreases and the boundaries become more localized to the fracture pattern, the dimensionless numbers approach 1.65 and S_F/S_L is increased.

Based on our results, we are able to construct a failure/flow regime map and identify a transition from an infiltration dominated process to a viscous dominated regime, similar to the results of Huang et al (2010). Using a dimensionless analysis and several image processing techniques, the modes of energy dissipation can be identified. For our series of non-Newtonian injection the energy dissipation mechanisms include viscous loss due to an infiltration dominated process, to dissipation via grain displacements, to viscous losses resulting from flow in channels created by fracturing.

5.2   Recommendations for Future Work

The results of our experimental series leave room for further expansion and addition to the work that has already been carried out. The use of a Hele-Shaw cell allows for a number of advantages over other testing techniques due to the ability to collect real-time data on the injection process and development. Although we worked with only one type of non-Newtonian polymer fluid in our series of tests, there is the possibility to incorporate a large number of fluid types. It would be feasible to conduct tests using real fracturing fluids such as cross-linked gels, or study the effects of the addition of filter-cake building materials to the fluid.

Another possible addition to the existing Hele-Shaw setup would be to record real-time pressure responses within the entire area of the cell using a tactile surface pressure transducer. Currently, the only pressure reading is being taken at the inlet of the cell and although this gives an accurate prediction of the pressure near that vicinity, within the rest of the Hele-Shaw cell is unknown. Using a thin, flat tactile pressure that could be placed at the interface between the sand and cell wall would allow for a two-dimensional array of pressure data over the entire face of the cell. Knowing the pressure response along the length of a fracture or at various points within an infiltration area would amount to a much clearer understanding of the flow and energy dissipation process.

The main deficiency to the technique for our series of injections is fact that a controlled confining stress cannot be applied with our Hele-Shaw setup. Due to the given cell geometry and small gap size it is not possible to apply a significant pressure to the outer boundary. An ideal situation would be a modification to the cell which allowed for a control in confining stress similar to a triaxial setup, but that still allowed for visualization of the injection process. With this setup a variety of in-situ stress conditions could be tested.

REFERENCES

1. Ancey, C. and P. Coussot (1999). "Transition from frictional to viscous regime for granular suspensions." Comptes Rendus De L Academie Des Sciences Serie Ii Fascicule B-Mecanique Physique Astronomie 327(5): 515-522.

2. Ancey, C., P. Coussot, et al. (1999). "A theoretical framework for granular suspensions in a steady simple shear flow." Journal of Rheology 43(6): 1673-1699.

3. Bear, J. (1972). Dynamics of fluids in porous media. New York, Dover Publications, Inc.

4. Ben Amar, M. and E. C. Poire (1999). "Pushing a non-Newtonian fluid in a Hele-Shaw cell: From fingers to needles." Physics of Fluids 11(7): 1757-1767.

5. Bestul, A. B. (1956). "KINETICS OF CAPILLARY SHEAR DEGRADATION IN CONCENTRATED POLYMER SOLUTIONS." Journal of Chemical Physics **24**(6): 1196-1201.

6. Bird, R., W. Stewart, et al. (2002). Transport Phenomena, John Wiley and Sons.

7. Bjerrum, L., R. M. Kennard, et al. (1972). "HYDRAULIC FRACTURING IN FIELD PERMEABILITY TESTING." Geotechnique 22(2): 319-&.

8. Chang, H. (2004). Hydraulic fracturing in particulate materials. Atlanta, Georgia Institute of Technology. Ph.D.

9. Chevalier, C., A. Lindner, et al. (2007). "Destabilization of a saffman-taylor fingerlike pattern in a granular suspension." Physical Review Letters 99(17).

10. Chevalier, C., A. Lindner, et al. (2009). "Morphodynamics during air injection into a confined granular suspension." Journal of Non-Newtonian Fluid Mechanics 158(1-3): 63-72.

11. Chhabra, R. (2007). Bubbles, Drops and Particles in Non-Newtonian Fluids, Taylor and Francis Group

12. Chhabra, R. P., J. Comiti, et al. (2001). "Flow of non-Newtonian fluids in fixed and fluidised beds." Chemical Engineering Science 56(1): 1-27.

13. Chong, J. S., Christia.Eb, et al. (1971). "RHEOLOGY OF CONCENTRATED SUSPENSIONS." Journal of Applied Polymer Science 15(8): 2007-&.

14. Christoph R and Middleman.S (1965). "POWER-LAW FLOW THROUGH A PACKED TUBE." Industrial & Engineering Chemistry Fundamentals 4(4): 422-&.

15. Chuoke, R. L., P. Vanmeurs, et al. (1959). "The Instability of Slow, Immiscible, Viscous Liquid-Liquid Displacements in Permeable Media." Transactions of the American Institute of Mining and Metallurgical Engineers 216: 188-194.

16. Coussot, P. (2002). Flows of Concentrated Granular Mixtures. Transport Processes in Bubbles, Drops and Particles. Taylor and Francis.

17. Coussot, P. and A. Ancey (1999). "Rheophysical classification of concentrated suspensions and granular pastes." Physical Review E 59(4): 4445-4457.

18. Daccord, G. and J. Nittmann (1986). "RADIAL VISCOUS FINGERS AND DIFFUSION-LIMITED AGGREGATION - FRACTAL DIMENSION AND GROWTH SITES." Physical Review Letters 56(4): 336-339.

19. dePater, C. and Y. Dong (2007). "Experimental Study of Hydraulic Fracture in Sand as a Function of Stress and Fluid Rheology." SPE International(SPE 1051620).

20. dePater, C. and Y. Dong (2009). "Fracture Containment in Sof Sands by Permeability and Strength Contrasts." SPE International(SPE 119634).

21. Dong, Y. and C. dePater "Experimental Study of Hydraulic Fracturing in Sand as a Function of Stress and Fluid Rheology." SPE 105620.

22. Dong, Y. and C. dePater (2008). "Observation and Modeling of the Hydraulic Fracture Tip in Sands." American Rock Mechanics Association(ARMA 08-277).

23. Einstein, A. (1906). "The theory of the Brownian Motion." Annalen Der Physik 19(2): 371-381.

24. Fast, P., L. Kondic, et al. (2001). "Pattern formation in non-Newtonian Hele-Shaw flow." Physics of Fluids 13(5): 1191-1212.

25. Fayers, F. J. (1981). Enhanced Oil Rocovery.

26. Ferry, J. D. (1948). "VISCOELASTIC PROPERTIES OF POLYMER SOLUTIONS." Journal of Research of the National Bureau of Standards 41(1): 53-62.

27. Flew, S. and R. H. J. Sellin (1993). "NON-NEWTONIAN FLOW IN POROUS-MEDIA - A LABORATORY STUDY OF POLYACRYLAMIDE SOLUTIONS." Journal of Non-Newtonian Fluid Mechanics 47: 169-210.

28. Garagash, D. and E. Detournay (2000). "The tip region of a fluid-driven fracture in an elastic medium." Journal of Applied Mechanics-Transactions of the Asme 67(1): 183-192.

29. Ghannam, M. T. and M. N. Esmail (1998). "Rheological properties of aqueous polyacrylamide solutions." Journal of Applied Polymer Science 69(8): 1587-1597.

30. Golovin, F. "Observation and Characterization of Hydraulic Fractures in Cohesionless Sand." American Rock Mechanics Association ARMA 10-359.

31. Griffith, A. A. (1921). "PHENOMENA OF RUPTURE AND FLOW IN SOLIDS." Asm Transactions Quarterly 61(4): 871-&.

32. Haas, R. and W. M. Kulicke (1984). "FLOW BEHAVIOR OF DILUTE POLYACRYLAMIDE SOLUTIONS THROUGH POROUS-MEDIA .2. INDIRECT DETERMINATION OF EXTREMELY HIGH MOLECULAR-WEIGHTS AND SOME ASPECTS OF VISCOSITY DECREASE OVER LONG-TIME INTERVALS." Industrial & Engineering Chemistry Fundamentals 23(3): 316-319.

33. Hainey BW, e. a. "Onsite Fracture Disposal of Oilfield Waste Solids in Wilmington Field, California " SPA Production Facility 18: 88-93.

34. Hocking, G. and R. Ospina (1999). "Construction and Performance Monitoring of Permeable Reactive Barriers." Subsurface Barrier Technologies Feb.

35. Holtzman, R. and R. Juanes (2010). "Crossover from fingering to fracturing in deformable disordered media." Physical Review E 82(4).

36. Homsy, G. M. (1987). "VISCOUS FINGERING IN POROUS-MEDIA." Annual Review of Fluid Mechanics 19: 271-311.

37. Hu, R. Y. Z., A. T. A. Wang, et al. (1991). "SURFACE-TENSION MEASUREMENT OF AQUEOUS POLYMER-SOLUTIONS." Experimental Thermal and Fluid Science 4(6): 723-729.

38. Huang, H. and J. Ayoub (2008). "Applicability of the Forchheimer equation for non-Darcy flow in porous media." SPE Journal 13(1): 112-122.

39. Huang, H. and R. Wu (2008). Fluid injection into granular media under confinement. Proceedings of the XVth International Congress on Rheology, Monterey, CA.

40. Huang, H., F. Zhang, et al. (2011). Fluid Injection Experiments in Two-dimensional Porous Media. Proceedings from the 2011 SPE Hydraulic Fracturing Technology Conference; The Woodlands, Texas. SPE140502.

41. Huang, N., G. Ovarlez, et al. (2005). "Flow of wet granular materials." Physical Review Letters 94(2).

42. Huang, H., P. Callahan, et al. (2010). "Pattern Formation in Fluid Injection into Granular Media." Presentation at the University of Pittsburgh, Ohio.

43. Jaworski, G. W., J. M. Duncan, et al. (1981). "LABORATORY STUDY OF HYDRAULIC FRACTURING." Journal of the Geotechnical Engineering Division-Asce 107(6): 713-732.

44. Johnsen, O., C. Chevalier, et al. (2008). "Decompaction and fluidization of a saturated and confined granular medium by injection of a viscous liquid or gas." Physical Review E 78(5).

45. Khodaverdian, M. and P. McElfresh (2000). Hydraulic fracturing stimulation in poorly consolidated sand: Mechanisms and consequences. SPE 63233 presented at the SPE Annual Technical Conference and Exhibition, Dallas, TX.

46. Khodaverdian, M., T. Sorop, et al. (2010). "Polymer Flooding in Unconsolidated-Sand Formations: Fracturing and Geomechanical Considerations." Spe Production & Operations 25(2): 211-222.

47. Kondic, L., P. PalffyMuhoray, et al. (1996). "Models of non-Newtonian Hele-Shaw flow." Physical Review E 54(5): R4536-R4539.

48. Kondic, L., M. J. Shelley, et al. (1998). "Non-Newtonian Hele-Shaw flow and the Saffman-Taylor instability." Physical Review Letters 80(7): 1433-1436.

49. Kulicke, W. M. and N. Bose (1986). "THE ROLE OF POLYMERS IN ENHANCED OIL-RECOVERY." Abstracts of Papers of the American Chemical Society 192: 53-PMSE.

50. Kutzner, C., Ed. (1996). Grouting of Rock and Soil.

51. Lemaire, E., P. Levitz, et al. (1991). "FROM VISCOUS FINGERING TO VISCOELASTIC FRACTURING IN COLLOIDAL FLUIDS." Physical Review Letters 67(15): 2009-2012.

52. Lindner, A., D. Bonn, et al. (2002). "Viscous fingering in non-Newtonian fluids." Journal of Fluid Mechanics 469: 237-256.

53. Littman, W. "Polymer Flooding." Developments in Petroleum Science 24: 25-28.

54. Litynski, J., S. Klara, et al. (2006). "The United States Department of Energy's Regional Carbon Sequestration Partnerships Program: A collaborative approach to carbon management." Environment International 32: 128-144.

55. Lovoll, G., Y. Meheust, et al. (2004). "Growth activity during fingering in a porous Hele-Shaw cell." Physical Review E 70(2).

56. Macosko, C. W. (1994). Rheology Principles, Measurements, and Applications, Wiley-VHC.

57. Marshall, R. J. and A. B. Metzner (1967). "FLOW OF VISCOELASTIC FLUIDS THROUGH POROUS MEDIA." Industrial & Engineering Chemistry Fundamentals 6(3): 393-&.

58. McLean, J. W. and P. G. Saffman (1981). "THE EFFECT OF SURFACE-TENSION ON THE SHAPE OF FINGERS IN A HELE SHAW CELL." Journal of Fluid Mechanics 102(JAN): 455-469.

59. Mills, P., P. Cerasi, et al. (1995). "EROSION INSTABILITY IN A NON-CONSOLIDATED POROUS-MEDIUM." Europhysics Letters 29(3): 215-220.

60. Nittmann, J., G. Daccord, et al. (1985). "FRACTAL GROWTH OF VISCOUS FINGERS - QUANTITATIVE CHARACTERIZATION OF A FLUID INSTABILITY PHENOMENON." Nature 314(6007): 141-144.

61. Nottelmann, H. and W. M. Kulicke (1991). "PREPARATION, CHARACTERIZATION, AND RHEOLOGICAL BEHAVIOR OF WATER-SWELLABLE POLYMER NETWORKS." Acs Symposium Series 462: 62-87.

62. Paterson, L. (1981). "RADIAL FINGERING IN A HELE SHAW CELL." Journal of Fluid Mechanics 113(DEC): 513-529.

63. Pearson, J. R. A. and P. M. J. Tardy (2002). "Models for flow of non-Newtonian and complex fluids through porous media." Journal of Non-Newtonian Fluid Mechanics 102(2): 447-473.

64. Peters, E. J. and D. L. Flock (1981). "THE ONSET OF INSTABILITY DURING 2-PHASE IMMISCIBLE DISPLACEMENT IN POROUS-MEDIA." Society of Petroleum Engineers Journal 21(2): 249-258.

65. Pinto, S. F., M. S. Couto, et al. (2007). "Granular fingers on jammed systems: New fluidlike patterns arising in grain-grain invasion experiments." Physical Review Letters 99(6).

66. Rossmanith, H. (1983). "Rock Fracture Mechanics." International centre for Mechanical Science: 1-17.

67. Saffman, P. G. and G. Taylor (1958). "THE PENETRATION OF A FLUID INTO A POROUS MEDIUM OR HELE-SHAW CELL CONTAINING A MORE VISCOUS

LIQUID." Proceedings of the Royal Society of London Series a-Mathematical and Physical Sciences 245(1242): 312-&.

68. Santamarina, J. (2001). "Soil Behavior at the Microscale: Particle Forces." Soil Behavior and Soft Ground Construction Ladd Symposium.

69. Seed, H. B. and J. M. Duncan (1987). "THE FAILURE OF TETON DAM." Engineering Geology 24(1-4): 173-205.

70. Shah, C. B. and Y. C. Yortsos (1995). "ASPECTS OF FLOW OF POWER-LAW FLUIDS IN POROUS-MEDIA." Aiche Journal 41(5): 1099-1112.

71. Shin, H. and J. C. Santamarina (2010). "Fluid-driven fractures in uncemented sediments: Underlying particle-level processes." Earth and Planetary Science Letters 299(1-2): 180-189.

72. Sochi, T. (2010). "Non-Newtonian flow in porous media." Polymer 51(22): 5007-5023.

73. Soga, K., S. K. A. Au, et al. (2004). "Laboratory investigation of multiple grout injections into clay." Geotechnique 54(2): 81-90.

74. Stickel, J. J. and R. L. Powell (2005). "Fluid mechanics and rheology of dense suspensions." Annual Review of Fluid Mechanics 37: 129-149.

75. Tordjeman, P. (2007). "Saffman-Taylor instability of shear thinning fluids." Physics of Fluids 19(11).

76. Wu, J. S., B. M. Yu, et al. (2008). "A resistance model for flow through porous media." Transport in Porous Media 71(3): 331-343.

77. Wu, R. (2006). Some fundamental mechanisms of hydraulic fracturing. Atlanta, Georgia Institute of Technology. Ph.D.

78. Xia, H., D. Wang, et al. (2008). "Effect of polymer solution viscoelasticity on residual oil." Petroleum Science and Technology 26(4): 398-412.